ACCURACY OF AERODYNAMIC PREDICTIONS AND ITS EFFECTS ON SUPERSONIC TRANSPORT DESIGN

Duane L. Knill*, Vladimir Balabanov*, Oleg Golovidov*,
Bernard Grossman†, William H. Mason‡, Raphael T. Haftka§,
and Layne T. Watson¶

MAD Report 96–12–01

December 1996

Supported by the NASA Langley Research Center
under grants NAG1-1160 and NAG1-1562.

**Multidisciplinary Analysis and Design Center
for Advanced Vehicles**

Virginia Polytechnic Institute and State University
Blacksburg, Virginia 24061–0203

---

*Graduate Research Assistant, Dept. of Aerospace and Ocean Engineering.
†Professor and Dept. Head of Aerospace and Ocean Engineering.
‡Professor of Aerospace and Ocean Engineering.
§Professor of Aerospace Engineering, Mechanics and Engineering Science, University of Florida, Gainesville, FL.
¶Professor of Computer Science and Mathematics

Abstract

An investigation of the aerodynamic modeling requirements for HSCT design is made. The purpose of this study is to determine the effects of including Euler and Navier-Stokes calculations for the supersonic aerodynamics and structural loading predictions in a multidisciplinary HSCT design optimization procedure. The accuracy, computational effort, and ease of implementation of the CFD analyses into the optimization process are compared with that of simpler models based on a combination of linear theory, slender body theory, and boundary layer theory. The accuracy of these simple models and grid-converged CFD solutions is quantified through comparisons with experimental data on analytic forebodies and wings. Differences in the cruise drag predictions of up to 2 counts are seen in the designs considered, which have cruise drag coefficients ranging from 70 to 85 counts. While this appears to be a small discrepancy, it has a large effect on the aircraft range and weight. A two count increase in cruise drag corresponds to a 120 *n.mi.* reduction in the range and a 56,000 *lb* increase in the take-off gross weight (TOGW) for an aircraft with a 5500 *n.mi.* range and a nominal TOGW of 770,000 *lb*. There is little difference noted in the wing loadings predicted from Euler and parabolized Navier-Stokes analyses. Linear theory loads match CFD loads well at cruise conditions, but not at high-lift conditions where crossflow shocks appear on the wing. Wing bending stresses are sensitive to small variations in the loading and spanwise center of pressure location. Even at cruise conditions where linear theory and Euler loads show good agreement, there are differences in the maximum bending stress of up to 26.5%. This sensitivity is a result of the fuel weight in the wings canceling much of the wing bending due to aerodynamic loading. Despite the large variations in the stresses and loads at high-lift conditions using the different aerodynamic models, the optimized wing bending-material weights show relatively small variations up to 1800 *lb*. Significant gains in the accuracy of our aerodynamic performance predictions can be realized using CFD calculations in the optimization, but the large computational requirements preclude the sole use of Euler or Navier-Stokes solutions in an efficient high-dimensional multidisciplinary aircraft optimization.

Contents

⋆ **Note:** Tables and Figures are placed after the appropriate subsection

1. Introduction

Procedures for the combined aerodynamic–structural design optimization of a high-speed civil transport (HSCT) have been developed recently at Virginia Tech.[1–4] The current detailed aerodynamic analyses in these studies involve what we term *linear supersonic theory*, comprising slender body results for wave drag, a linear theory panel code modified with leading-edge suction corrections for drag-due-to-lift and supersonic loads, and algebraic skin friction estimates. These analyses are used to predict, for example, the drag at cruise and the supersonic loads for the structural optimization. The overall purpose of this paper is to investigate the implications of supplementing the linear supersonic theory calculations in our HSCT optimization with Euler and Navier-Stokes solutions. To achieve this goal, we first validate and then certify an Euler/Navier-Stokes code for HSCT applications at both supersonic cruise and at off-design conditions. This paper will concentrate on the supersonic flight regime. The accuracy of the range estimates based on Euler and Navier-Stokes results are compared with those from linear supersonic theory. We also compare the accuracy of the loads calculated by Euler/Navier-Stokes with linear supersonic theory and examine the effects of any differences on the structural optimization.

1.1. Background

The HSCT design problem considered in Refs. 1–4 involves the minimization of the take-off gross weight (TOGW) with a range constraint of 5500 *n.mi.*, a cruise Mach number of 2.4, and 251 passengers. The optimization uses 70 constraints which can be grouped into three categories: geometric constraints, performance/aerodynamic constraints, and constraints implicit in the analysis. The implicit constraints are a part of the analysis or geometry definition and are not handled directly by the optimization. They include an altitude limit, a fuselage volume constraint, and wing mean aerodynamic chord (MAC) and nacelle orientation specifications. The wing shape, fuselage shape, tail areas, and nacelle sizes and locations are described using 26 design variables with two additional variables for the mission profile and another for the fuel, giving a total of 29 design variables. To efficiently perform the optimization, a variable-complexity modeling (VCM) technique (Refs. 1–4) has been employed. This technique utilizes both simple and complex models for predicting aerodynamic performance and structural weights. The simple conceptual-design-level methods are predominantly used in the optimization due to their low computational costs. More accurate and more computationally expensive methods are used to periodically update the simpler models. In this way, one incorporates the accuracy of the higher level codes with the computational efficiency of the simpler models.

The linear supersonic theory methods used as our current detailed model includes the Harris[5] wave drag program, a panel method by Carlson[6] *et al.* with attainable leading-edge thrust corrections[7], and standard algebraic estimates of the skin friction using the Van Driest II method.[8] In the present work, we are investigating the benefits of introducing Euler/Navier-Stokes computations as the next level of complexity in the hierarchy of supersonic aerodynamic prediction models.

Related studies[9–11] on the use of CFD methods for supersonic HSCT design have appeared elsewhere. For pure analysis, Hollenback and Blom[9] compared parabolized Navier-Stokes (PNS) results with experimental data, Euler, and linear theory results for a Mach 2.4 HSCT design. Pittman[10] *et al.* obtained Euler equation solutions for a Mach 3 HSCT concept, and compared the results with linear theory. Their predictions were later verified by comparison to experimental data[12]. In each case, linear theory slightly overpredicted the lift, underpredicted the drag, and produced poor pitching moment results. However, Pittman[10] *et al.* concluded that linear theory is still useful in conceptual and preliminary design.

Mann and Carlson[11] evaluated the use of Euler analysis within the design context. Looking at

pressure distributions, they proposed a method to overcome linear theory deficiencies and concluded that there is no significant advantage to the use of Euler codes in their wing design procedures. We extend these studies to show the effects of differences in aerodynamic prediction tools on HSCT performance, wing stresses, and aerodynamic/structural optimization results.

1.2. Fluid Dynamics Code

We are using version 2.2 of the General Aerodynamic Simulation Program[13] (GASP) for the Euler and PNS calculations. The PNS equations are a subset of the complete Navier-Stokes equations, valid in supersonic conditions, in which the streamwise shear stress terms are neglected. By suppressing a portion of the streamwise pressure gradient the equation type is changed from elliptic to parabolic, allowing the solution to be space marched in the streamwise direction. This reduces the computational cost by an order of magnitude as compared to that required for a complete Navier-Stokes solution. The PNS equations can predict crossflow separation but not streamwise separation. For our PNS calculations, the flow is considered to be fully turbulent, and the Baldwin-Lomax turbulence model is used. GASP is a fully conservative CFD code which solves the Reynolds-averaged Navier-Stokes equations and many of its subsets. The code uses an upwind three-dimensional finite-volume spatial discretization. Roe, Van Leer, Steger-Warming, and full flux functions are available in each direction. Roe flux difference splitting is used in this study. For our calculations, a third-order upwind biased interpolation is used in each of the marching planes.

The finite-volume formulation of the Reynolds-averaged Navier-Stokes equations may be written in terms of the vector of conserved variables, Q, the vector of primitive variables, q, the cell volume, V, and a residual vector, $R(q)$, as

$$\frac{\partial <Q>}{\partial q}\frac{\partial <q>}{\partial t}V + R(q) = 0.$$

The cell average quantity, $<Q>$, is defined by integrating over the volume of the cell

$$<Q> = \frac{1}{V}\iiint_V Q(x,y,z,t)\,dV.$$

The cell average quantity for the primitive variables, $<q>$, is defined in the same manner. The residual vector can be written as a function of the inviscid fluxes, $\vec{F}$, the viscous fluxes, $\vec{F}_v$, the unit normal vectors, $\hat{n}$, to the cell faces, and the areas, ΔA, of the cell faces as

$$R(q) = \sum_{j=1}^{nface}\left(\vec{F} - \vec{F}_v\right)\cdot\hat{n}_j\,\Delta A_j.$$

The norm of this residual vector represents the convergence to the steady state solution. GASP iteratively solves the system of equations until a prescribed reduction in the residual norm is reached. GASP can implement global iteration techniques as well as space-marching schemes. Due to the large savings in computational time, space-marching has been performed for all of the supersonic CFD calculations presented in this report.

1.3. CFD Grids

The grids for the space-marching calculations on HSCT wings and wing-fuselage combinations are created using a 3-D grid generator originally developed by Barger[14] and modified in the present work. The original grid generator has been modified to give better resolution of the wing leading-edge geometry. In addition, the code has been improved to be more robust for large planform variations. The grid generator receives as input the aircraft configuration stored in the Craidon[15] geometry format, extends

the wing to join the fuselage, performs filleting of the wing-fuselage intersection, [16] and then creates a grid for space-marching calculations. Since our HSCT optimization code creates a Craidon description file from its set of design variables, the conversion from a set of design variables to a space marching CFD grid is straightforward.

The space-marching planes are created along *x=constant* planes. Two of these computational planes for a wing-fuselage configuration are shown in Fig. 1. A Mach cone analysis is used to form the outer boundary to ensure that all shocks are contained within the computational domain. The grid generator allows for flexible stretching of the grid points around and normal to the aircraft to create grids suitable for both Euler and Navier-Stokes calculations. Measures are employed to reduce grid skewness at the wing tip and wing-fuselage juncture. The grid generator is automated and robust for large planform changes. These qualities are required for design optimization applications.

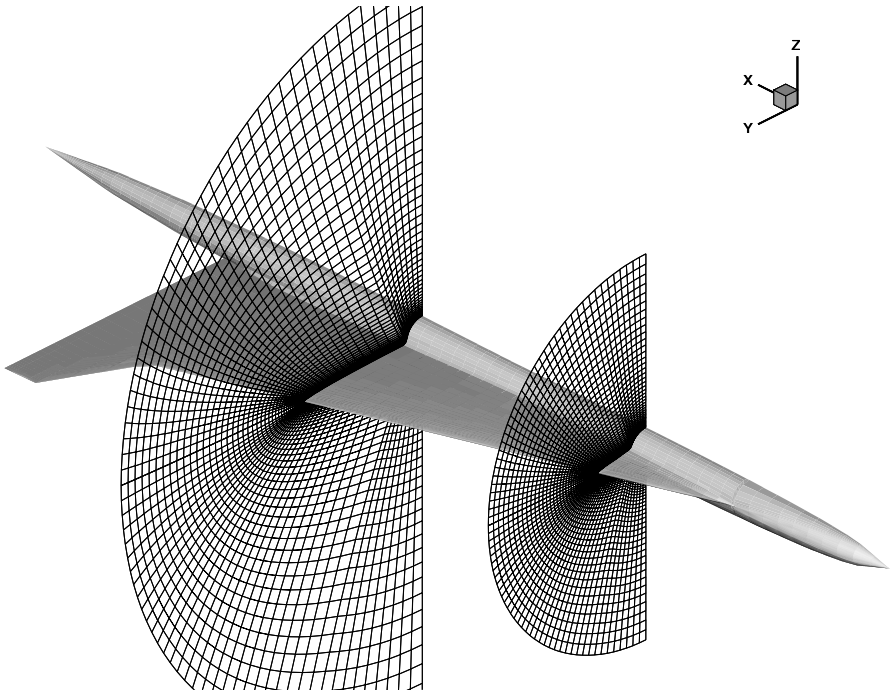

Figure 1: HSCT Wing-Fuselage and Grid Slice

1.4. Structural Optimization

The structural analyses and optimization are performed using the general purpose finite-element (FE) structural optimization code GENESIS.[17] The FE model used in the structural analysis consists of 451 rods, 383 membrane elements, and 129 shear panels. The 963 elements are joined together at 193 nodes with a total of 1032 degrees of freedom. Optimizations can be performed using the Method of Feasible Directions, the Sequential Linear Programming method, and the Sequential Quadratic Programming method. We use the Method of Feasible Directions for our problem. A coarse grained parallel version of GENESIS has been implemented on 28 nodes of the Intel Paragon computer at Virginia Tech (Ref. 18). This is a 119 node parallel computer with distributed memory. An automated structural mesh generator[19] has been developed to construct the FE model for the HSCT configuration. As with the space-marching CFD grid generator, the FE grid generator uses as input the Craidon description of the aircraft.

1.5. Code Verification, Validation, and Certification

As CFD technology matured, code verification became important. In 1988, Bobbitt[20] presented a comprehensive survey of code verification issues, and AGARD held a conference[21] on the verification of CFD codes. Since then, the establishment of a rigorous basis for verifying and certifying codes has been found to be more difficult than originally envisioned. An excellent discussion has been given by Aeschliman[22] *et al.*

To assess the consequences of including CFD results in the variable-complexity modeling approach to HSCT optimization, the guidelines on code certification procedures outlined by NASA and the Multidisciplinary Analysis and Design Industrial Consortium (MADIC)[23–25] have been followed. First in this process is the code *verification*, which establishes an acceptable level of accuracy in the calculation. The MADIC/NASA panel defines verification as "the process that demonstrates the code's ability to solve the specific set of governing equations and boundary conditions posed to the computer by the code."[24] Grid refinement studies and comparison to experimental data are key components in this process. The *validation* step then ensures that the code properly models the flow physics. In this presentation, we are conceding that our models do not exactly model the correct flow physics. The point in question is how much of an effect does moving to higher fidelity aerodynamic models have on certain parameters of interest. The *certification* of the code for the specific design applications can take place only after these steps are completed. Certification assesses the adequacy of the code for a specific class of applications. For design optimization, the key issues are accuracy, robustness, computational effort, and ease of implementation. The trade-off between accuracy and computational effort is of practical significance, and in essence is the motivation of our variable-complexity modeling technique.

1.6. Outline

We begin to address these issues by comparing the wave drag predictions from the Harris code and Euler calculations with experimental data on simple analytic axisymmetric forebodies and a symmetric delta-wing. Data from a high-lift maneuver wing is then used to determine the accuracy of the linear theory drag-due-to-lift and skin friction estimates as well as the accuracy of the Euler and PNS predictions. Grid convergence and residual norm reduction studies are performed to give insight into the mesh sizes and computational effort required to achieve converged results. After establishing the level of accuracy in our CFD solutions, the integrated forces and moments for our HSCT wings and wing-fuselage configurations are computed using the Euler and PNS equations. These results are then compared to those predicted from linear supersonic theory, and the sensitivity of the aircraft range to the predicted value of the drag is determined from analysis. The effects of drag changes to the optimized configuration is determined. We also investigate the differences in the distributed loads and their effects on the structural analysis. The Von Mises equivalent stresses calculated using linear theory and CFD loads are compared at supersonic cruise and off-design conditions. These loads are then used in the structural optimization to compare the wing bending material weights computed using linear supersonic theory loads and CFD loads. From these investigations we attempt to determine where in the design optimization process it is advantageous to increase the accuracy of linear supersonic theory results with higher level CFD analyses and discuss practical ways to move to the more computationally expensive methods.

2. Preliminary Studies: Code Verification

2.1. Haack-Adams Bodies

Our studies begin by investigating the zero-lift wave drag prediction for a series of Haack-Adams bodies.[26] Calculations have been performed using two different fineness ratios: $l/d_{max} = 7$ and $l/d_{max} = 10$. The bodies in this study have a non-zero base area, A_{base}, for mounting to a sting in the wing-tunnel tests. The equation for the radius, r, of these bodies with area ratio $A_{base}/A_{max} = 0.532$ is given as:

$$\frac{r}{r_{max}} = \left\{ 0.707 \left[1 - \left(\frac{2x}{l} - 1 \right)^2 \right]^{3/2} + 0.16934 \left(\frac{2x}{l} - 1 \right) \left[1 - \left(\frac{2x}{l} - 1 \right)^2 \right]^{1/2} + 0.16934 \cos^{-1} \left(1 - \frac{2x}{l} \right) \right\}^{1/2}.$$

Investigation of the body shape (Fig. 2) reveals that the nose is blunt. However, following work by Mason and Lee,[27] the CFD solutions are space-marched as if the nose were sharp. They found that certain classes of bodies, while having geometrically blunt noses, produce flowfields which do not exhibit classical blunt body behavior. These bodies can be treated as if they are geometrically sharp. The Haack-Adams bodies are treated in this manner.

A grid convergence study of the wave drag (Fig. 3) for the Euler equations is performed for the body with $l/d_{max} = 10$ at Mach 2.5. An axisymmetric grid is used for these calculations, so the total number of cells, N, is the number of axial cells times the number of normal cells. Meshes with uniform axial spacing and with distributions clustered at the nose are considered. For the clustered grids, two different grid aspect ratios are considered. One has an equal number of axial and normal points, while the other has twice the number of axial points as normal points. The clustered grids with a $1:1$ (*normal:axial*) grid ratio range in size from 11×11 to 71×71. The clustered grids with a $1:2$ grid ratio range in size from 11×21 to 41×81. The uniform grids with a $1:2$ grid ratio range in size from 11×21 to 81×161.

Clearly, the grids with axial points clustered near the nose outperform the grids with uniform axial spacing. Both the 36×71 and 51×51 clustered grids produce converged results, where our criteria for convergence is computed drag values within one percent of the extrapolated value as $N \to \infty$. Since the 36×71 grid has 50 fewer grid cells than the 51×51 grid, it is chosen for use in the Euler computations. The drag for these bodies is non-dimensionalized using the free stream conditions and the maximum cross-sectional area, A_{max}, of the body.

Methods quantifying grid convergence for CFD solutions using a Grid Convergence Index (GCI) are described in Ref. 28. The GCI measures the uncertainty of the grid convergence based upon the error derived from generalized Richardson extrapolation theory. This method is applied to cases where the solution on only a few grids are available. Since we are able to obtain solutions relatively quickly through the supersonic space-marching techniques, we have the luxury of producing solutions over a large number of mesh sizes and graphically extrapolating the solution for zero mesh size. Therefore, the GCI is not used as a measure of our grid convergence. The GCI method will be applicable when this study is extended to the transonic regime where our computational costs will increase by an order of magnitude and the method used in this report for determining grid convergence will not be feasible.

Convergence of the wave drag with the prescribed residual norm reduction (Fig. 4) is investigated for the body in a Mach 2.5 flow using the clustered 71×71 grid. The *residual norm reduction* plotted in the graph refers to how many orders of magnitude the residual norm is required to decrease from its value at the first iteration in each marching plane. Mathematically it can be written for each marching plane as

$$\text{residual norm reduction} = \frac{||R||^{(i)}}{||R||^{(1)}},$$

where $||R||^{(i)}$ is the norm of the residual vector at the i^{th} iteration. The wave drag prediction is nearly constant after the residual has been reduced by four orders of magnitude, so all other calculations on the Haack-Adams body are performed with this convergence criterion.

The Euler wave drag predictions show substantial improvement over the Harris wave drag code results (Figs. 5,6) for both the $l/d_{max} = 7$ and $l/d_{max} = 10$ cases. The Harris code performs poorly with increasing Mach number for this case. While the experimental data and Euler prediction of the wave drag decrease with Mach number, the Harris code wave drag prediction begins to increase with Mach number. As expected, the accuracy of the Harris wave drag results does improve for the more slender body.

The computational time required for the Euler analysis of the Haack-Adams forebody is approximately three minutes (0.07 sec/cell) for the clustered 36×71 grid on a single processor SGI R4000 workstation. By comparison, the Harris wave drag code takes less than one second to compute the drag.

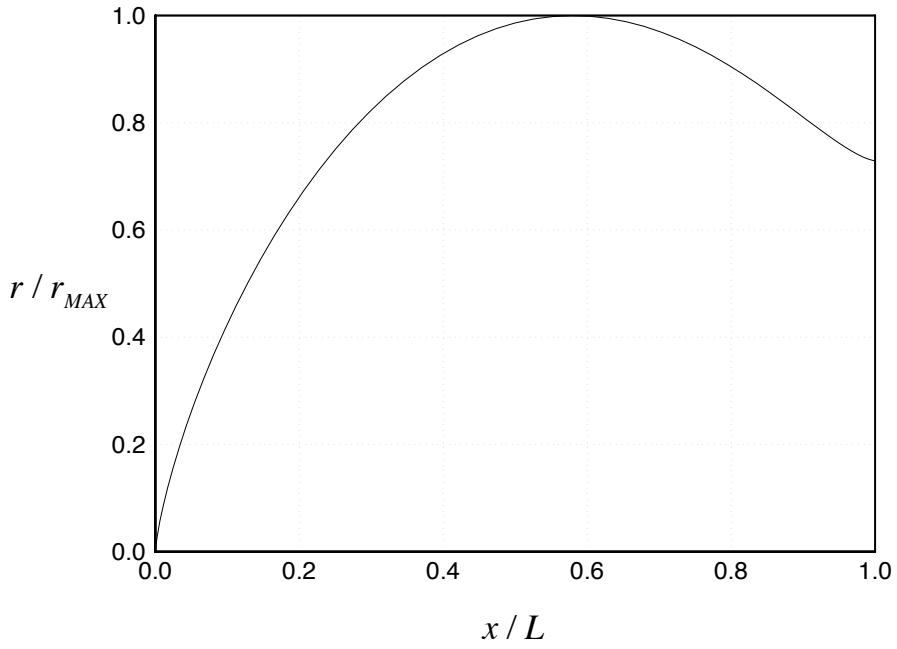

Figure 2: Haack-Adams Body Shape

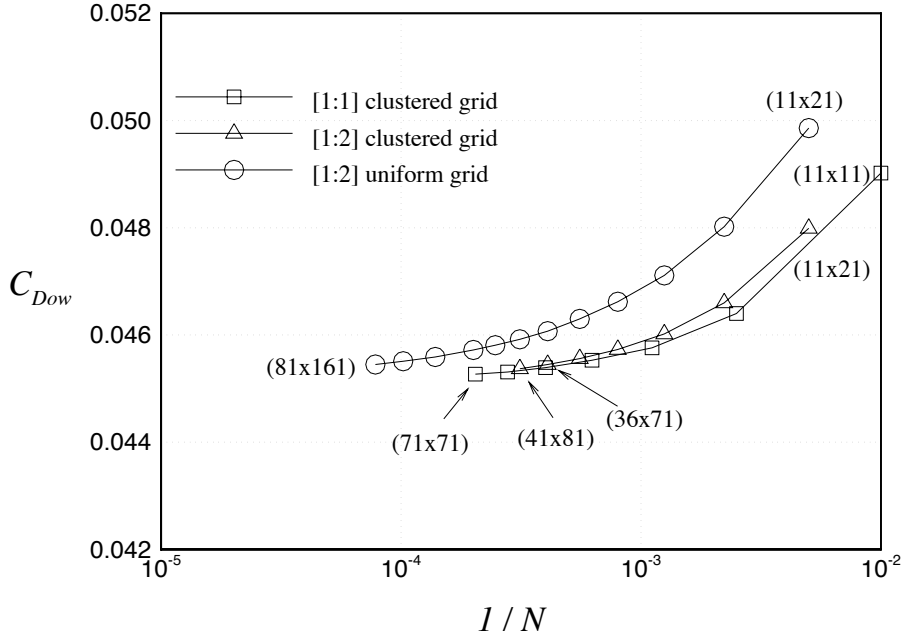

Figure 3: Haack-Adams Grid Convergence

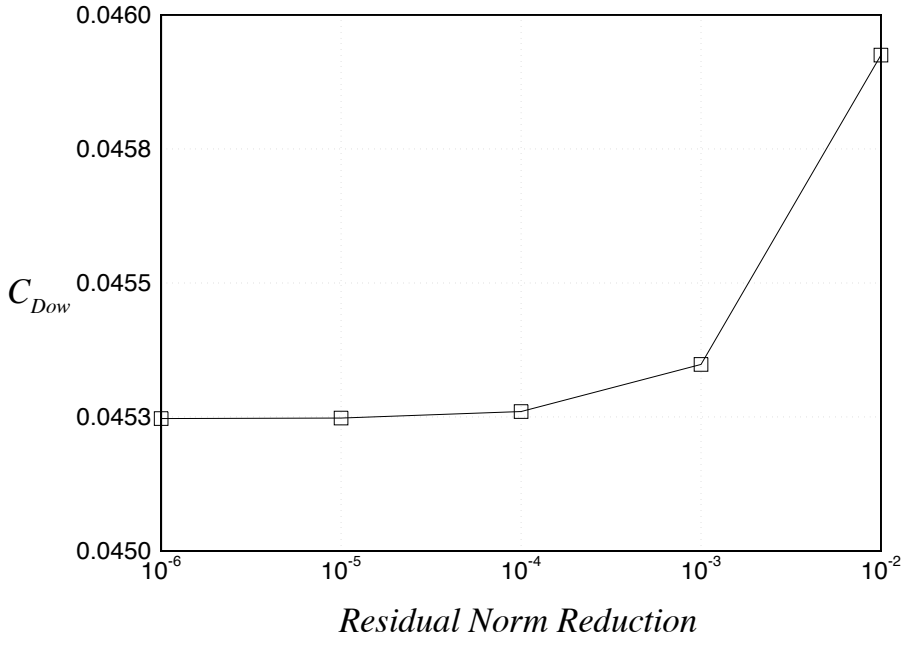

Figure 4: Haack-Adams Residual Norm Reduction

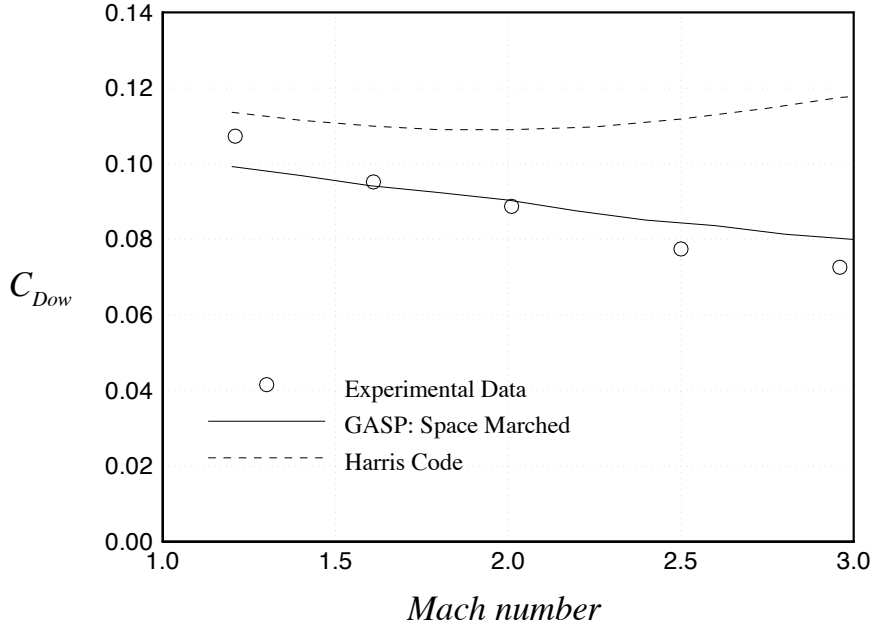

Figure 5: Haack-Adams Wave Drag ($l/d_{max} = 7$)

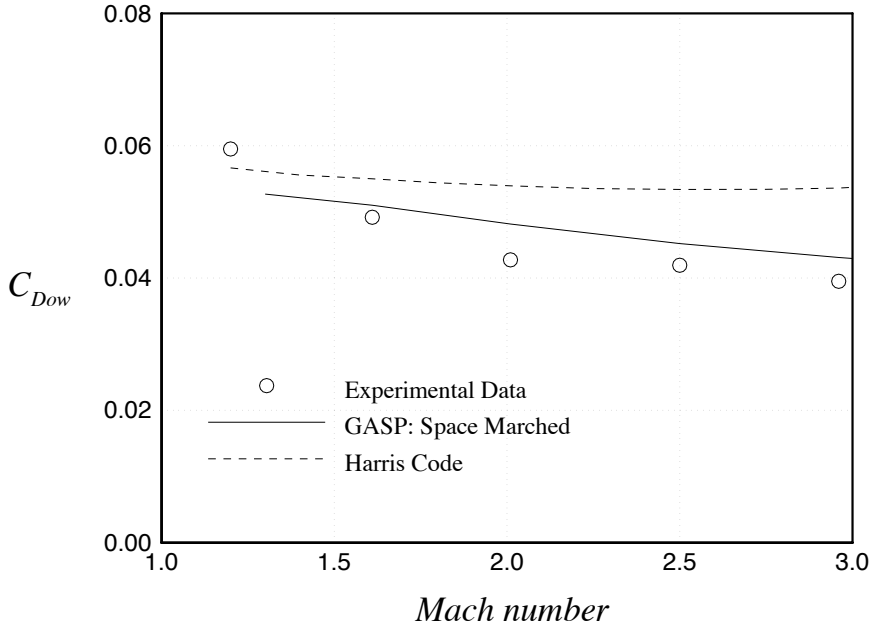

Figure 6: Haack-Adams Wave Drag ($l/d_{max} = 10$)

2.2. Squire Wing

We now investigate the wave drag prediction on a symmetric delta wing. The Squire wing (Fig. 7) is a delta wing with a biconvex centerline and elliptic cross-section. The thickness of each cross-section is chosen to match the cross-sectional area of a 9% thick biconvex wing with a diamond-shaped cross-section[29]. The space marching grid is created with the grid points clustered near the wing in the same way they were for the Haack-Adams body. The wing surface grid is also clustered along the leading edge to properly define the elliptical cross-section geometry.

Grid refinement studies are performed on the wing at 0° angle-of-attack and Mach 2.4. Figure 8 shows the relative effects of varying the number of grid points in only one direction. This is done to identify the dimension to which the wave drag is most sensitive. The drag coefficient data, based on the planform area, is given in *counts* of drag, where one count of drag is equivalent to $C_D = 0.0001$. The coarsest grid considered is 21×21×21. The number of spanwise, outward, and chordwise points are increased to 141, 81, and 101 respectively. As expected, the number of spanwise points is found to have the largest effect on the drag. Note that the scale for this graph is very small. The total change in drag from the coarsest to finest grid for the spanwise variation is slightly less than one count. With this in mind, a grid convergence study (Fig. 9) for a [3:2:2] aspect ratio grid [*spanwise*:*outward*:*chordwise*] is investigated. The 61×41×41 grid is chosen for our computations. The wave drag predicted from solution on this mesh is within 1/4 count of the value extrapolated as $N \to \infty$. The residual norm reduction study (Fig. 10) performed on the 61×41×41 grid at Mach 2.4 indicates that requiring the residual norm to decrease by two orders of magnitude is sufficient for converged wave drag results. This is a less stringent criteria than is required for converged results on the Haack-Adams bodies.

Inspection of the wave drag results (Fig. 11) shows good agreement between GASP and the experimental data. The Harris wave drag results show the same overprediction found in the results for the thickest Haack-Adams body. Similar comparisons of the wave drag coefficients predicted from linear theory and from a three-dimensional nonlinear full-potential code (NCOREL) are presented in Ref. 30. The Euler computation for the 61×41×41 grid took about 19 minutes (0.012 sec/cell) on an SGI R4000 workstation.

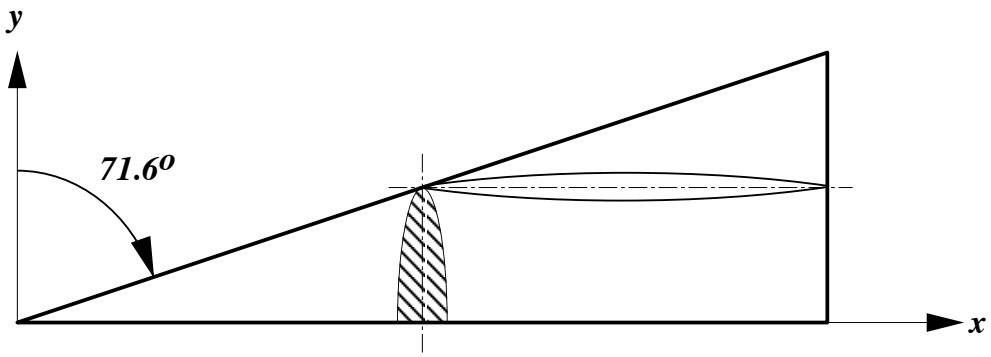

Figure 7: Squire Wing

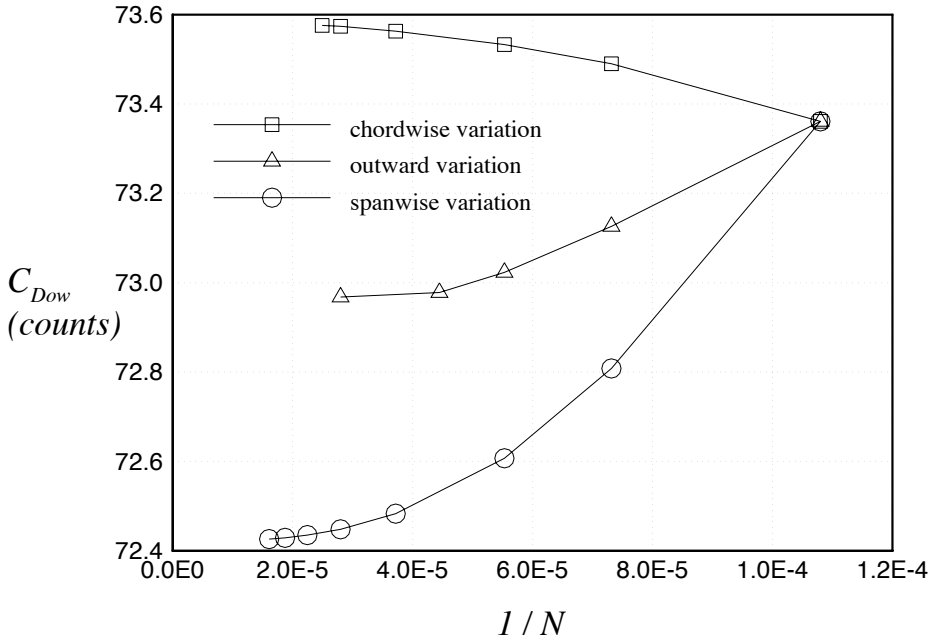

Figure 8: Squire Wing Grid Convergence

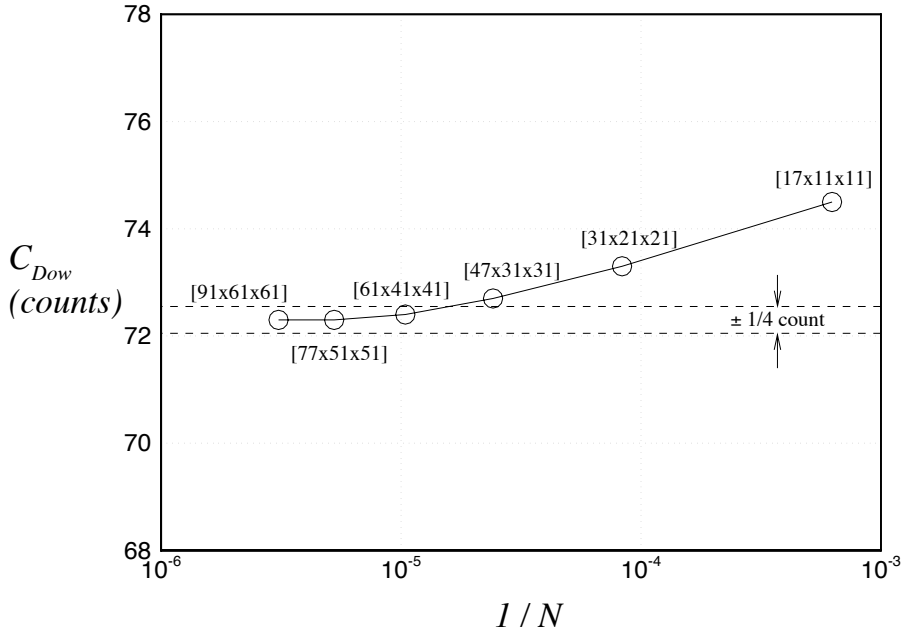

Figure 9: Squire Wing Grid Convergence

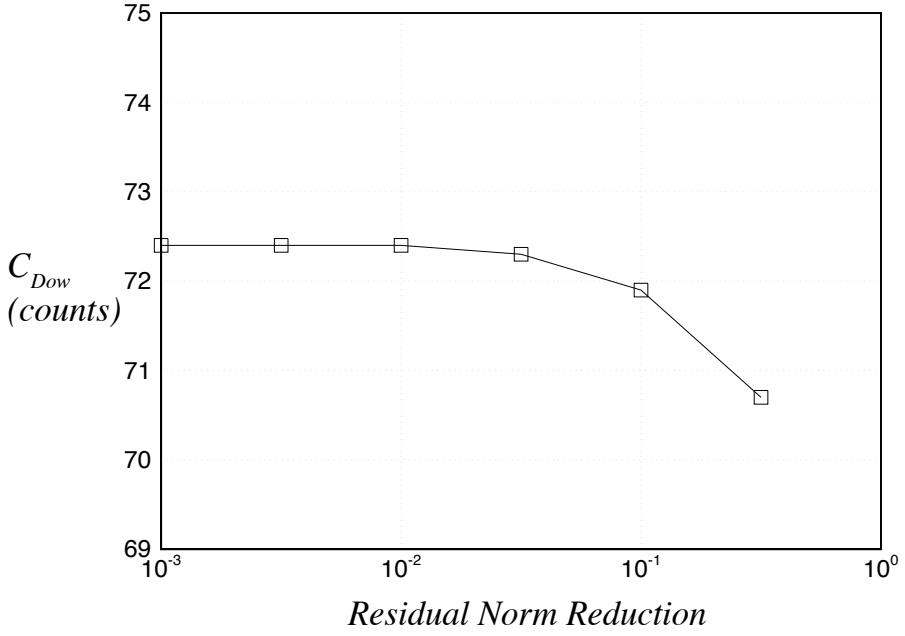

Figure 10: Squire Wing Residual Norm Reduction

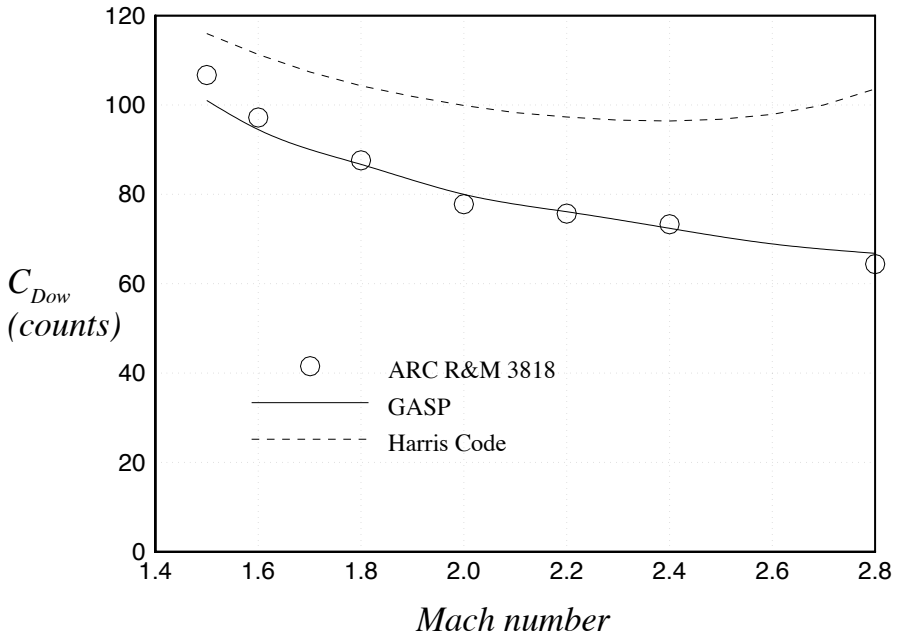

Figure 11: Squire Wing Wave Drag Coefficient

2.3. High-Lift Maneuver Wing

The study will now focus on the force and moment predictions from linear supersonic theory and from GASP. A high-lift maneuver wing [31–33] with experimental force and moment data and pressure distributions is selected to assess the accuracy of the codes. The experimental pressures have previously been compared with predictions from linear theory and potential methods.[32] The high-lift wing (Fig. 12) is only slightly cambered in the streamwise sections, but it has pronounced spanwise cambering. Another feature of this wing is that, due to its design, inviscid flow conditions predominate on the upper surface. The wing was tested at Mach 1.62 and angles of attack, α, ranging from 0° through 14°.

The grid convergence study (Fig. 13) reveals that a 77×51×77 mesh (*spanwise* ×*outward* ×*chordwise*) is sufficient for Euler computations on this wing. The solution on this mesh gave the drag coefficient within 1/2 count of the solution predicted by extrapolating to a mesh with an infinite number of cells. Calculations on this grid took about 18 minutes (0.004 sec/cell) on an SGI Power Challenge R8000. A 77×91×77 grid is chosen for the PNS calculations from the grid convergence study in Figure 14. Computations for a single angle of attack on this grid took about 2.5 hours (0.017 sec/cell) on an SGI Power Challenge R8000 to converge. Using a hyperbolic tangent distribution to stretch the grid points normal to the body gives 40 cells in the boundary layer with the first cell well inside the laminar sublayer ($y^+ \approx 1.0$). Grid-converged results are therefore obtained with meshes having the same number of cells in the inviscid region for both the PNS and Euler grids.

Reducing the residual two orders of magnitude is found to be sufficient for both the parabolized Navier-Stokes and Euler computations on this wing. The results from the Euler and linear theory codes are adjusted to include an axial friction drag coefficient of 0.0069 to compare with the experimental data. This viscous correction was obtained by Pittman[33] *et al.* using the method in Ref. 34. This viscous term is assumed to be invariant with the angle-of-attack. Generally, the CFD results compare well with the experimental data. The PNS lift curve (Fig. 15) matches the experimental data nearly perfectly. The Euler results have the correct lift-curve slope, C_{L_α}, but the zero-lift angle of attack is slightly off. There is a 7.5% overprediction in the linear theory C_{L_α}.

The pitching moment is taken about the point $x = 16.701$, $y = 0.0$, $z = -0.275$, where the origin of the coordinate system is the wing apex. The pitching moment coefficients show the greatest discrepancy between the computational methods and experiment. While the Euler and PNS pitching moment results differ from the experimental data, they are significantly more accurate than the linear theory results. The same behaviors are seen in the pitching moment data in Ref. 33 computed using the full-potential code NCOREL.[30] The CFD and linear theory results predict a stronger nose-down tendency than does the experimental data. Some of these differences in the pitching moment can be attributed to flow separation from the trailing edge of the wing outboard of the crossflow shock at the larger values of C_L. Since the Euler equations are inviscid flow relations and the parabolized Navier-Stokes equations can not treat streamwise separation, these solutions give a more negative pitching moment than the experimental data. Linear theory predicts the incorrect sign for the zero-lift pitching moment coefficient as well.

The PNS drag coefficient results (Fig. 16) show slightly better agreement with experiment than do the Euler, but both outperform the linear theory results, especially at the larger angles of attack. PNS drag comparisons to the experimental data begin to degrade at an angle of attack around 8°. Oil flow visualizations presented in Ref. 31 reveal that this is the angle of attack at which the flow begins to separate from the tailing edge of the wing. Because linear theory overpredicts both the lift and drag coefficients at a given angle of attack for this wing, plotting the results on a drag polar (Fig. 17) gives

better agreement with experiment. Euler and PNS results still outperform those from linear theory over most of the range of lift coefficients considered, but there is a region near $C_L = 0.35$ where the CFD and linear theory polars cross. This results in a small range of lift coefficients where the linear theory results are as accurate or more accurate than those from CFD. This phenomenon will be seen and discussed further in the studies of HSCT wings and wing-fuselage configurations.

The load distributions (Fig. 18) for this wing at 5.98° angle of attack show the CFD results matching well with experimental data. Euler and PNS solutions yield basically the same pressure distributions. The distributions computed from linear theory give the correct general shape, but do not capture the details as well. This is evident in the $x = 19.9$ curve where the peak and drop in ΔC_p near the leading edge are completely smoothed out. The loads (Fig. 19) for the wing at 12.91° angle of attack show much more dramatic disagreement. Again both the Euler and PNS results do an excellent job predicting the load distribution. In particular, the CFD solutions capture the crossflow shock at this condition. The panel code does not capture the physics of the nonlinear flowfield, and the results are much worse than they were for the lower angle-of-attack cases. While giving good load predictions inboard of the crossflow shock location, linear theory underpredicts the load immediately outboard of this area. In addition, the leading-edge singularity produces a large peak in the leading-edge load which compares poorly to the experimental data and CFD results.

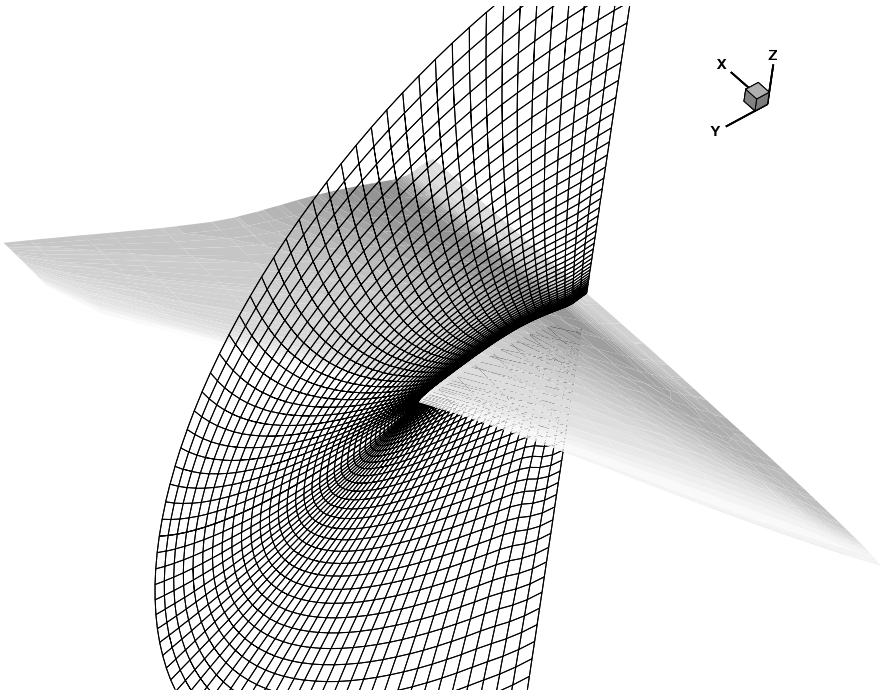

Figure 12: High-Lift Maneuver Wing with Grid Slice

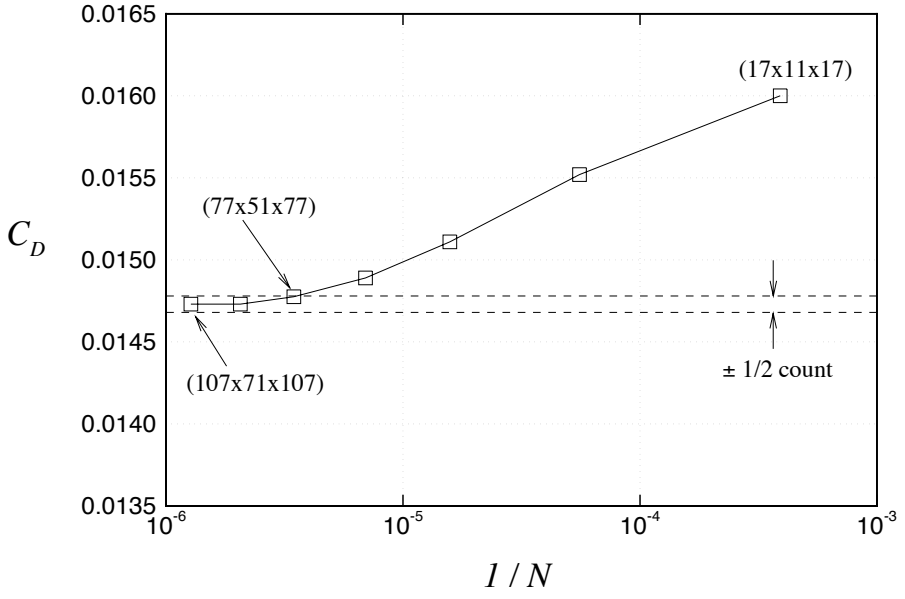

Figure 13: Euler Grid Convergence

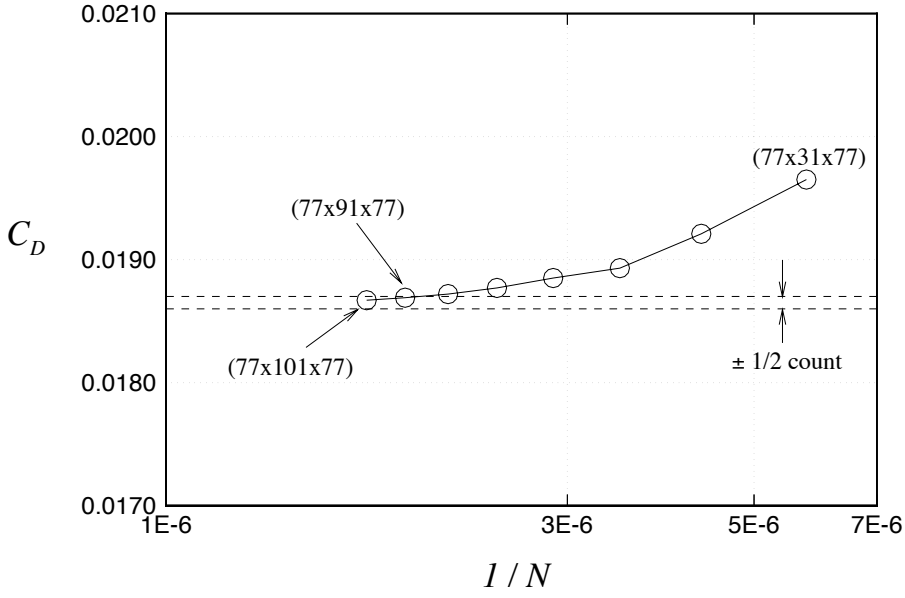

Figure 14: PNS Grid Convergence

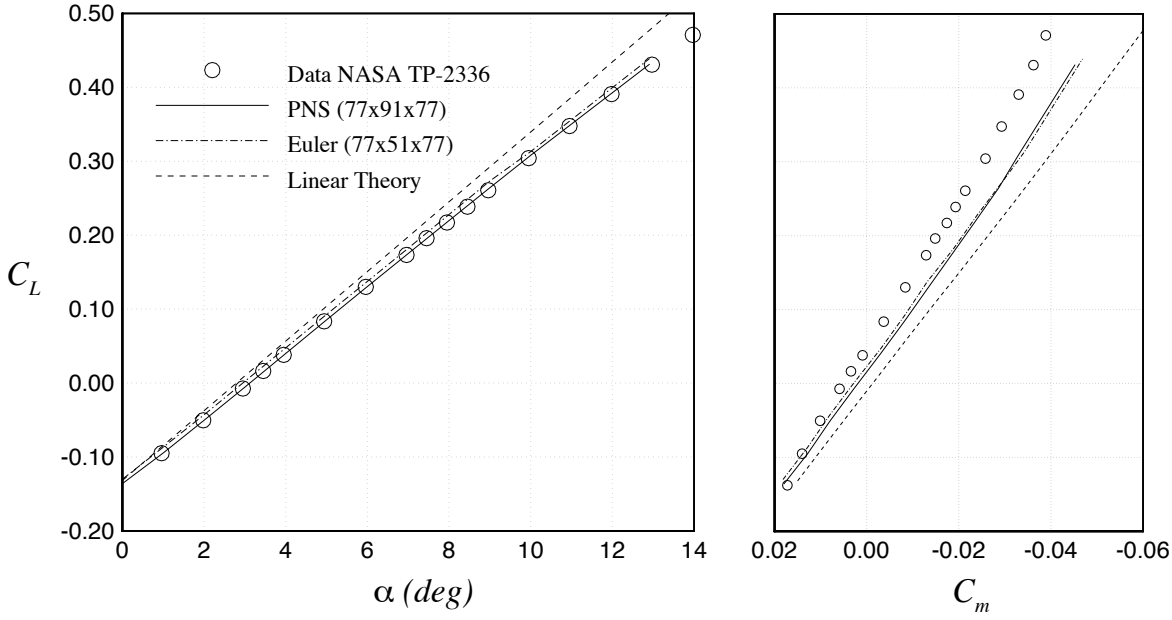

Figure 15: Lift and Pitching Moment Coefficients for Maneuver Wing

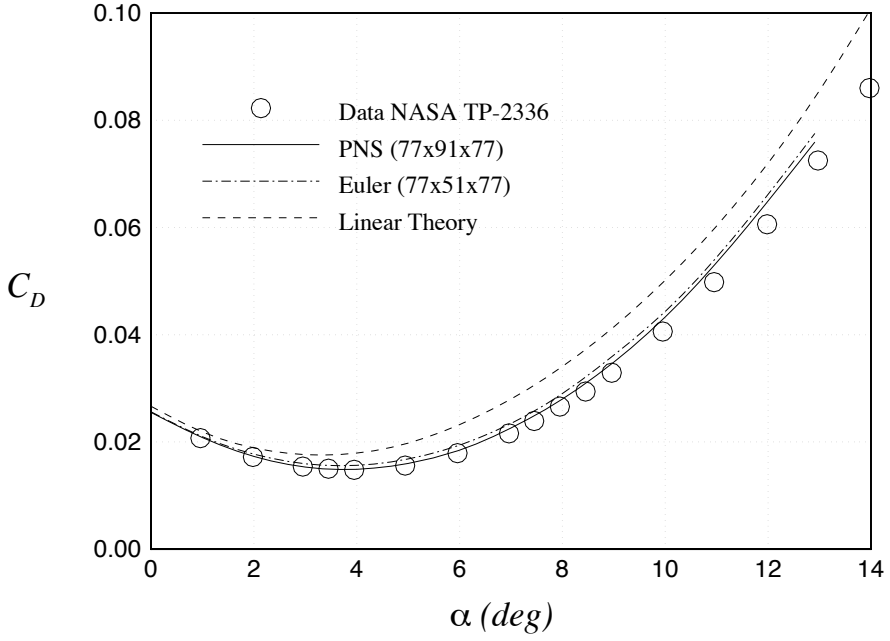

Figure 16: Drag Coefficients for Maneuver Wing

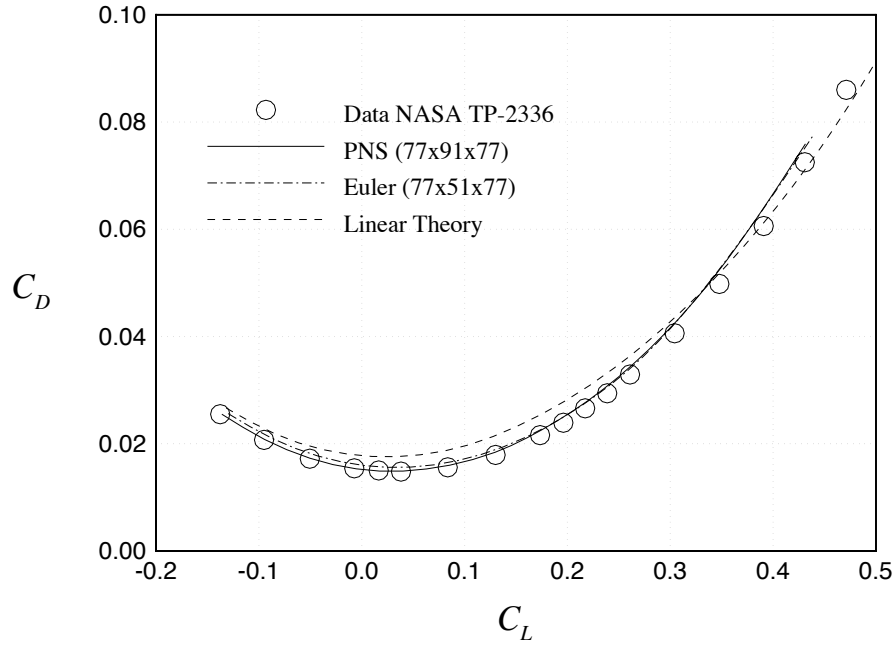

Figure 17: Drag Polar for Maneuver Wing

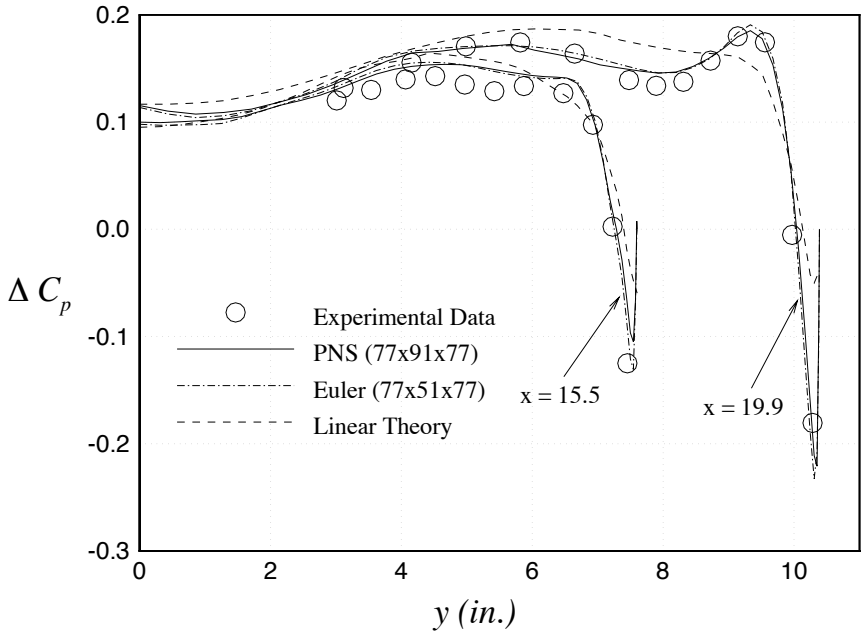

Figure 18: Load Distributions at $\alpha = 5.98°$

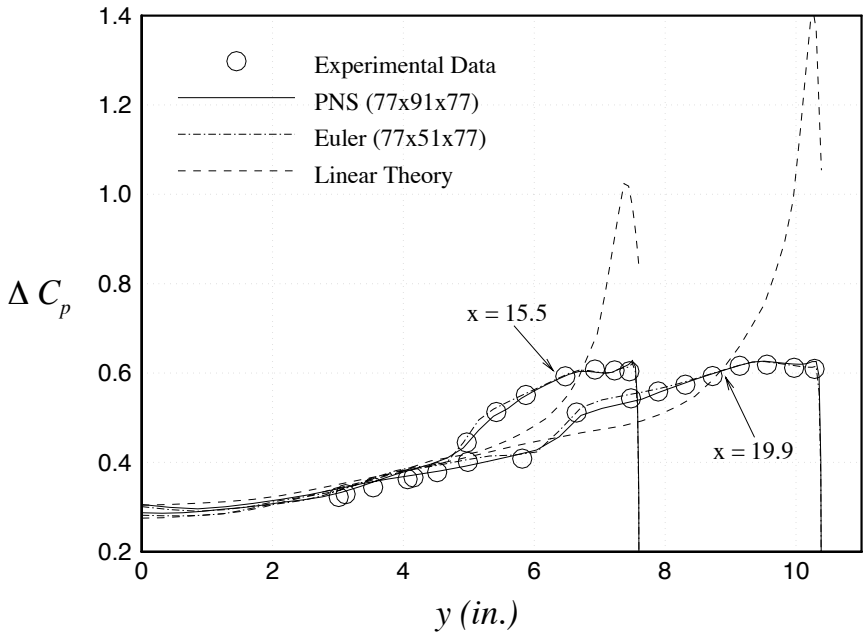

Figure 19: Load Distributions at $\alpha = 12.91°$

3. HSCT Design Studies: Code Certification

The previous sections indicate an opportunity to significantly improve the accuracy of our current aerodynamic predictions by supplementing linear supersonic theory results with Euler or Navier-Stokes solutions. In this section, we discuss the differences in integrated force and moment predictions and distributed loads between linear theory and CFD solutions on three HSCT configurations. The sensitivity of the aircraft range to the predicted drag is determined from analysis. We also determine the effect of the loading differences on the wing bending stresses and the optimized wing bending-material weight. Finally, we perform optimizations with explicit changes to the baseline drag, and discuss how these variations in drag affect the optimized aircraft weight and planform.

3.1. Design Case 1

The first design considered (Fig. 20), which we will call Design Case 1, is a modified version of an early optimal design described in Ref. 4. The original wing planform has been altered so that there is no trailing edge sweep. This allows the grid generator to create a marching grid which models the wing trailing edge exactly. The design variables used to create this configuration are given in Table 1.

Fuselage

We create the fuselage for our HSCT configurations using 8 design variables that define the axial location and radius of the fuselage at four positions. The shape of the body between these points is then determined by considering it as a minimum wave drag body of a fixed volume[1, 35]. The cross-sectional area is given by

$$\begin{aligned} S(\tilde{x}) &= \frac{128V}{3\pi l}\tilde{x}^{3/2}(1-\tilde{x})^{3/2} + l^2\sum_{i=1}^{4}\nu_i\left[\ln\left(\frac{z_{1i}+2z_{2i}}{z_{1i}-2z_{2i}}\right)+\frac{2z_{2i}}{9}\left(9z_{1i}-64z_{2i}^2\right)\right], \\ \text{where}\quad z_{1i} &= \tilde{x}+k_i-2\tilde{x}k_i \quad \text{and} \\ z_{2i}^2 &= \tilde{x}k_i(1-\tilde{x})(1-k_i). \end{aligned}$$

The quantity V is the fixed volume, l is the fuselage length, $\tilde{x}$ is the normalized axial location x/l, and the k_i are the normalized axial locations of the restraints. The constants ν_i are determined by solving the 4×4 linear system resulting from this equation applied at the four restraint locations. The fuselage shape is shown in Figure 21. The plot shows the reduced area in the fuselage mid-section, which gives improved area ruling of the wing-fuselage configurations.

In contrast to the Haack-Adams bodies studied earlier which have fineness ratios of 7 and 10, the HSCT fuselages are more slender with typical fineness ratios of $l/d_{max} = 25$. In addition, we have non-dimensionalized the HSCT fuselage wave drag using the wing area instead of the maximum fuselage cross-sectional area. These two factors result in much smaller differences between the Harris code and Euler predicted wave drag coefficients (Fig. 22) than were seen in the Haack-Adams study. The minimum difference between the Euler calculations on a 41×81 (*normal*×*axial*) grid and Harris wave drag is approximately 0.8 counts of drag near Mach 2.0. The maximum difference in the Euler and Harris code predictions of the wave drag over the Mach number range studied is 2.0 counts.

Uncambered Wing-Alone Configuration

We now investigate the forces and moments on the uncambered Design Case 1 wing at Mach 2.4 flight conditions. The integrated force and moment data reveal many of the same trends present in the maneuver wing results. Linear supersonic theory results show a 4.7% overprediction of the lift-curve

slope (Fig. 23). The pitching moment coefficients taken about the quarter chord of the MAC show differences of about 0.006 at $C_L = 0.2$. The pitching moment curve shows significant curvature. The same behavior is seen in experimental and Euler analyses performed on the Mach 3 HSCT configuration presented in Refs. 10 and 12. The curvature in the pitching moment coefficient is related to movement in the aerodynamic center location with increasing lift. This is apparent in the basic relationship for the aerodynamic center location, $x_{a.c.}$:

$$x_{a.c.} = x_m - \bar{c}\left(\frac{\partial C_m}{\partial C_L}\right),$$

where x_m is the reference point about which the pitching moment, C_m, is taken. Consider the following equation for the pitching moment:

$$C_m = C_{m_o} + C_N\left[\frac{x_m - x_{a.c.}}{\bar{c}}\right], \tag{1}$$

where C_{m_o} is the zero-lift pitching moment and C_N is the normal force coefficient. For an uncambered wing

$$C_{m_o} = 0 \quad \text{and} \quad C_N = \left(\frac{\partial C_N}{\partial C_L}\right)C_L.$$

Figure 24 shows the variation in the aerodynamic center with increasing lift coefficient. Because the wing is uncambered, the center of pressure and aerodynamic center locations are equivalent. The figure shows that the change in $x_{a.c.}$ is nearly linear. Using this assumption, an equation for the $x_{a.c.}$ in terms of C_L can be written as:

$$x_{a.c.} = x_{a.c._O} + \left(\frac{\partial x_{a.c.}}{\partial C_L}\right)C_L,$$

where $x_{a.c._O}$ is the aerodynamic center location at zero lift. Substituting the relations for C_{m_o}, C_N, and $x_{a.c.}$ into Eqn. 1 gives the final equation for the pitching moment of an uncambered wing:

$$C_m = \left[\left(\frac{\partial C_N}{\partial C_L}\right)(x_m - x_{a.c._O})\frac{1}{\bar{c}}\right]C_L - \left[\left(\frac{\partial C_N}{\partial C_L}\right)\left(\frac{\partial x_{a.c.}}{\partial C_L}\right)\frac{1}{\bar{c}}\right]C_L^2. \tag{2}$$

The ratio of the quadratic to linear terms is

$$\frac{\textit{quadratic term}}{\textit{linear term}} = \frac{\left(\frac{\partial x_{a.c.}}{\partial C_L}\right)}{x_m - x_{a.c._O}}$$

For this wing, the ratio is 2.6 which explains why the pitching moment coefficient plot shows noticeable curvature. When the distance between the aerodynamic center and moment reference point is much larger than the change in the aerodynamic center location, the moment is lift-driven and behaves linearly, however when this is not the case, the movement in the aerodynamic center produces curvature in the pitching moment curve. For this wing, the aerodynamic center travels from 53.3% of the root chord, c_o, at $C_L = 0.0$ to 52.7% at $C_L = 0.2$. The aerodynamic center locations are based on the root chord to present the results in a consistent manner with those in Ref. 36. The aerodynamic center locations for this wing are close to those presented in Ref. 36 for a similar family of diamond-shaped wings. The quarter-chord of the MAC for this wing lies between the linear theory and CFD aerodynamic center locations. The Euler and PNS $x_{a.c.}$ are located about 3.5 *ft* aft of that from linear theory, resulting in a more negative pitching moment. This is a different trend than is seen in the maneuver wing studies and in studies of other HSCT configurations by Pittman[10] *et al.* and by Hollenback and Blom[9].

Figure 25 shows good agreement between the PNS drag and the Euler drag predictions with algebraic skin friction corrections. As expected, the Harris wave drag results on this nominally 2.5% thick wing show closer agreement than those for the 9.0% thick Squire wing. At Mach 2.4, the slender-body theory

prediction for the zero-lift wave drag, $C_{D_{OW}}$, is 1.4 counts higher than that calculated using CFD. The algebraic skin friction estimate predicts a viscous drag coefficient of 0.00290. This is 0.9 counts higher than the PNS prediction of 0.00281 at zero angle-of-attack. For this wing, the simple skin friction estimate gives a viscous drag value within 3.2% of the PNS value. Linear supersonic theory overestimates the zero lift drag for this wing, but underestimates the induced drag. This is evident because the linear theory drag polar crosses the CFD drag polars, resulting in good comparisons at the cruise C_L of 0.070. This behavior is similar to that seen in the maneuver wing drag polar (Fig. 17), but it is more significant since the cross-over occurs near the cruise C_L. The linear theory estimate is only 0.6 counts higher than the PNS result. The differences in the drag coefficient estimates become much worse at larger values of the lift coefficient.

On an SGI Power Challenge R8000, the PNS computations take 1.25 hours (0.008 sec/cell) at the lower angles of attack and 2.5 hours (0.017 sec/cell) at the larger angles of attack. This results from the need to decrease the time step to converge the solution at the higher angles of attack. On the same machine, the Euler calculations approximately 18 minutes (0.004 sec/cell), while the linear supersonic theory results only take one second. These times are typical for all of the wing-alone computations performed for this study.

Cambered Wing-Alone Configuration

The optimal camber for our HSCT designs is determined using the linear theory code WINGDES.[37] WINGDES attempts to find the camber distribution along the wing which minimizes the drag-due-to-lift. Two runs of WINGDES per wing were required to get the proper camber distribution. The second run served to smooth the camber distribution and provide the maximum leading-edge suction parameter closer to the design lift coefficient.

The lift, pitching moment, and drag coefficient results for the Design Case 1 cambered wing configuration are given in Figures 26 and 27. Linear theory again overpredicts C_L and C_m, and there is an additional error in these quantities at zero angle-of-attack due to the wing camber. The curvature in the pitching moment due to movement in the aerodynamic center location is still present. The linear theory drag is fairly accurate at the lower lift values. The cambering of the wing did result in a reduction of the drag at cruise. From linear theory analysis, the drag coefficient for the cambered wing is 1.8 counts lower than for the uncambered wing. The improvement is not quite as good when the drag coefficient is computed using the Euler and PNS equations. PNS solutions show a 0.9 count reduction, and Euler results show a 0.6 count reduction in the cruise drag. The algebraic skin friction estimate is 0.7 counts higher than the PNS viscous drag value. For the Design Case 1 cambered wing, the difference between the linear theory and PNS predicted cruise drag coefficients is 0.3 counts. At this condition, the overestimate of the zero-lift drag is almost completely cancelled by the underestimate in the induced drag.

Wing-Fuselage Configuration

Force and moment predictions from CFD on the cambered wing-fuselage configuration are now compared with those from linear supersonic theory. Another grid convergence study is performed to ensure a converged PNS solution. Figure 28 shows the convergence of the drag coefficient with mesh for the body in a Mach 2.4 flow at 4°angle of attack. A 91×91×91 grid gives the drag coefficient within 1/2 count of the solution extrapolated to zero mesh spacing. Boundary layer profiles (Fig. 29) on the wing and fuselage show that there are 3–4 cells in the laminar sublayer with the first cell center having $y^+ < 1.0$. Solutions on this mesh took approximately 3 hours and 20 minutes (0.0165 sec/cell) on an

SGI Power Challenge R8000. Comparing this wing-fuselage grid with that required for converged wing-alone PNS calculations, we find that additional spanwise and lengthwise points are required to properly resolve the fuselage, while the number of points normal to the body remains the same. Since the grid convergence studies for the maneuver wing (Section 2.3) show that reducing the number of cells in the normal direction from the grid for converged PNS calculations by 40 gives a grid suitable for converged Euler results, a 91×51×91 grid is chosen for the wing-fuselage Euler calculations without an additional grid convergence investigation. Computations on this mesh required about 35 minutes (0.005 sec/cell) of CPU time.

The linear theory drag-due-to-lift code does not handle a fuselage. The wing is simply extended to the fuselage centerline, as it is for the wing-alone studies. For this reason, the effects of adding the fuselage will only be seen in the wave drag and skin friction components of our linear supersonic theory drag. The lift-curve slope (Fig. 30) for the wing-fuselage configuration shows worse agreement between linear theory and CFD than is seen in the wing-alone configurations. Our linear theory code does not predict the drop in C_{L_α} due to the presence of the fuselage. The pitching moment differences remain about the same as in the wing-alone configuration. The drag polar (Fig. 31) also shows larger discrepancies than were previously seen. At cruise, the difference between the linear supersonic theory drag coefficient and that from PNS is 1.3 counts. The algebraic skin friction estimate is only 0.4 counts higher than the PNS viscous drag. Unlike the wing-alone cases, the zero-lift drag predicted from linear theory is lower than that from CFD. This causes the errors in the zero-lift and induced drag components to add to instead of subtract from each other at cruise.

The effect of the 1.3 count difference in drag predictions between linear theory and CFD on HSCT performance is assessed for this wing. While linear supersonic theory predicts the cruise drag within 2.0%, the small differences present have a large effect on the aircraft range. The increase in range resulting from an 1.3 count underprediction in the drag predicted from linear theory is 73 $n.mi.$ This corresponds to a sensitivity for this design of 56 $n.mi.$ per drag count.

Loads and Structural Optimization

We now shift our attention from the integrated forces and moments to the distributed loads predicted from linear theory and Euler calculations. Loads from parabolized Navier-Stokes calculations are not presented since we found little difference between the pressure fields from our viscous and inviscid analyses. In the multidisciplinary design optimization, the constraints for the structural optimization are evaluated at a number of load cases including taxi, transonic climb, low-speed cruise, high-speed cruise, and high-speed pull-up. For this study we will concentrate on three supersonic loads cases: Mach 2.4 cruise, 2.5-g pull-up at Mach 2.4, and Mach 1.2 cruise. The effect of differences in the loads on the Von Mises equivalent stresses is determined at these three conditions. Structural optimizations are then performed using the supersonic loads from Euler solutions and from linear theory analyses to determine the sensitivity of the wing bending material weight to the accuracy of the predicted loads.

The loads computed from linear theory and Euler calculations on wing-alone and wing-fuselage configurations are presented for comparison. Cruise at Mach 2.4 for Design Case 1 is achieved with a lift coefficient of 0.070. The loads at this condition (Fig. 32) show good agreement over most of the wing. Little variation is seen between the wing-alone and wing-fuselage loads. There is a slight peak in the linear theory loads at the wing trailing-edge cut, but this is a difference of only about 0.02 in ΔC_P.

The wing model used for the structural optimization is shown in Figure 33. Figure 34 shows contours of the difference in wing bending stress computed from Euler and linear theory loads. The difference in stresses is negative over most of the wing, indicating that the stresses computed from Euler loads are

lower. The largest magnitude difference in stress occurs on the lower wing surface in a region inboard of the leading-edge break. The value of this maximum stress difference (Table 2) is -1971 *psi*, which represents 37.0% of the nominal value. The percentage variation in the maximum stress is lower at 23.6%, but is still high considering the agreement in the loads. Searching for explanations to this relatively large discrepancy led us to look at the predicted center of pressure location. The spanwise location of the center of pressure calculated from Euler analysis is 1.53 *ft* inboard of that computed from linear theory on a wing with a semi-span of 75.9 *ft*. This gives insight into why the Euler loads result in a wing with lower bending stress values. The sensitivity of the stresses to the predicted loads comes from the large amounts of fuel stored in the wings of our HSCT designs. Inertial relief from the fuel weight cancels much of the wing bending due to aerodynamic loading. This causes the wing bending stresses to become very sensitive to small changes in the loading and the spanwise location of the center of pressure.

The Mach 1.2 cruise load condition is examined next. Cruise at this Mach number is obtained with a lift coefficient of 0.071. The Euler solution to the wing-fuselage configuration at Mach 1.2 cruise could not converge. The reason for this failure is the semi-vertex angle of the fuselage nose. For a free stream Mach number of 1.2, the limiting cone semi-vertex angle which retains supersonic flow after the shock is 14.1°. For comparison, at Mach 2.4 this maximum angle is 41.5°. This particular fuselage has a semi-vertex angle of 24°, which is not only larger than the maximum angle for supersonic flow after the shock, but it is also larger than the limiting deflection angle for an attached shock. This illustrates an important physical limitation of using a space-marching approach to CFD solutions on our HSCT designs. The wing-alone Euler calculations were successful, and the results (Fig. 35) compare well with those from linear theory. As with the Mach 2.4 cruise condition, the loads near the trailing edge show the poorest agreement.

The stress comparisons (Fig. 36) for the Mach 1.2 cruise condition show that, overall, the stresses computed from Euler loads are lower than those from linear theory loads. The value of the maximum stress difference (Table 2) is -2710 *psi* which represents 17.3% of the stress value for that element, while the variation in the maximum stress is only -641 *psi* (2.6%). The maximum stress occurs near the leading edge break. The spanwise center of pressure location from Euler analysis is 1.34 ft inboard of that from linear theory.

The Mach 2.4 2.5-g pull-up case ($C_L = 0.154$) gives much more dramatic differences in the loading. The Euler solution (Fig. 37) on the wing and wing-fuselage case reveals the formation of a shock on the upper wing surface. Linear theory loads match well inboard of the shock, but underpredict the load immediately outboard of it. Linear theory also overpredicts the leading edge suction peak along the entire subsonic leading-edge. The subsonic leading edge is that portion ahead of the leading-edge break in which the component of the Mach number normal to the leading edge is subsonic. Similar behavior in the loads is evident in the high angle-of-attack loads for the maneuver wing in Section 2.3. After the wing break, the leading-edge loads predicted from linear theory match better with those from the Euler solutions, however the peak caused by the error along the subsonic leading edge propagates and results in the peak seen at the aft-most wing station.

The effects of the differences in aerodynamic loading can be seen in the structural analysis of the aircraft. As expected, we find that the largest magnitude difference in stresses (Table 2) computed from linear theory and Euler loads occurs for the Mach 2.4 2.5-g pull-up condition. The maximum difference in predicted stresses is 25.5% and the variation in the maximum stress is 16.7%. The maximum stress again occurs near the wing leading edge break. As with the previous two cases, the spanwise location center of pressure is farther inboard for the Euler loads. The stresses (Fig. 38) from Euler loads are larger over the small outboard section of the wing, however over the remainder of the wing they are

lower than the stresses found from linear theory loads. As with the other two load cases, the maximum difference in stresses occurs near the middle of the wing. While the regions aft of the leading-edge break show large variations in the aerodynamic loading from Euler and linear theory results, they also have inertial loading from the nacelles. These inertial effects appear to explain why the maximum difference in stress does not occur farther aft on the wing.

The overall effect of these differences on the structural optimization is an optimal design whose wing bending-material weight is 5.6% lighter by using the Euler loads instead of the linear theory loads. The magnitude of the difference in bending-material weight is 1181 *lb*. The lower stress values from using Euler loads have resulted in a lighter wing. However, in spite of the difference in loads for the Mach 2.4 2.5-g pull-up and the relatively large variations in stresses for all load cases, the optimized wing-bending material weight only shows a small change.

Table 1: Design Case 1 Design Variables

DV	Value	Description
1	181.00	Wing Root Chord ($ft.$)
2	156.00	L.E. Break, x ($ft.$)
3	49.20	L.E. Break, y ($ft.$)
4	181.00	T.E. Break, x ($ft.$)
5	64.00	T.E. Break, y ($ft.$)
6	170.00	L.E. Wing Tip, x ($ft.$)
7	11.00	Wing Tip Chord ($ft.$)
8	75.90	Wing Semi-Span ($ft.$)
9	0.4019	x-Loc. Airfoil Max. t/c (x/c)
10	3.6921	L.E. Radius Parameter
11	2.5789	t/c at Wing Root ($\%c$)
12	2.1594	t/c at L.E. Break ($\%c$)
13	1.8039	t/c at Wing Tip ($\%c$)
14	2.196	Fuselage X-Restraint #1
15	1.0610	Fuselage R-Restraint #1
16	12.200	Fuselage X-Restraint #2
17	3.4961	Fuselage R-Restraint #2
18	132.463	Fuselage X-Restraint #3
19	5.3410	Fuselage R-Restraint #3
20	248.668	Fuselage X-Restraint #4
21	4.6661	Fuselage R-Restraint #4

Table 2: Stress, Center of Pressure, and Bending Material Weight Comparisons

Load Case	$(\Delta\sigma)_{\max}$		$\Delta(\sigma_{\max})$		$\Delta y_{\text{c.p.}}$	$\frac{W_{\text{S/O-Euler}}}{W_{\text{S/O-LT}}}$
	psi	%	*psi*	%	*ft*	
M=2.4 n=1.0	-1971	(37.0%)	-1729	(23.6%)	-1.528	
M=1.2 n=1.0	-2710	(17.3%)	-641	(2.6%)	-1.342	0.944
M=2.4 n=2.5	-4696	(25.5%)	-4341	(16.7%)	-1.218	

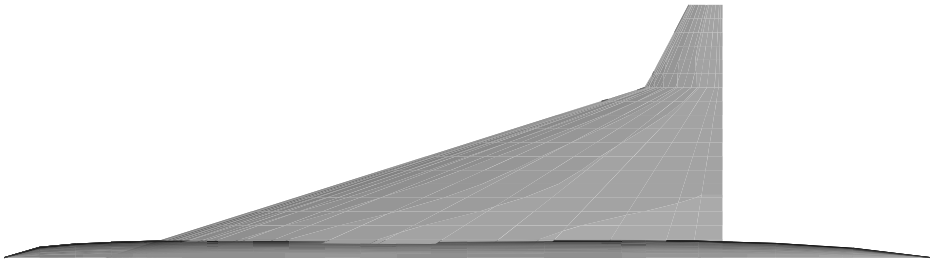

Figure 20: Design Case 1

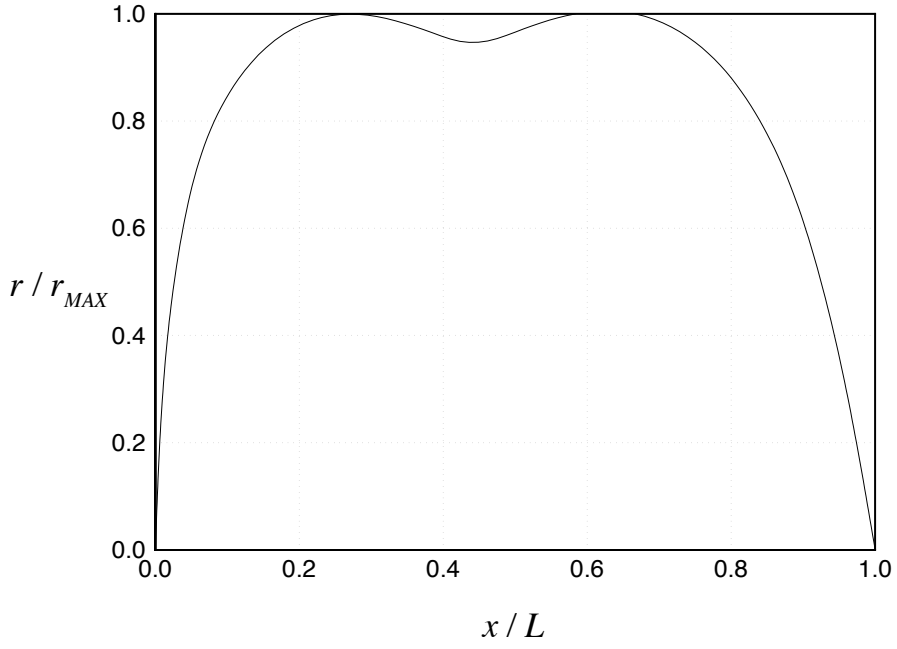

Figure 21: Design Case 1 Fuselage

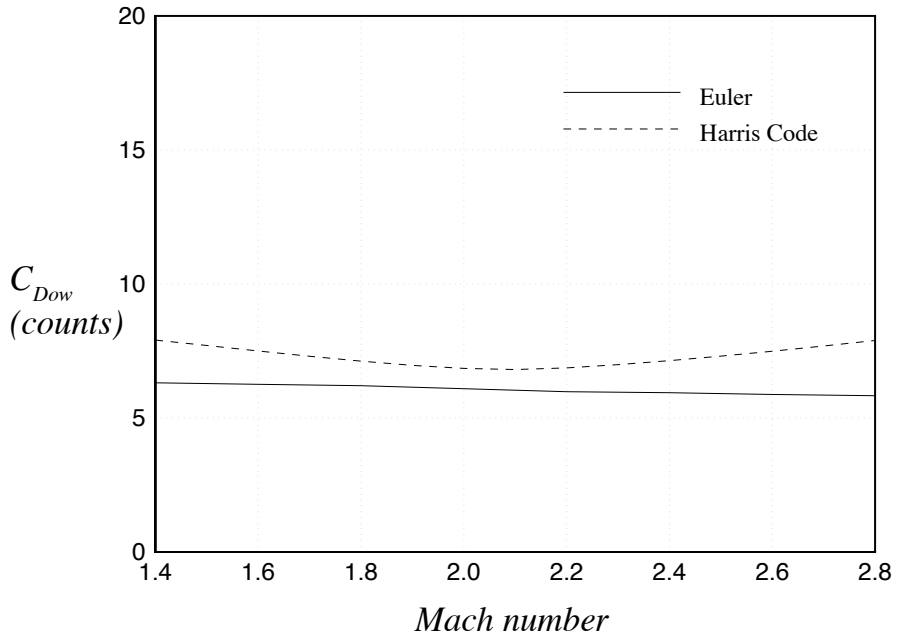

Figure 22: Design Case 1 Fuselage Wave Drag

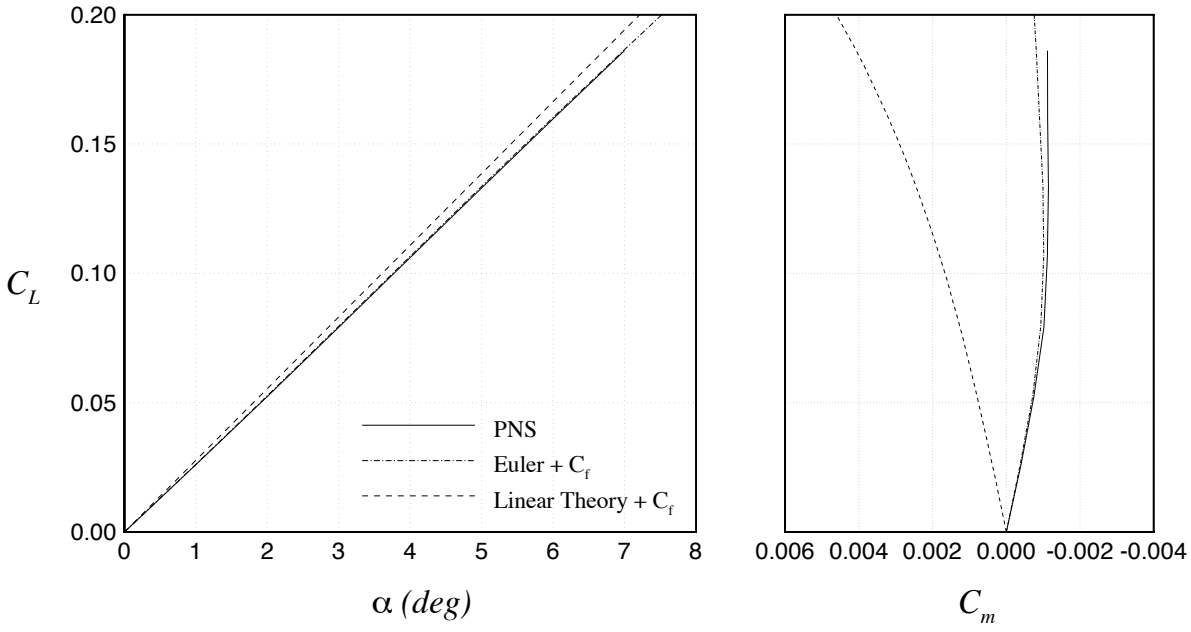

Figure 23: Lift and Pitching Moment Coefficients for Design Case 1 Uncambered Wing-Alone Configuration

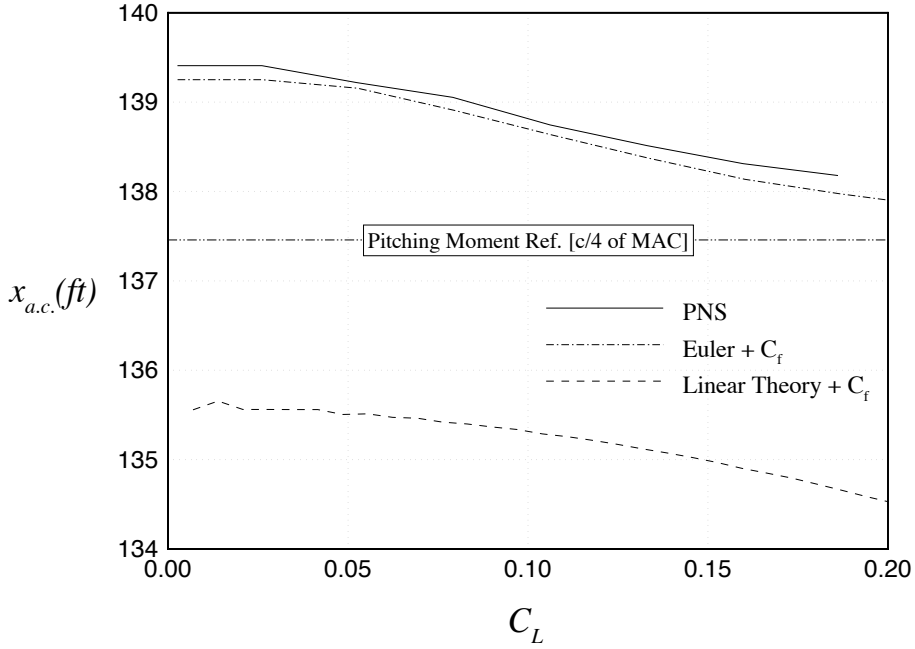

Figure 24: Change in Center of Pressure Location with Lift Coefficient

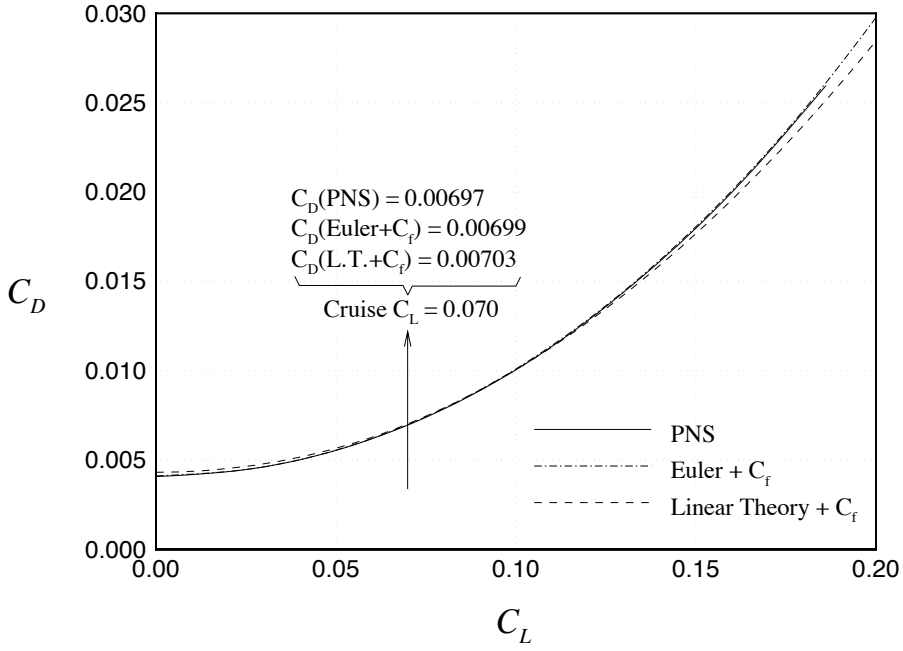

Figure 25: Drag Polar for Design Case 1 Uncambered Wing-Alone Configuration

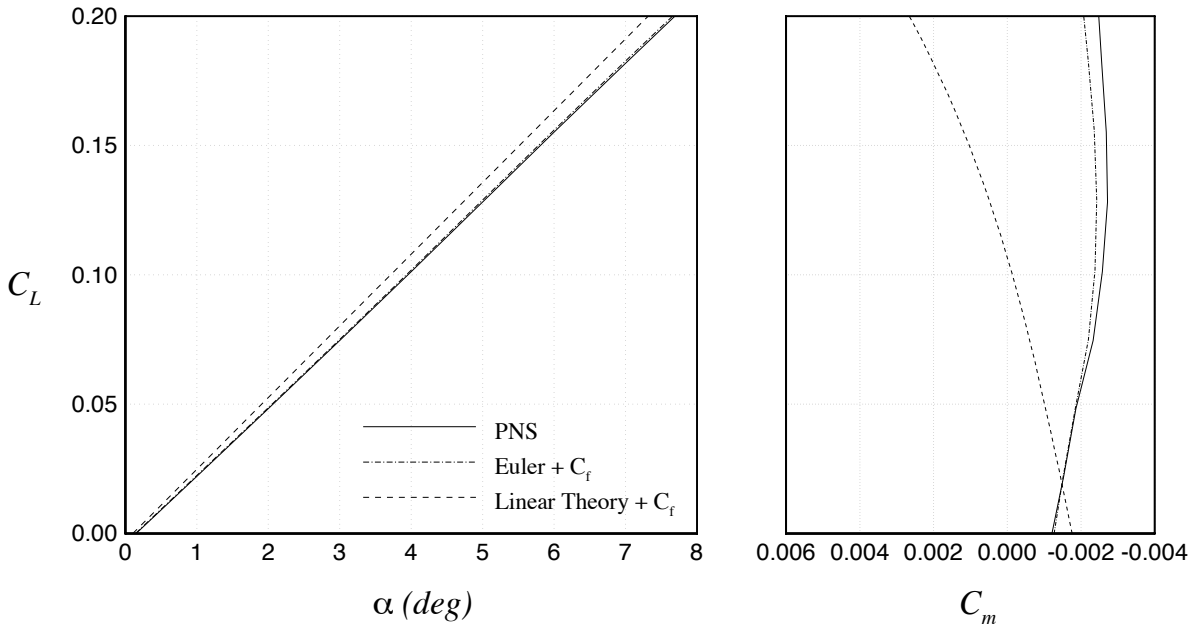

Figure 26: Lift and Pitching Moment Coefficients for Design Case 1 Cambered Wing-Alone Configuration

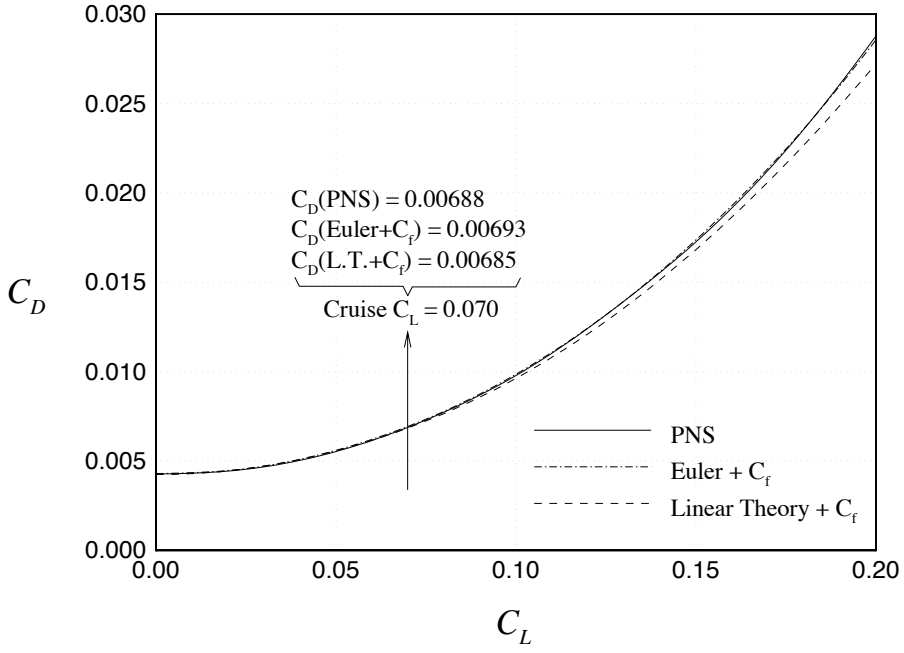

Figure 27: Drag Polar for Design Case 1 Cambered Wing-Alone Configuration

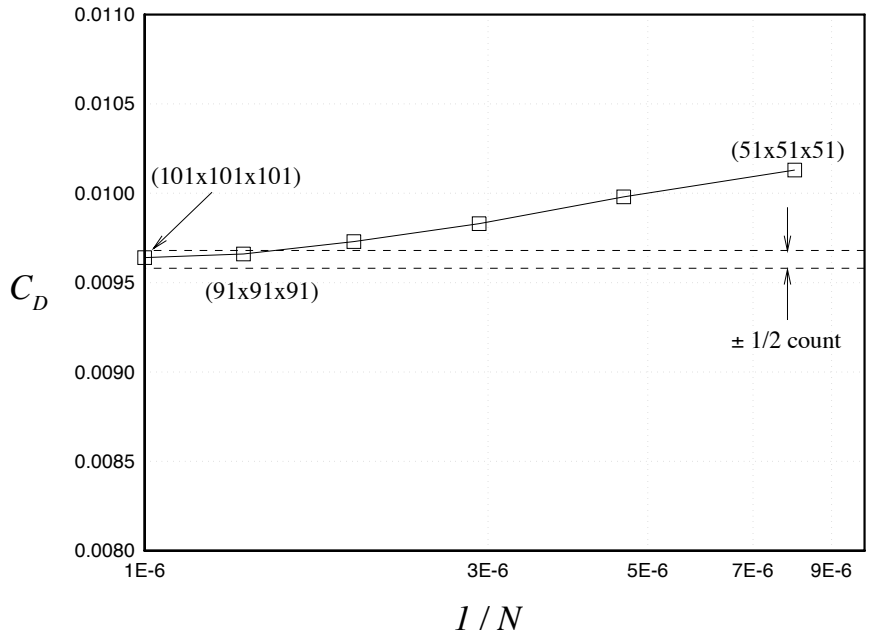

Figure 28: Wing-Fuselage PNS Grid Convergence

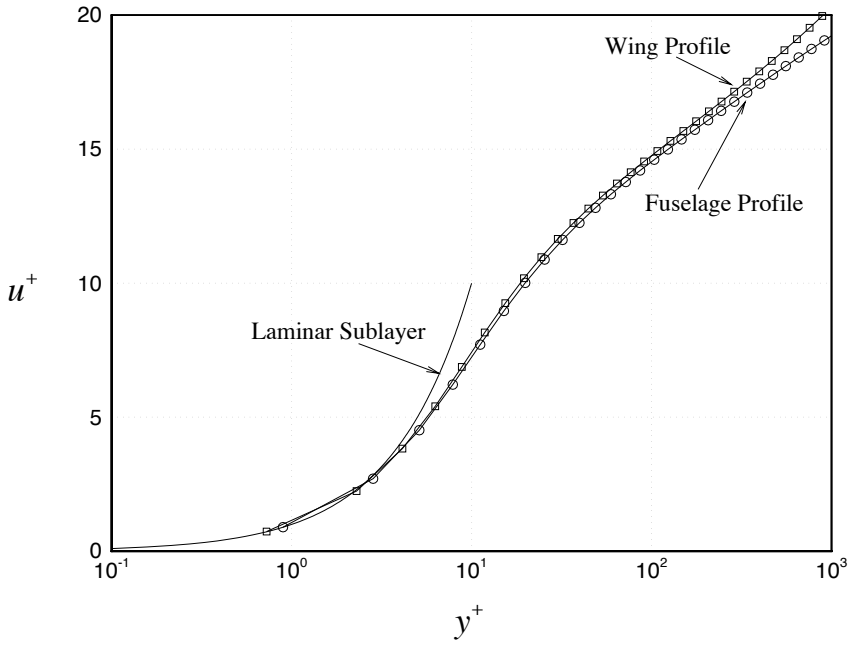

Figure 29: Boundary Layer Profiles

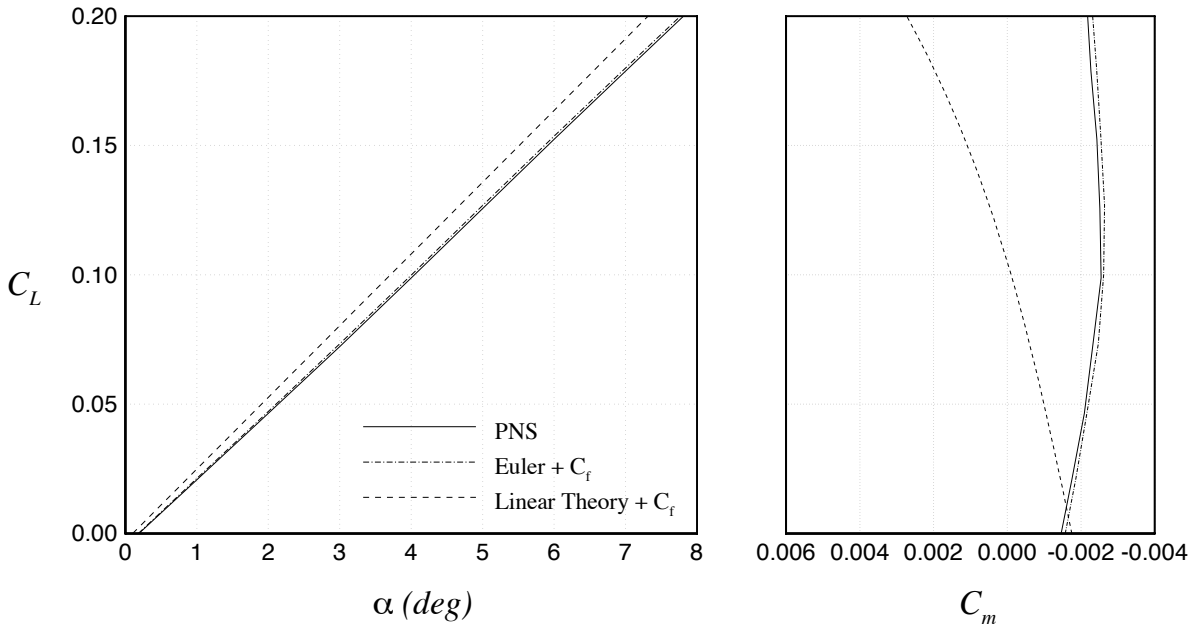

Figure 30: Lift and Pitching Moment Coefficients for Design Case 1 Wing-Fuselage Configuration

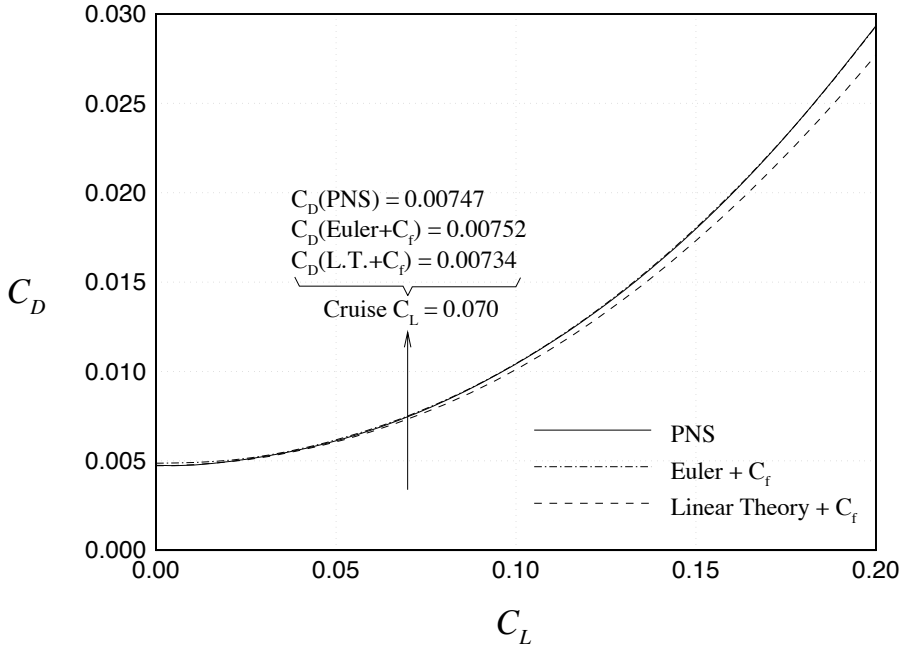

Figure 31: Drag Polar for Design Case 1 Wing-Fuselage Configuration

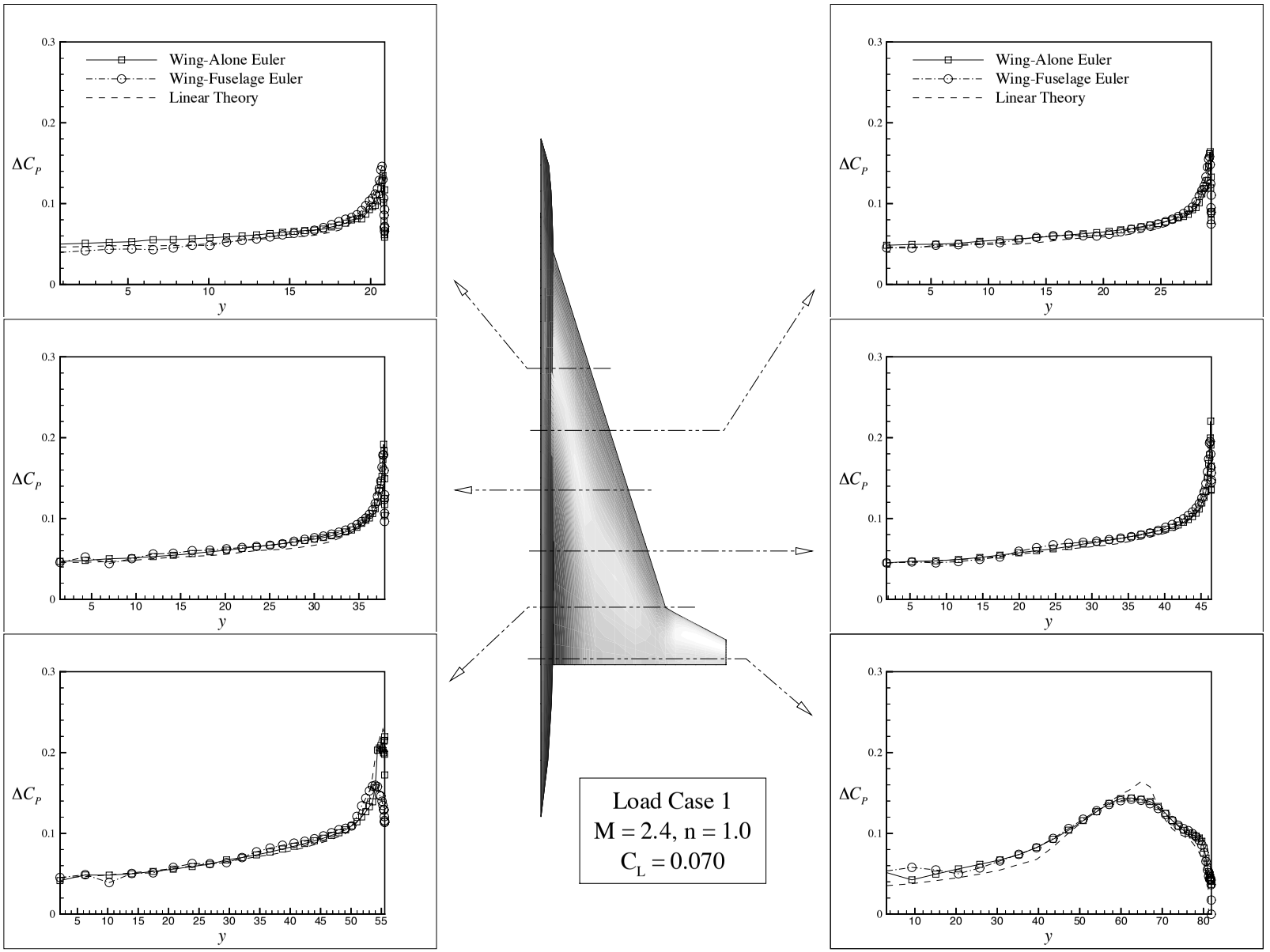

Figure 32: Aerodynamic Loads for Design Case 1 at Mach 2.4 Cruise

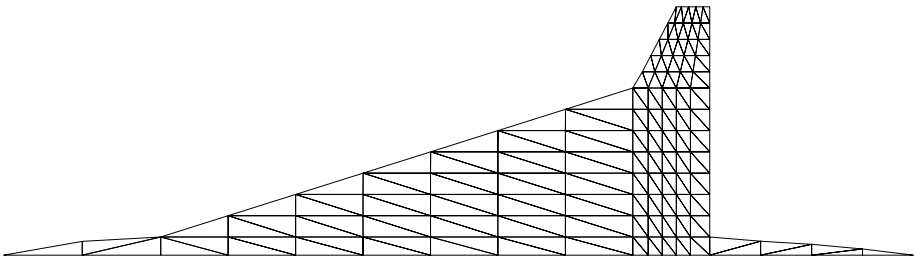

Figure 33: Structural Mesh for Design Case 1

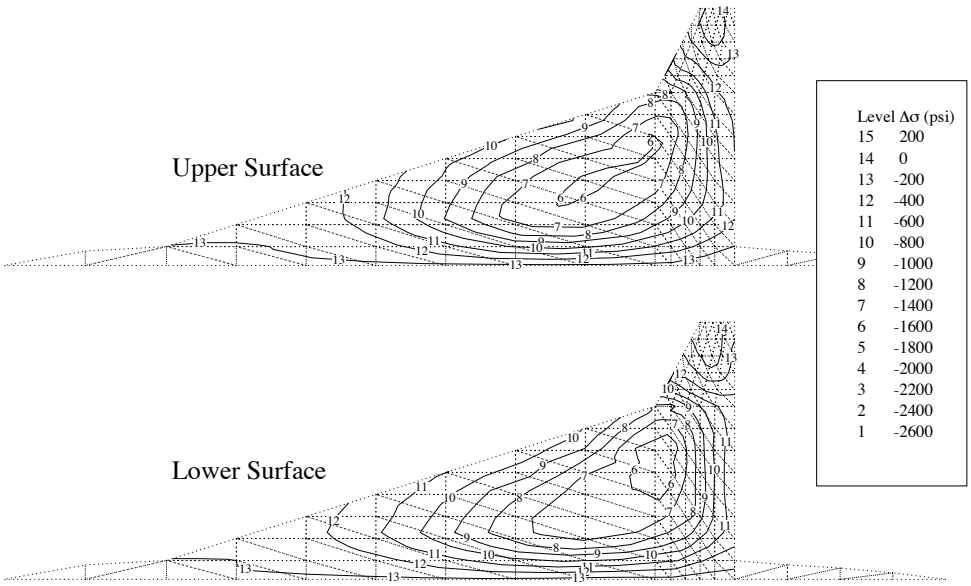

Figure 34: Stress Differences for Design Case 1 at Mach 2.4 Cruise

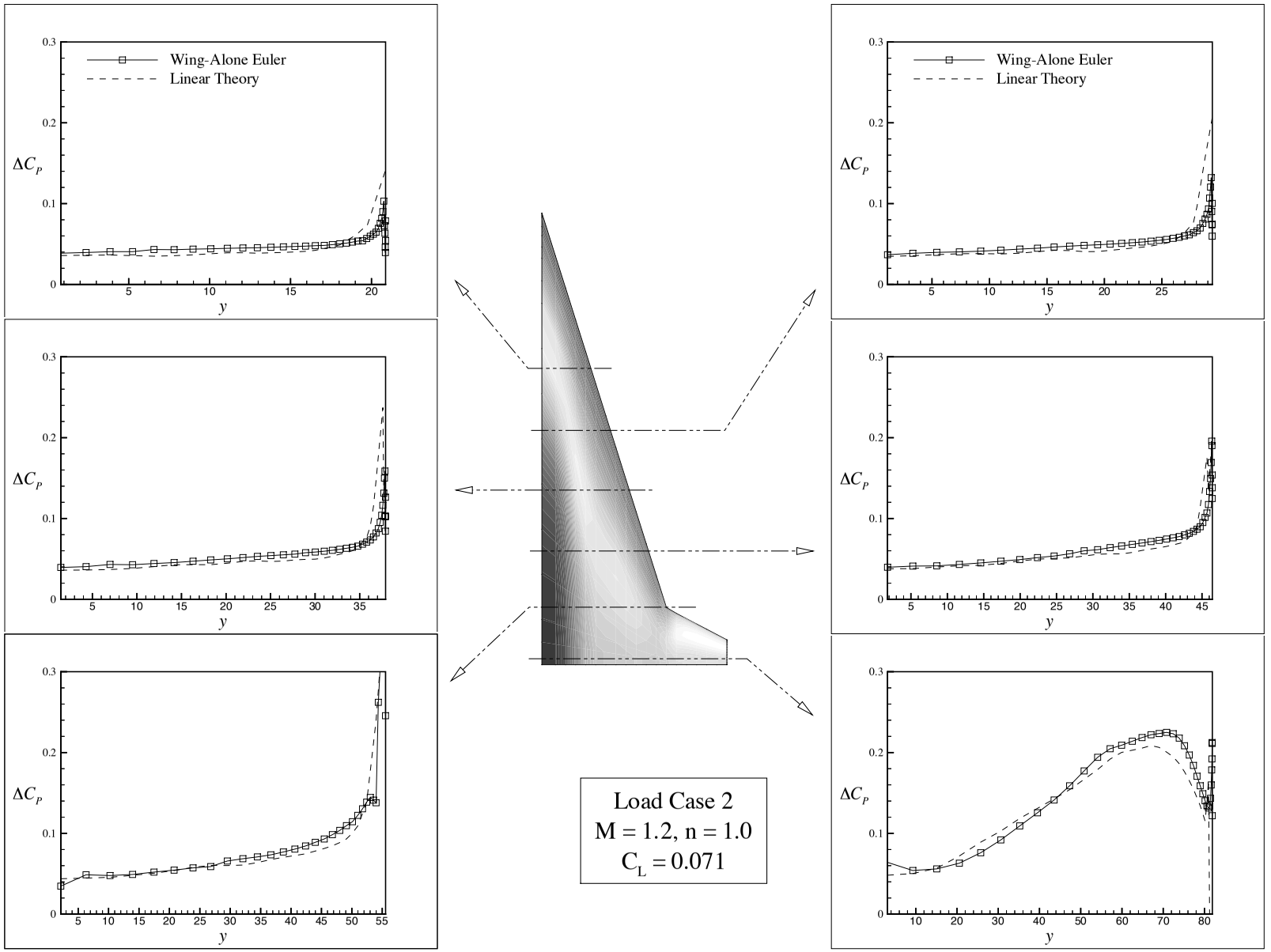

Figure 35: Aerodynamic Loads for Design Case 1 at Mach 1.2 cruise

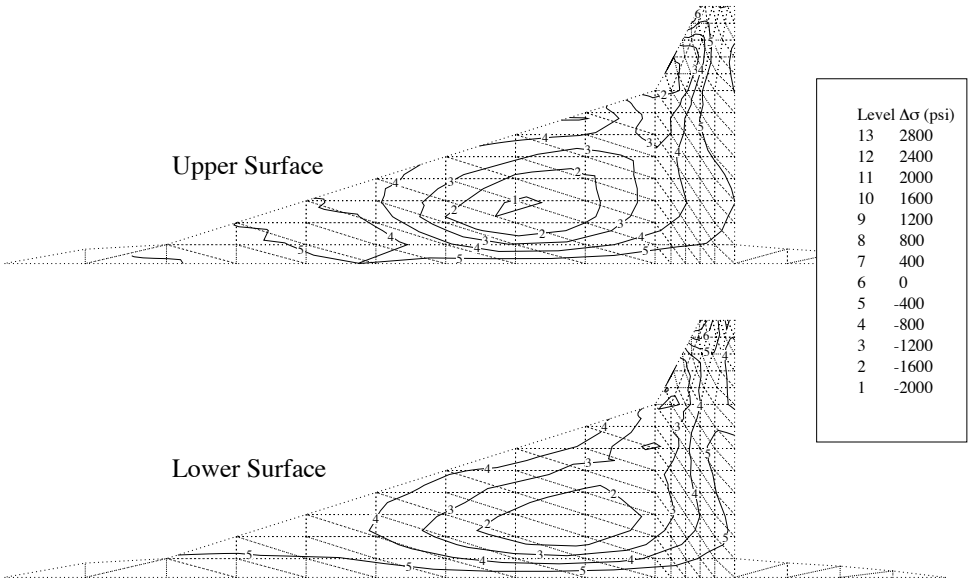

Figure 36: Stress Differences for Design Case 1 at Mach 1.2 Cruise

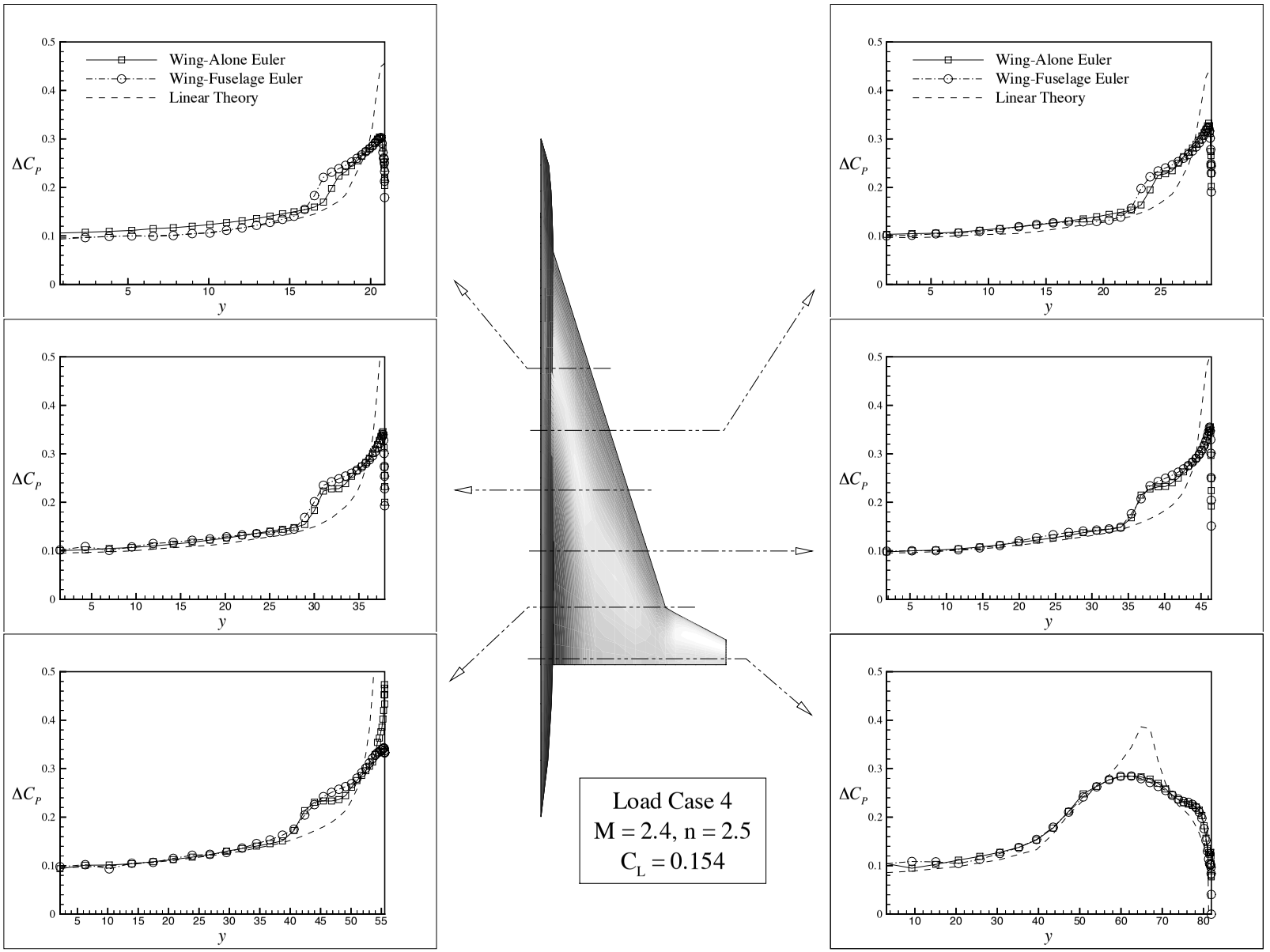

Figure 37: Aerodynamic Loads for Design Case 1 at Mach 2.4 2.5-g pull-up

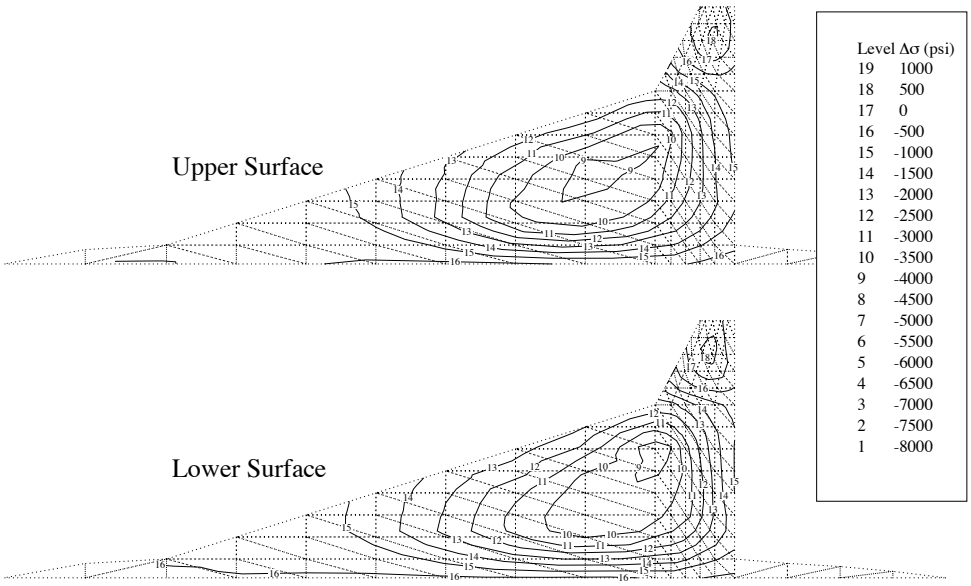

Figure 38: Stress Differences for Design Case 1 at Mach 2.4 2.5-g pull-up

3.2. Design Case 2

The next HSCT design (Fig. 39) presented is an optimal design with an unusual planform. A full description of the optimization is given in Ref. 38. This type of planform with a forward-swept trailing edge has been encountered in other HSCT optimizations.[3, 38] Table 3 contains the design variables which describe the wing and fuselage geometry.

Uncambered Wing-Alone Configuration

For the uncambered wing-alone configuration, linear theory gives an overprediction in the lift and pitching moment coefficient (Fig. 40) compared to CFD solutions. Unlike the previous design, the pitching moment curves behave linearly. Taking the ratio of the quadratic and linear terms of the pitching moment relation (Eqn. 2), as is done in Section 3.1, gives $(\textit{quadratic term}/\textit{linear term}) = 0.27$. The linear term is therefore overshadowing the quadratic term in the pitching moment equation. Another way to look at this is that the effect of the moment arm for the normal force is much larger than the effect due to the movement in the aerodynamic center location. This is illustrated in Fig. 41. The aerodynamic center travels from 33.1% c_o at $C_L = 0.0$ to 32.7% c_o at $C_L = 0.2$. The forward sweep of the trailing edge has resulted in a more forward position of the aerodynamic center compared to Design Case 1. This trend is consistent with the diamond wing studies presented in Ref. 36. The aerodynamic center location predicted from CFD is 4.0 *ft* aft of that from linear theory.

The drag polar (Fig. 42) shows linear theory underestimating the PNS drag coefficient by 1.4 counts at the cruise C_L of 0.082. This comes mostly from the 1.2 count underprediction in the linear theory induced drag. The skin friction estimate is 0.9 counts higher than the viscous drag predicted from the PNS solution.

Cambered Wing-Alone Configuration

Cambering the wing again results in a reduced cruise drag coefficient. Linear theory predicts a 1.5 count improvement, Euler analysis gives a 1.3 count reduction, and PNS calculations show a 0.9 count improvement in the cruise drag due to wing cambering. The agreement between the linear theory and CFD lift coefficient values (Fig. 43) is slightly worse for the cambered wing. The linear theory zero-lift pitching moment coefficient is more negative, but the slope of the curve is more positive than that from Euler and PNS. The drag coefficients (Fig. 44) also show worse agreement between CFD and linear theory than for the uncambered wing. Linear theory calculations give a drag coefficient which is 2.1 counts lower than that from PNS. This is a 2.7% error compared to the PNS prediction of the cruise drag. The viscous drag estimate compares well to the PNS values for this wing.

The sensitivity of the range to the computed drag coefficient is 60 *n.mi.*/count for this design. This indicates that linear supersonic theory is overestimating the range by 126 *n.mi.* This is a significant error in an aircraft with a required 5500 *n.mi.* range constraint. Linear theory estimates of the cruise drag, while having relatively small errors, are not sufficient for accurate aircraft range calculations.

Wing-Fuselage Configuration

Comparison of the force and moment data for the wing-fuselage configurations show the same basic trends as seen in the previous cases. The largest difference between linear theory and CFD lift and pitching moment coefficients (Fig. 45) occurs for this configuration. The PNS computed drag coefficient (Fig. 46) is 0.7 counts higher than the linear supersonic theory value. Surprisingly, this is less than the difference seen in the wing-alone cases. The reason is the larger overprediction in the zero-lift drag value which tends to cancel the induced drag errors.

Loads and Structural Optimization

The distributed loads on Design Case 2 computed from linear theory and Euler analyses reveal similar comparisons to those from Design Case 1. The loads (Fig. 47) on the body at Mach 2.4 cruise compare well. The wing-fuselage loads show a drop in ΔC_P due to the shock formed at the wing-fuselage juncture impinging on the fuselage. Over the remainder of the wing, the wing-alone and wing-fuselage loads do not differ significantly.

The mesh used for the Design Case 2 structural analysis is shown in Figure 48. Figure 49 reveals that the location of the maximum variation is inboard of the subsonic leading edge. Using Euler loads results in lower wing bending stresses over the inboard wing and larger ones over a region of the outboard section. The maximum stress difference (Table 4) for the Mach 2.4 cruise condition is -706 *psi*, which is 25.2% of the stress value over that element. The difference in the maximum stress predicted from the Euler and linear theory loads is 5.0%. This is a smaller stress difference than for Design Case 1, and it is accompanied by a reduction in the difference between the predicted spanwise center of pressure locations.

Euler calculations on the wing-fuselage configuration at Mach 1.2 cruise did converge for this design. The fuselage nose half-angle is 13.9°, which is lower than the maximum deflection angle for supersonic flow after the shock. The Mach 1.2 cruise loads (Fig. 50) from Euler and linear theory agree well at the chordwise locations examined.

The differences in predicted stresses for the Mach 1.2 cruise case are shown in Figure 51. Although the stresses from the Euler loads are lower than those from linear theory over most of the wing, there is a large region over the rear of the wing where the stresses from Euler are larger. The maximum difference between the stresses is -2049 *psi*. Again, we see an improvement in the agreement in stresses and the predicted center of pressure location (Table 4) compared to the Design Case 1 wing. The value of the nominal stress is small over the element where the maximum difference in stress occurs. This results in the large 49.0% relative error observed. The percent error in the maximum stress is smaller at 15.5%.

As expected, the loads for the Mach 2.4 2.5-g pull-up (Fig. 52) show the largest variation. Linear theory loads agree well inboard of the crossflow shock location, except for the area where the shock is impinging on the fuselage. For this design, a double shock is present in the wing-fuselage case. As is seen in the maneuver wing and Design Case 1 loads, linear theory underpredicts the load near the crossflow shock and then overpredicts the load at the leading edge. This peak in the leading edge load propagates down past the leading-edge break.

The largest difference in predicted stresses also occurs for the Mach 2.4 2.5-g pull-up load case. Contours of the difference in predicted stresses (Fig. 53) shows the same behavior as seen in the previous cases, where the Euler loads give lower stress values over most of the inboard section, with the maximum difference occurring near the center of the wing. Over the outboard wing section, the stresses from Euler analysis are typically higher than from linear theory. The percent difference in maximum stress is only 6.3%. The maximum stress is location near the leading edge break for all three load cases. As with the other load cases, the spanwise center of pressure location (Table 4) and wing bending stresses computed from Euler and linear theory loads show better agreement for Design Case 2 than for the Design Case 1.

The wing bending material weights from the structural optimization show the effect of the improved agreement in stresses. The ratio of the wing bending material weight predicted from Euler loads to that from linear theory loads is 0.971. A lighter design is obtained using the more accurate loads, but the overall difference is extremely small (325 *lb*).

Table 3: Design Case 2 Design Variables

DV	Value	Description
1	167.31	Wing Root Chord ($ft.$)
2	103.52	L.E. Break, x ($ft.$)
3	32.06	L.E. Break, y ($ft.$)
4	138.09	T.E. Break, x ($ft.$)
5	31.15	T.E. Break, y ($ft.$)
6	122.45	L.E. Wing Tip, x ($ft.$)
7	10.55	Wing Tip Chord ($ft.$)
8	56.14	Wing Semi-Span ($ft.$)
9	0.4182	x-Loc. Airfoil Max. t/c (x/c)
10	2.8193	L.E. Radius Parameter
11	2.2646	t/c at Wing Root ($\%c$)
12	1.5632	t/c at L.E. Break ($\%c$)
13	1.5334	t/c at Wing Tip ($\%c$)
14	27.437	Fuselage X-Restraint #1
15	4.0653	Fuselage R-Restraint #1
16	129.866	Fuselage X-Restraint #2
17	5.0904	Fuselage R-Restraint #2
18	143.983	Fuselage X-Restraint #3
19	4.8947	Fuselage R-Restraint #3
20	244.050	Fuselage X-Restraint #4
21	5.0596	Fuselage R-Restraint #4

Table 4: Stress, Center of Pressure, and Bending Material Weight Comparisons

Load Case	$(\Delta\sigma)_{\max}$		$\Delta(\sigma_{\max})$		$\Delta y_{\text{c.p.}}$	$\frac{W_{\text{S/O-Euler}}}{W_{\text{S/O-LT}}}$
	psi	%	*psi*	%	*ft*	
M=2.4 n=1.0	-706	(25.2%)	-265	(5.0%)	-0.532	
M=1.2 n=1.0	-2049	(49.0%)	-1496	(15.5%)	-0.197	0.971
M=2.4 n=2.5	-2088	(55.4%)	-1043	(6.3%)	-0.811	

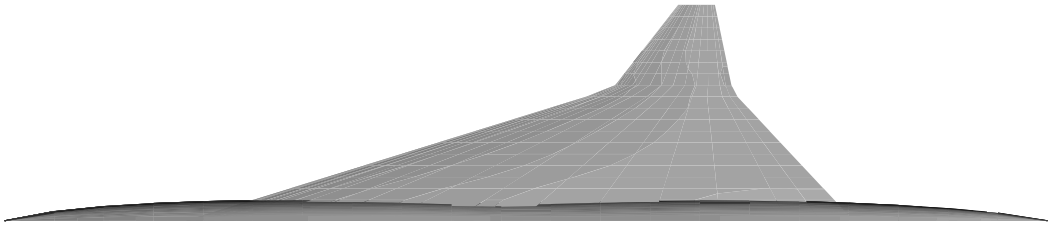

Figure 39: Design Case 2

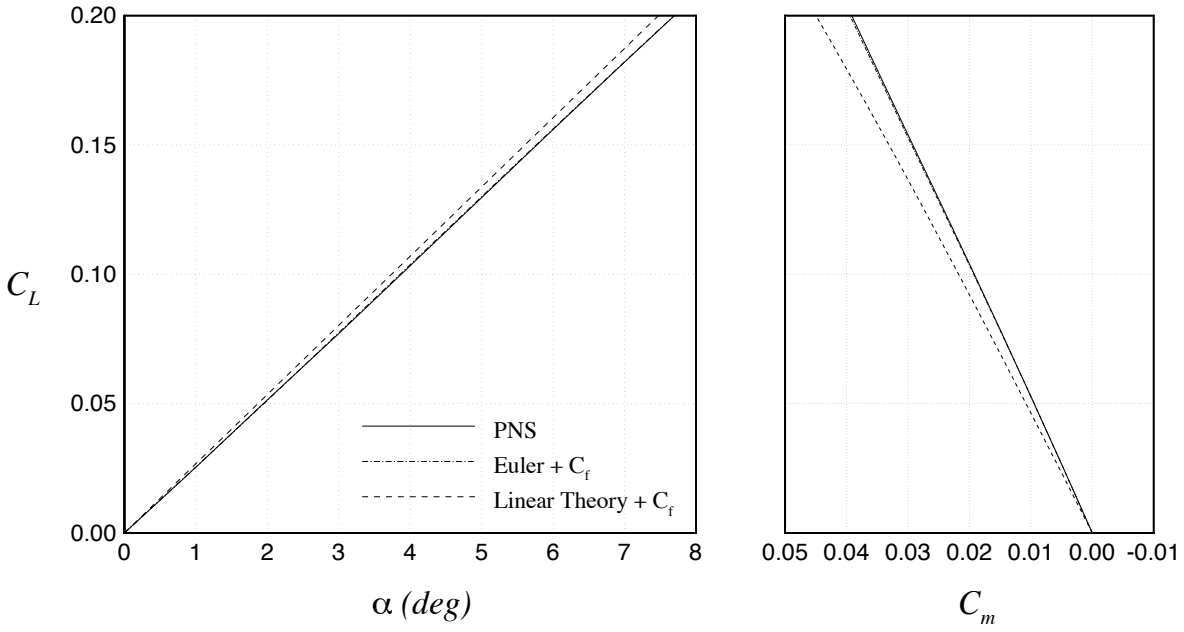

Figure 40: Lift and Pitching Moment Coefficients for Design Case 2 Uncambered Wing-Alone Configuration

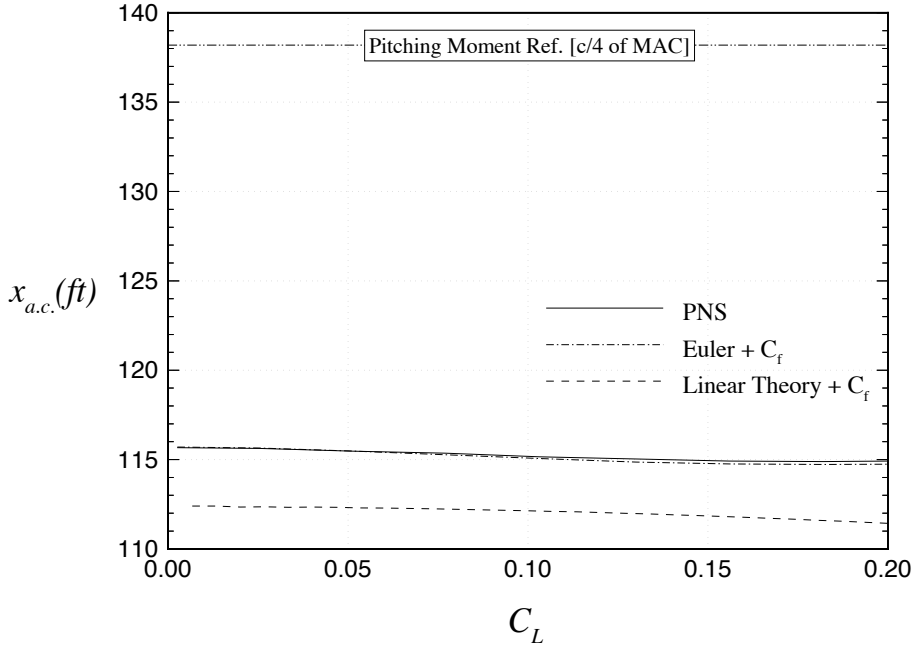

Figure 41: Change in Center of Pressure Location with Lift Coefficient

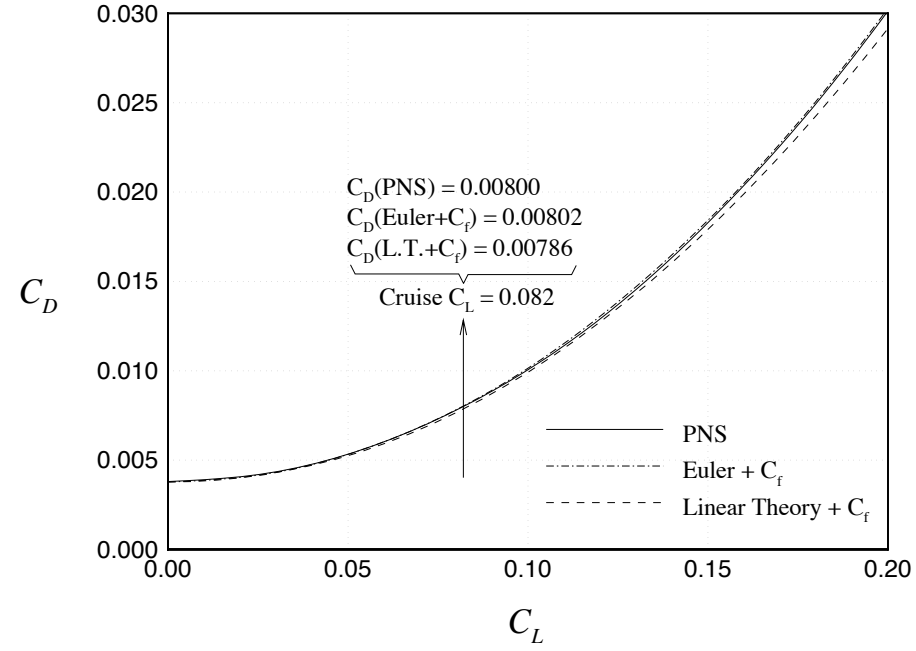

Figure 42: Drag Polar for Design Case 2 Uncambered Wing-Alone Configuration

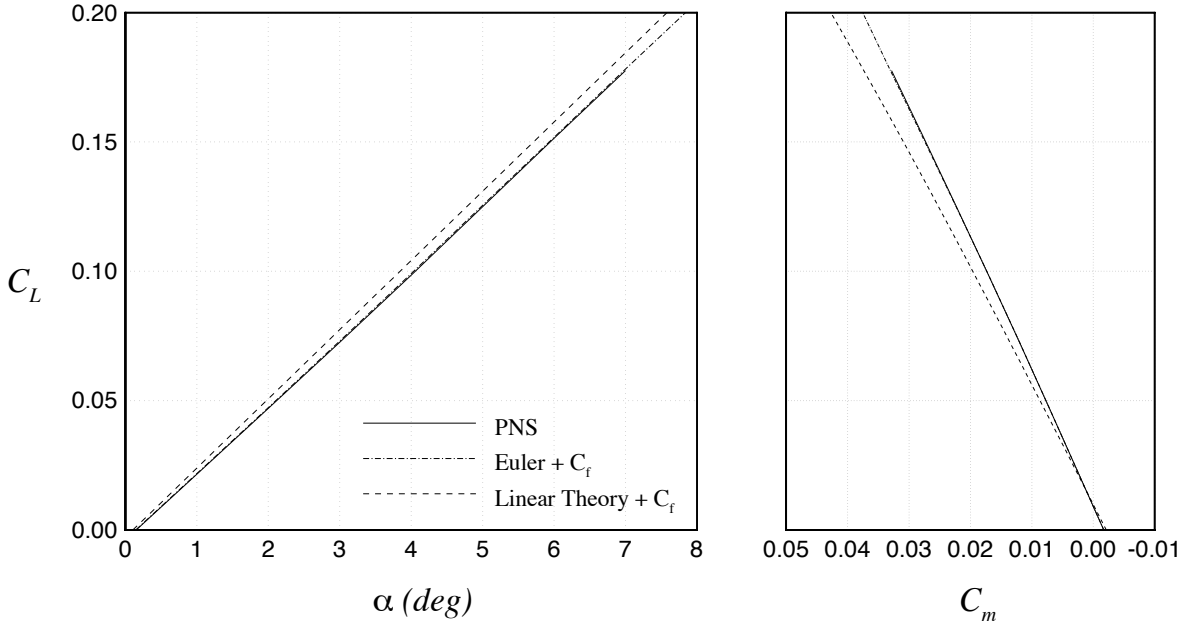

Figure 43: Lift and Pitching Moment Coefficients for Design Case 2 Cambered Wing-Alone Configuration

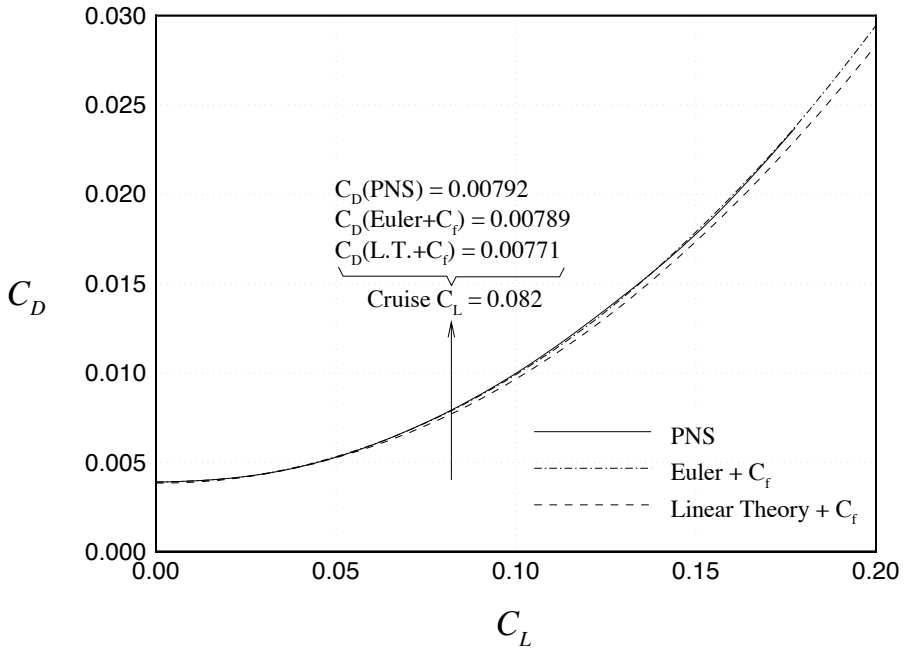

Figure 44: Drag Polar for Design Case 2 Cambered Wing-Alone Configuration

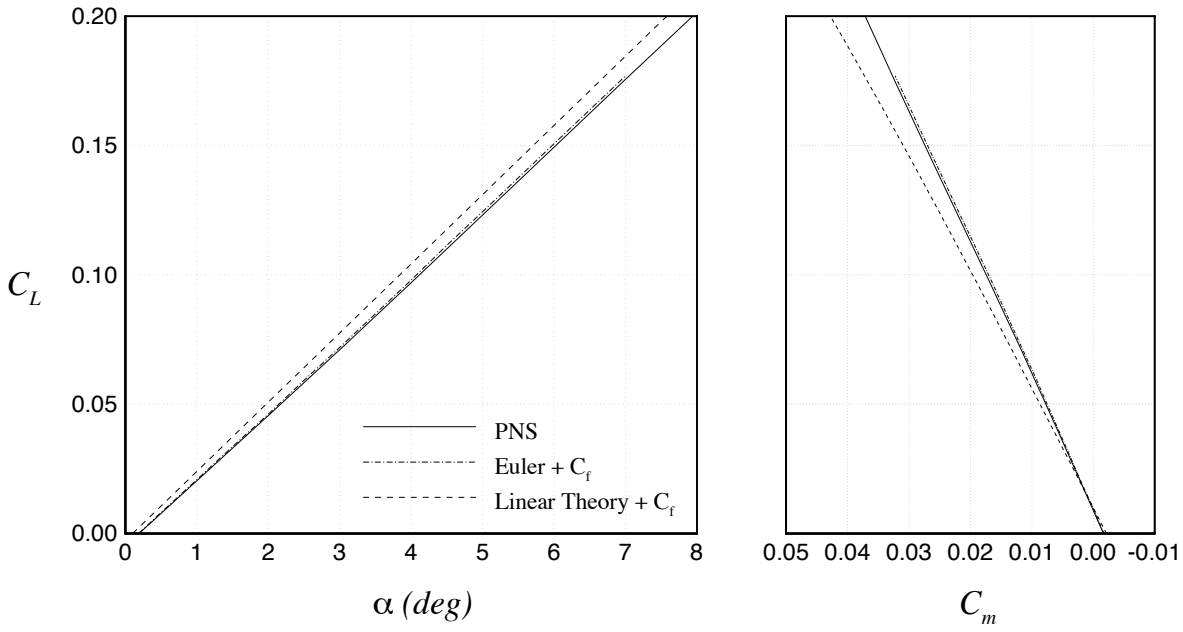

Figure 45: Lift and Pitching Moment Coefficients for Design Case 2 Wing-Fuselage Configuration

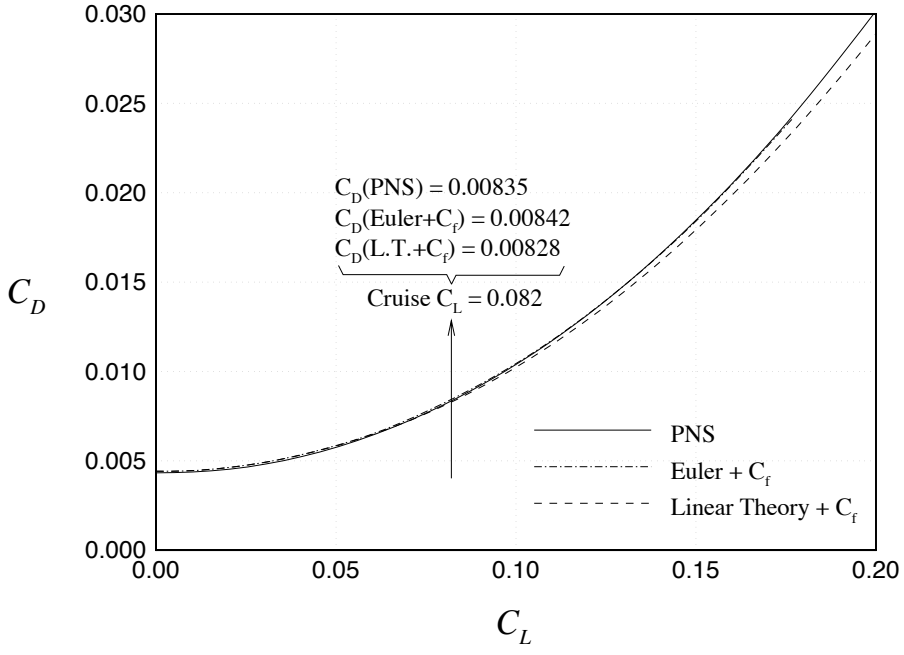

Figure 46: Drag Polar for Design Case 2 Wing-Fuselage Configuration

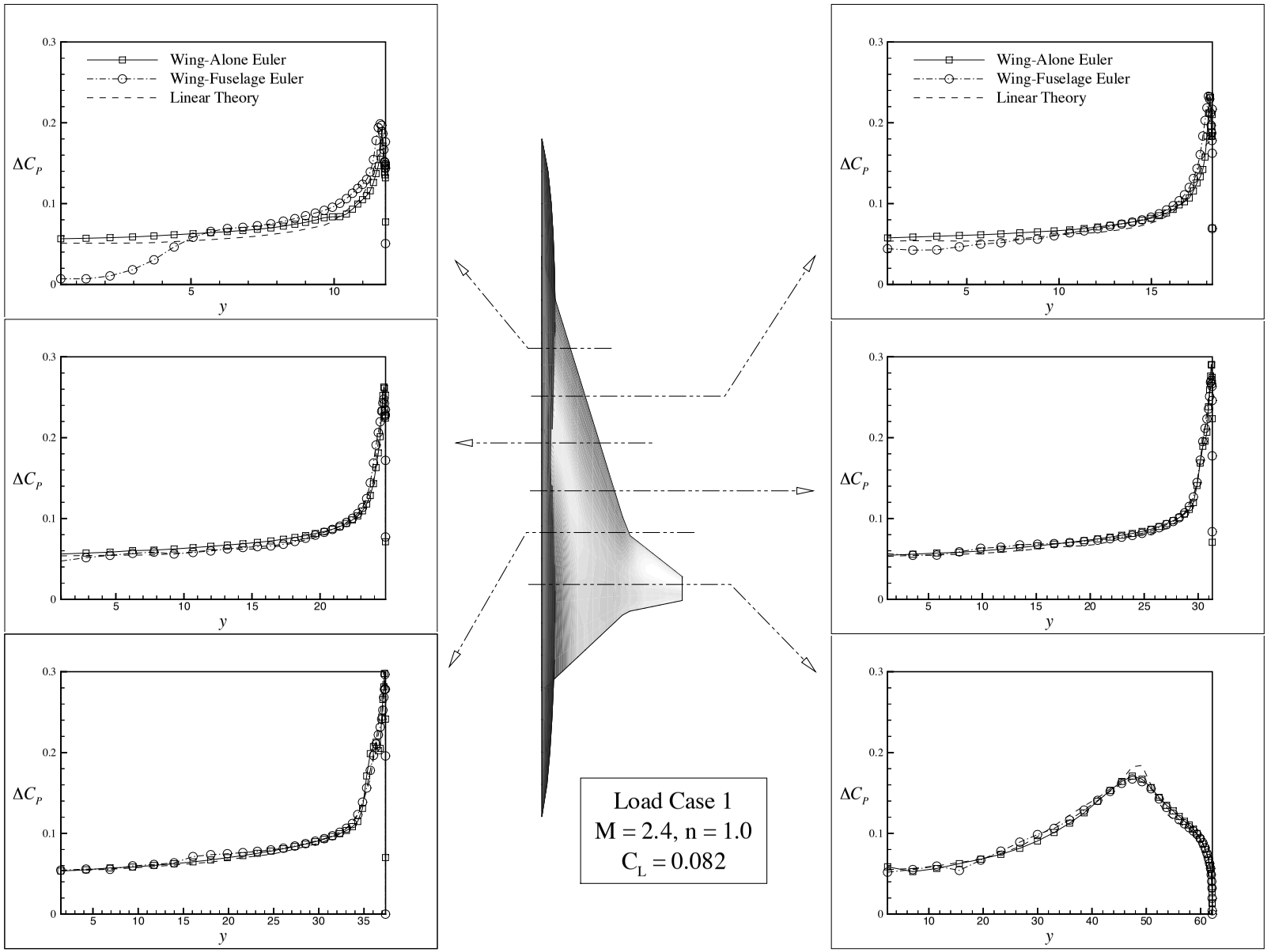

Figure 47: Aerodynamic Loads for Design Case 2 at Mach 2.4 Cruise

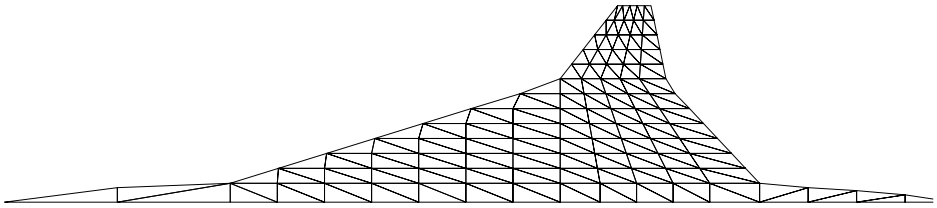

Figure 48: Structural Mesh for Design Case 2

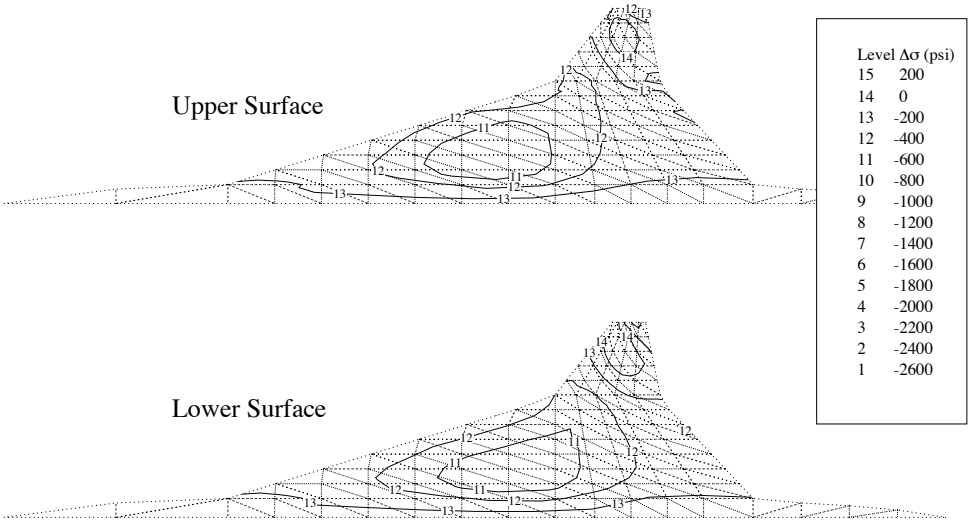

Figure 49: Stress Differences for Design Case 2 at Mach 2.4 Cruise

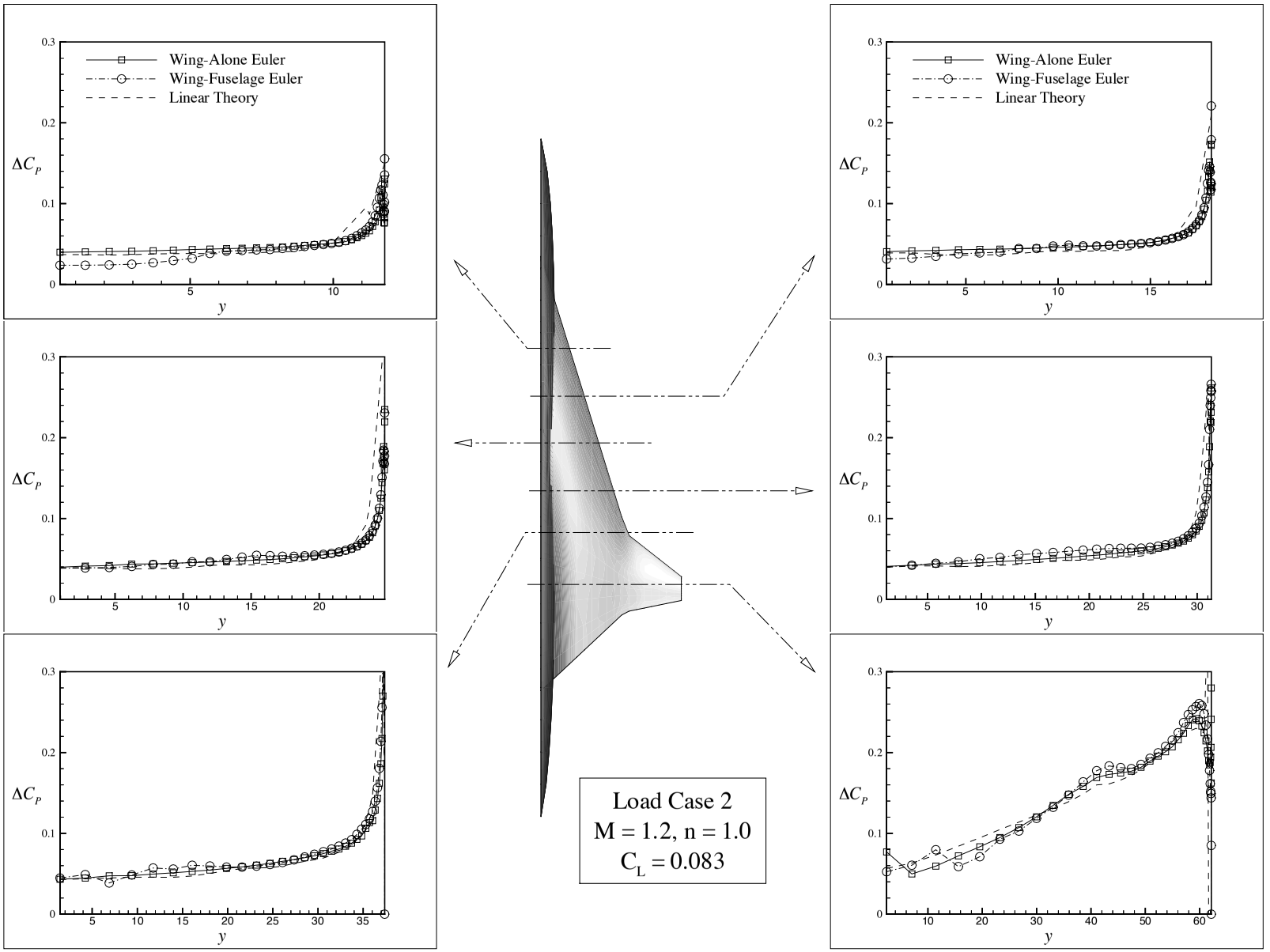

Figure 50: Aerodynamic Loads for Design Case 2 at Mach 1.2 Cruise

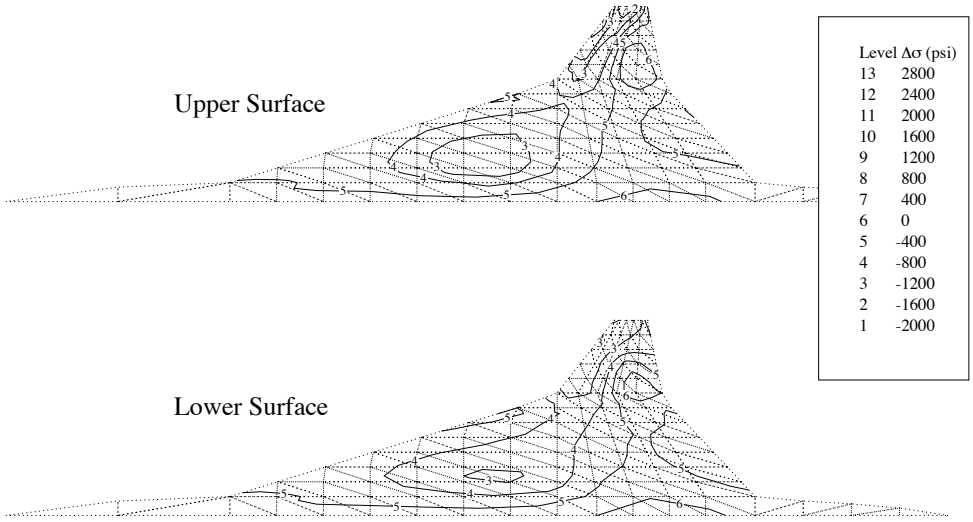

Figure 51: Stress Differences for Design Case 2 at Mach 1.2 Cruise

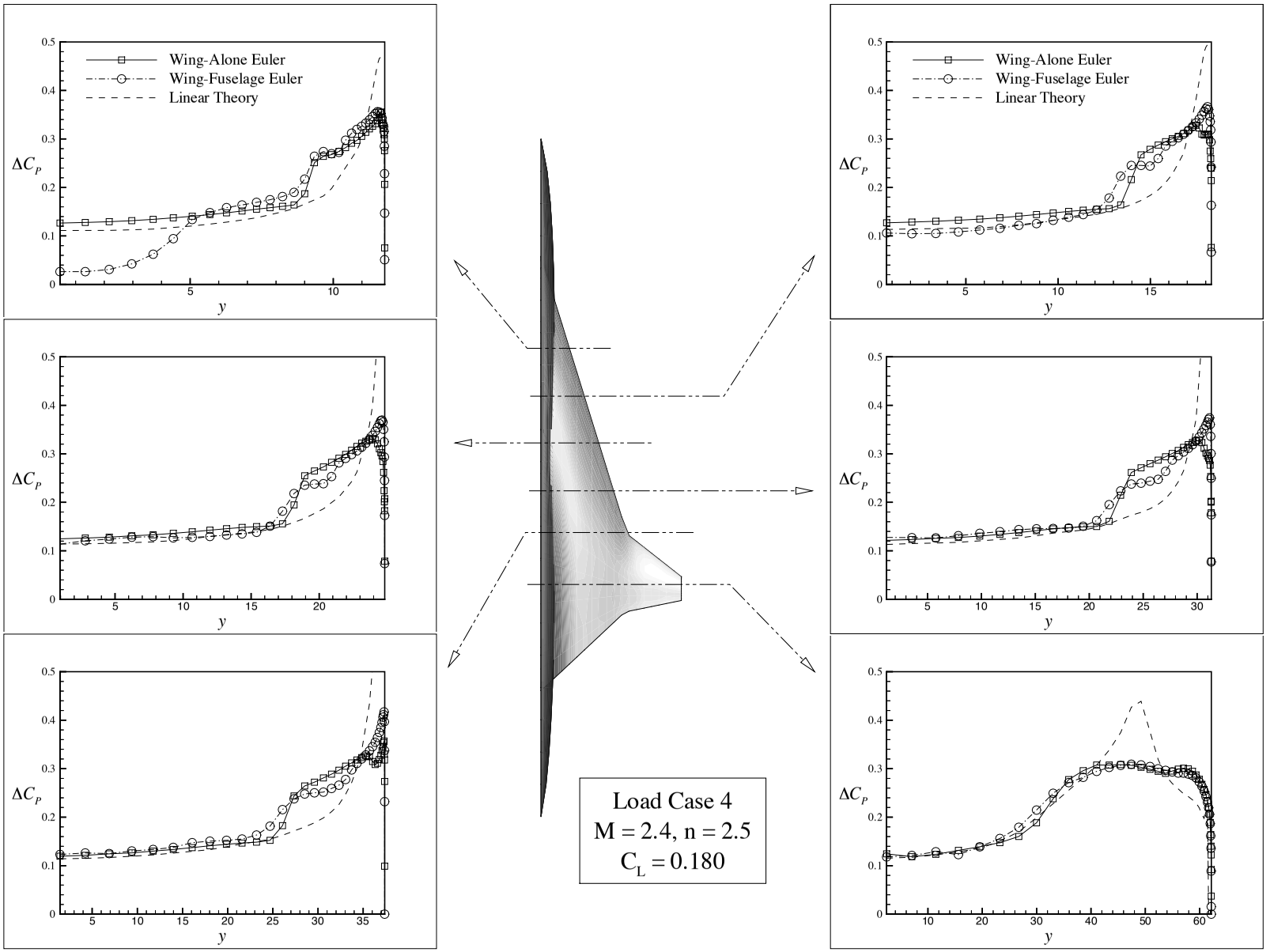

Figure 52: Aerodynamic Loads for Design Case 2 at Mach 2.4 2.5-g pull-up

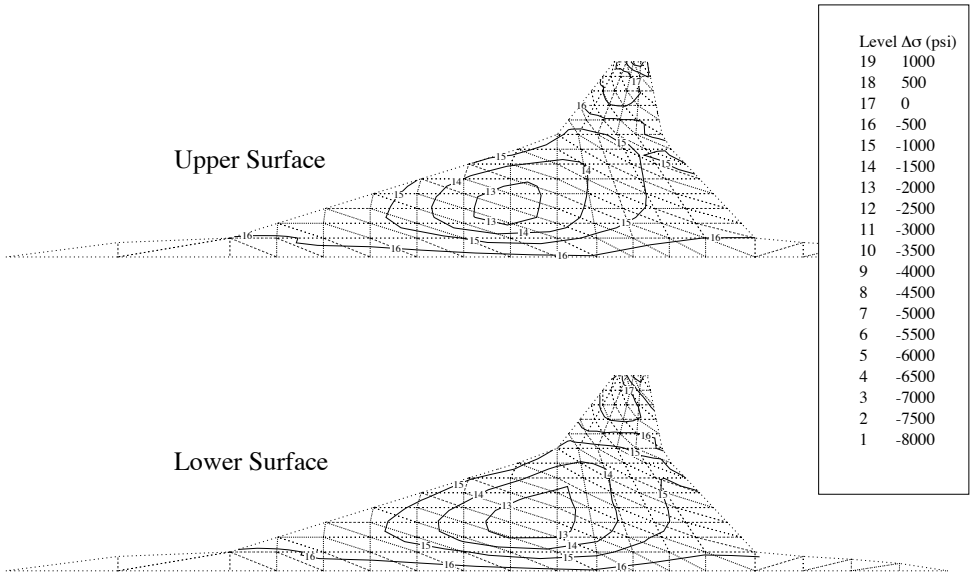

Figure 53: Stress Differences for Design Case 2 at Mach 2.4 2.5-g pull-up

3.3. Design Case 3

The third planform considered (Fig. 54) is a starting point design used in our optimization. This wing has a highly swept leading edge both inboard and outboard of the leading-edge break, and the wing trailing edge is aft-swept. The design variables used to create Design Case 3 are given in Table 5.

Uncambered Wing-Alone Design

The lift and pitching moment coefficient data for the Design Case 3 uncambered wing are plotted in Figure 55. These plots show many of the same trends in force predictions seen throughout this study. Linear theory overestimates the lift-curve slope and predicts a more positive C_m compared to CFD. The ratio of the quadratic to linear pitching moment terms from Eqn. 2 is 1.7 for this configuration. This ratio is lower than that for Design Case 1, and the curvature, while still apparent in the pitching moment plot, is correspondingly less. Figure 56 shows the movement in the aerodynamic center along with the location of the quarter-chord of the MAC. The aerodynamic center travels from 63.3% c_o at $C_L = 0.0$ to 61.2% c_o at $C_L = 0.2$. These locations are farther aft than those of Design Case 1 due to the aft-swept trailing edge. This trend and the nominal values of $x_{a.c.}$ are again in agreement with the diamond wing results presented in Ref. 36. As is true for the previous two designs, the aerodynamic center location from Euler and PNS calculations is farther aft than that from linear theory, resulting in a stronger nose-down tendency. The difference in $x_{a.c.}$ is 5.5 ft for this design.

The drag polar is given in Figure 57. For this design, cruise at Mach 2.4 is achieved with a lift coefficient of 0.077. PNS calculations give a cruise drag coefficient which is 1.0 count higher than that from linear theory. The skin friction estimate is only 0.4 counts larger than the PNS viscous drag. The wave drag computed from the Harris code is 0.7 count lower than that from PNS and 0.4 count lower than that from Euler. The errors in friction and wave drag cancel each other, giving a good value for the linear supersonic theory zero-lift drag. As with the other cases, the drag-due-to-lift error results in poor drag prediction at larger values of C_L.

Cambered Wing-Alone Design

Figures 58 and 59 show the lift curve and drag polar for the cambered wing. Cambering the wing resulted in a 2.9 count reduction in the cruise drag predicted from linear theory and a 2.4 count reduction in the cruise drag predicted from PNS. This is the largest drag reduction due to wing camber seen our studies.

The agreement between linear theory and CFD for the cambered wing is worse than it is for the uncambered wing. The friction drag estimate remains 0.6 counts higher than the PNS viscous drag prediction, but the total variation in the cruise drag for the cambered wing is 1.5 counts. Analysis shows that the sensitivity of the range to changes in the drag for this design is 61.5 *n.mi.*/count. This means that the range computed from linear supersonic theory is 92 *n.mi.* greater than if we used PNS aerodynamics. Again, we see that seemingly small differences in the drag coefficient result in large variations in the predicted range.

Wing-Fuselage Design

The wing-fuselage lift, moment, and drag coefficient data are plotted in Figures 60 and 61. The linear theory cruise drag is 0.7 counts lower than the PNS cruise drag. The skin friction estimate is 0.4 counts higher than the PNS prediction for the viscous drag. For all three designs studied, the skin friction estimate overpredicts the viscous drag, but the errors have been within one count.

Loads and Structural Optimization

The loads for the wing-alone and wing-fuselage configurations at Mach 2.4 cruise (Fig. 62) show good agreement much like the previous two designs. The structural model used for the finite-element analysis is shown in Figure 63. The stress distributions for this load case (Fig. 64) indicate that the largest difference in predicted stresses occurs near the middle of the wing. In addition, this difference is negative meaning that the stresses from Euler loads are lower than those from linear theory loads. This is in agreement with the results from the previous two designs. The magnitude of the differences in stress and spanwise center of pressure location (Table 6) are larger than those of Design Cases 1 and 2. The maximum difference in predicted stresses -2764 *psi* (23.4%), and the percent difference in maximum stress is 18.9%. As seen in the previous wings, the wing bending stresses are very sensitive to small variations in the wing loading.

The Mach 1.2 cruise loads show good agreement over most of the wing. There is some variation in loads aft of the leading-edge break. The wing-fuselage configuration shows the largest differences at the last wing cut. The stresses (Fig. 66) from the Euler loads are lower than those from linear theory loads over the middle of the inboard wing section. However, there is a large region where the Euler stresses are larger. In fact, as seen in Table 6, the maximum difference between the stresses from Euler and linear theory loads is +4600 *psi* (21.2%). The maximum stress from Euler loads is also 12.7% larger than that from linear theory loads. While, the Design Case 2 stresses for this load case did show a fairly large region of positive stress difference, this is the first case seen where the maximum difference in stresses and difference in maximum stress are positive.

The 2.5-g pull-up at Mach 2.4 (Fig. 67) again gives the largest disagreement in loads. Linear theory fails to properly predict the loads outboard of the crossflow shock. The stress differences (Fig. 68) for this case are also large. The maximum difference in stress is -8745 *psi*, which is 22.8% of the stress value at that element. The difference in maximum stress is 21.1%. As is the case for Design Cases 1 and 2, the maximum stress on the wing occurs near the leading edge break. The stresses from the Euler loads are lower over the majority of the wing. This stress disagreement is larger than in the other load cases, as is the error in the predicted spanwise location of the center of pressure.

The structural optimization shows the effects of the larger Euler stresses in the Mach 1.2 cruise condition. In contrast to the previous two designs, structural optimization produced a heavier wing when using the Euler loads than when using linear theory loads. The ratio of wing bending material weights is 1.051. This amounts to only a 1761 *lb* difference in weight. For all designs studied, we have seen that significant differences in the wing bending stresses do not translate into large differences in wing weight from structural optimization. It appears that while significant gains can be achieved using CFD for the HSCT performance predictions, linear theory loads may be adequate for use in our HSCT wing bending material weight calculations.

Table 5: Design Case 3 Design Variables

DV	Value	Description
1	169.47	Wing Root Chord ($ft.$)
2	143.34	L.E. Break, x ($ft.$)
3	37.73	L.E. Break, y ($ft.$)
4	176.05	T.E. Break, x ($ft.$)
5	30.39	T.E. Break, y ($ft.$)
6	189.83	L.E. Wing Tip, x ($ft.$)
7	7.02	Wing Tip Chord ($ft.$)
8	74.33	Wing Semi-Span ($ft.$)
9	0.4800	x-Loc. Airfoil Max. t/c (x/c)
10	3.2000	L.E. Radius Parameter
11	2.1400	t/c at Wing Root ($\%c$)
12	1.7300	t/c at L.E. Break ($\%c$)
13	1.5100	t/c at Wing Tip ($\%c$)
14	70.000	Fuselage X-Restraint #1
15	6.0000	Fuselage R-Restraint #1
16	135.000	Fuselage X-Restraint #2
17	5.8000	Fuselage R-Restraint #2
18	170.000	Fuselage X-Restraint #3
19	5.8000	Fuselage R-Restraint #3
20	215.000	Fuselage X-Restraint #4
21	6.0000	Fuselage R-Restraint #4

Table 6: Stress, Center of Pressure, and Bending Material Weight Comparisons

Load Case	$(\Delta\sigma)_{\max}$		$\Delta(\sigma_{\max})$		$\Delta y_{\text{c.p.}}$	$\frac{W_{\text{S/O-Euler}}}{W_{\text{S/O-LT}}}$
	psi	%	*psi*	%	*ft*	
M=2.4 n=1.0	-2764	(23.4%)	-2520	(18.9%)	-1.713	
M=1.2 n=1.0	+4601	(21.2%)	+4594	(12.7%)	-0.056	1.051
M=2.4 n=2.5	-8745	(22.8%)	-8543	(21.1%)	-1.952	

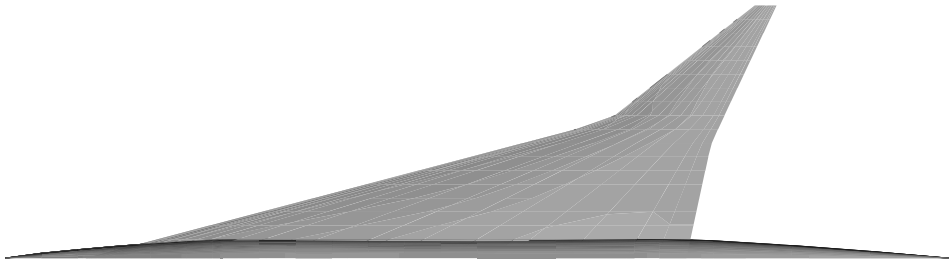

Figure 54: Design Case 3

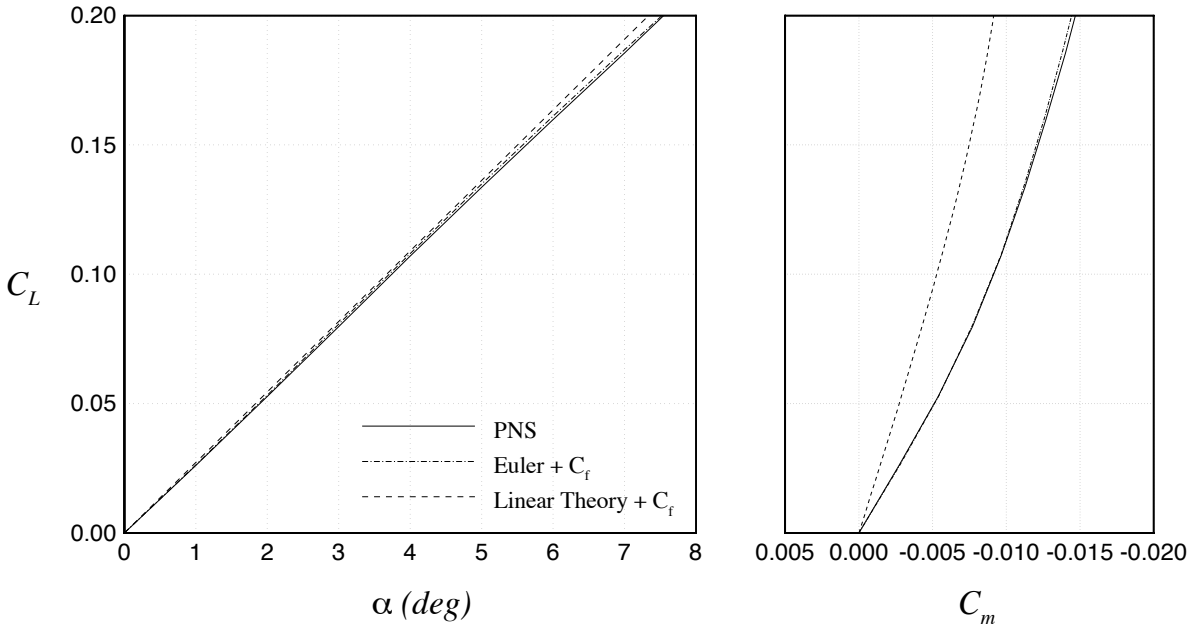

Figure 55: Lift and Pitching Moment Coefficients for Design Case 3 Uncambered Wing-Alone Configuration

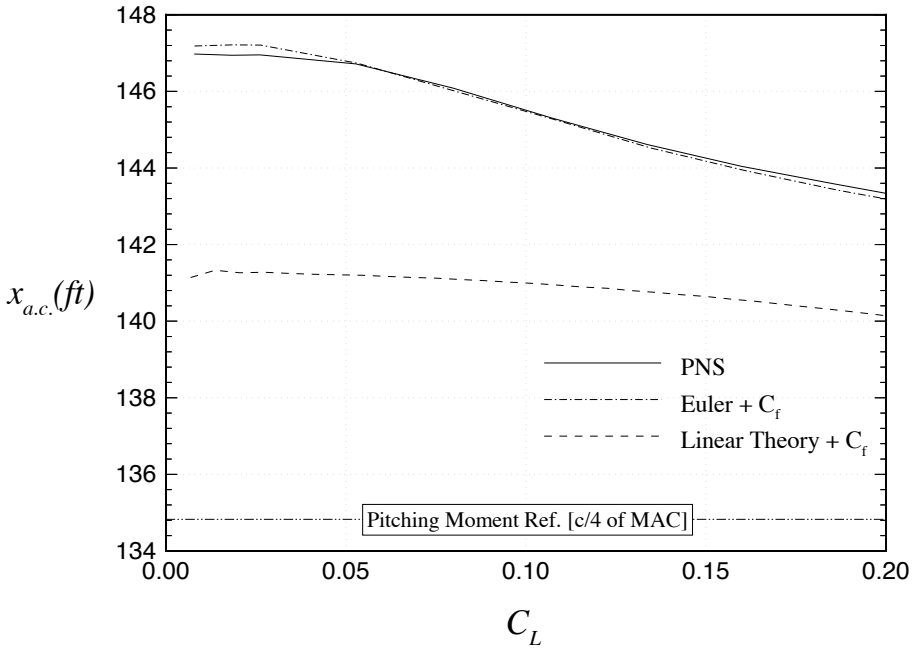

Figure 56: Change in Center of Pressure Location with Lift Coefficient

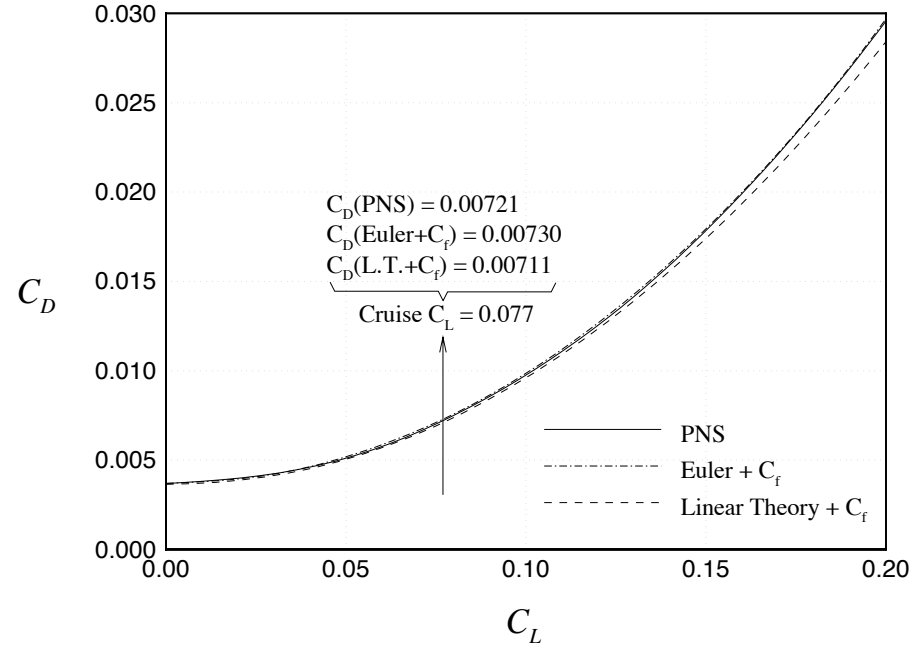

Figure 57: Drag Polar for Design Case 3 Uncambered Wing-Alone Configuration

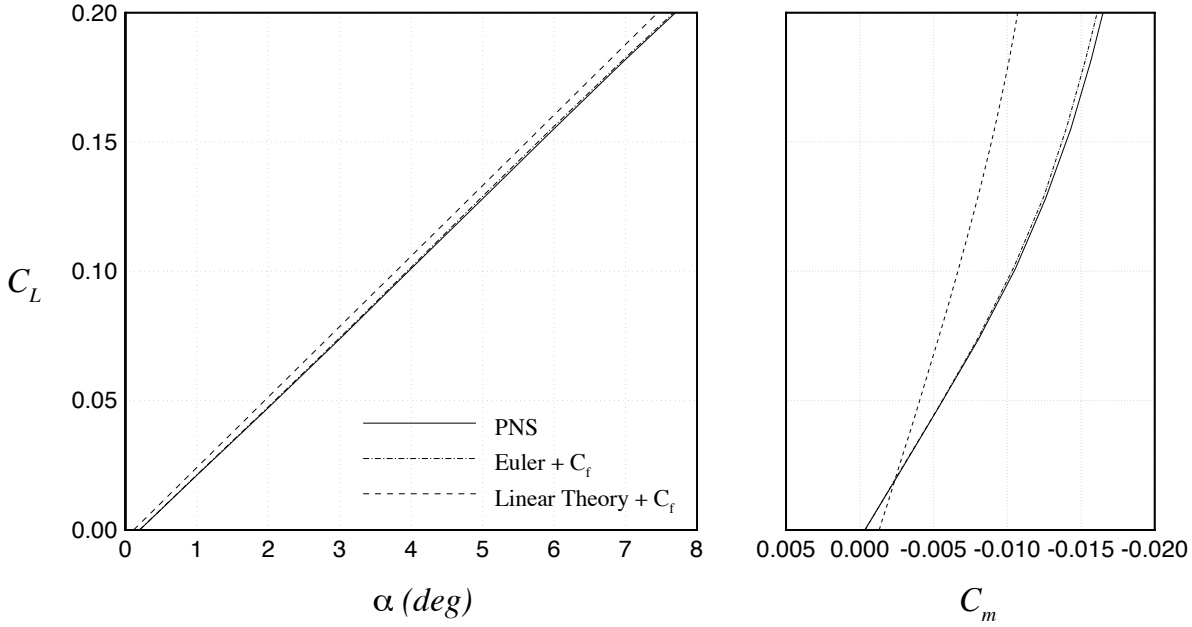

Figure 58: Lift and Pitching Moment Coefficients for Design Case 3 Cambered Wing-Alone Configuration

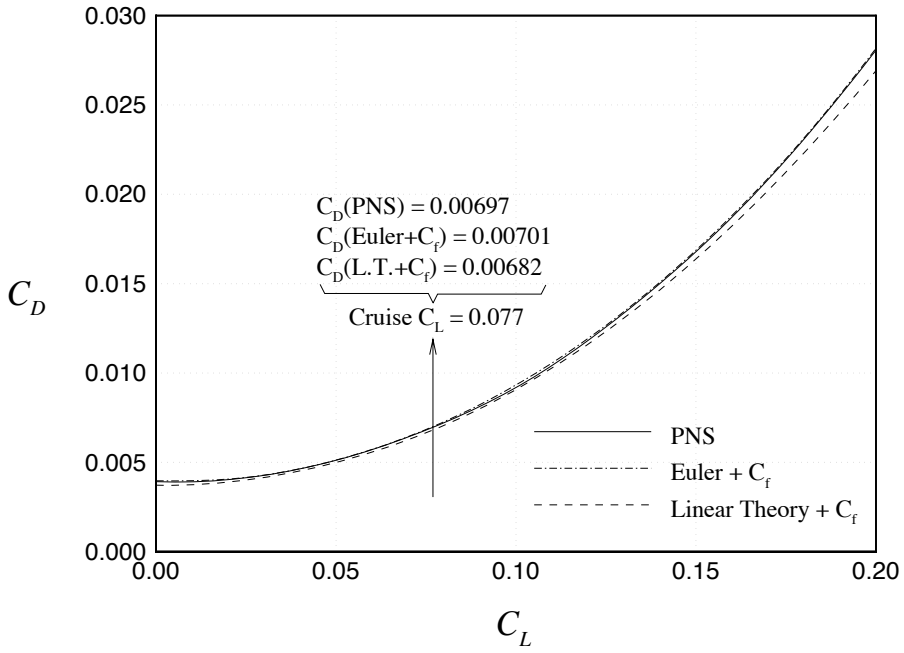

Figure 59: Drag Polar for Design Case 3 Cambered Wing-Alone Configuration

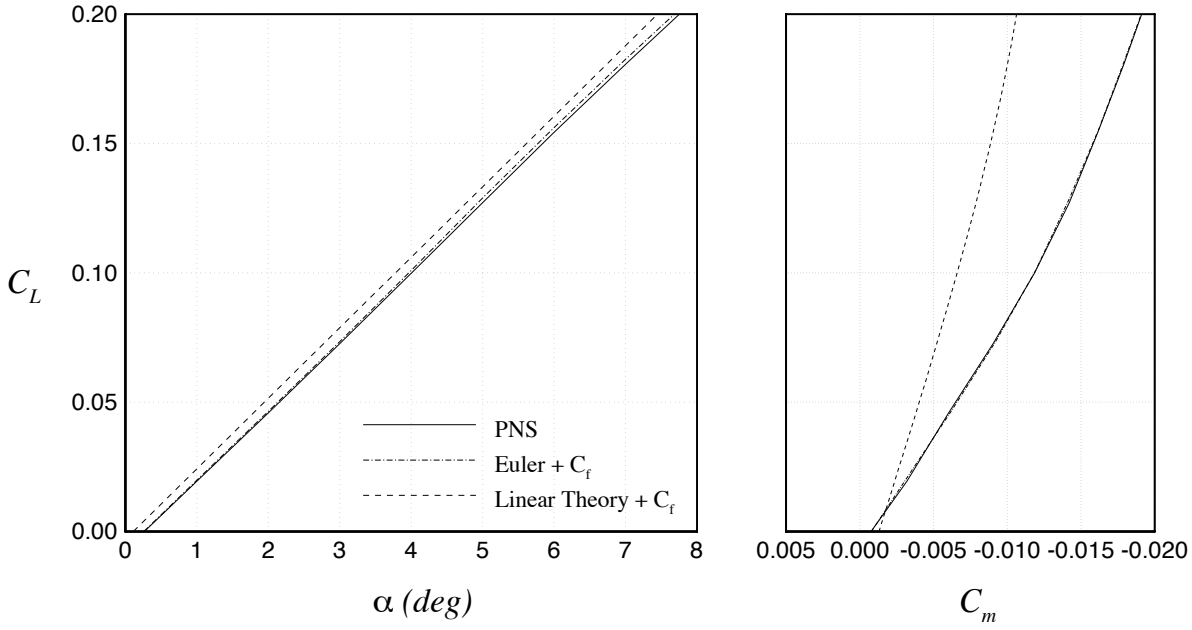

Figure 60: Lift and Pitching Moment Coefficients for Design Case 3 Wing-Fuselage Configuration

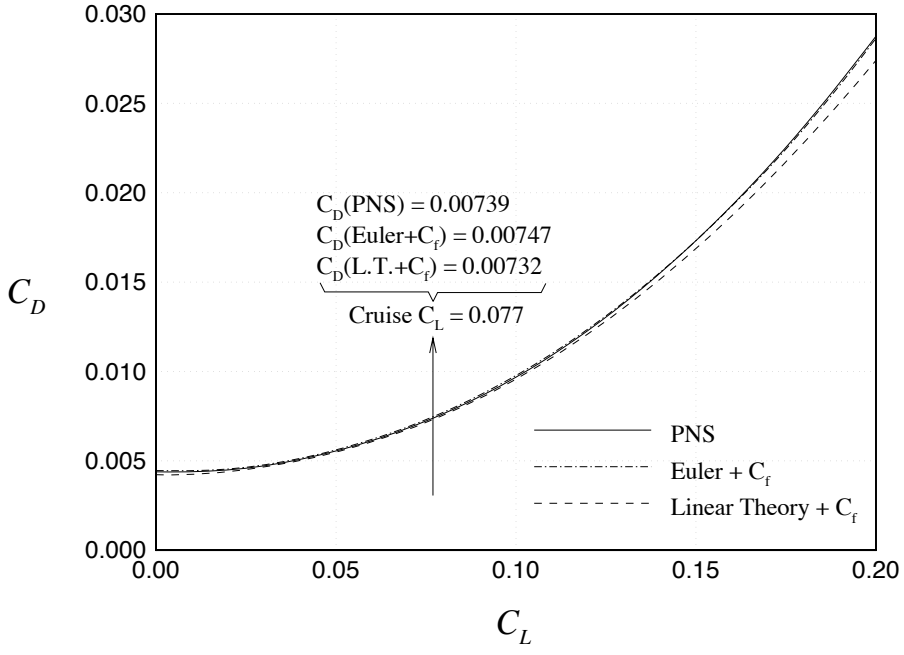

Figure 61: Drag Polar for Design Case 3 Wing-Fuselage Configuration

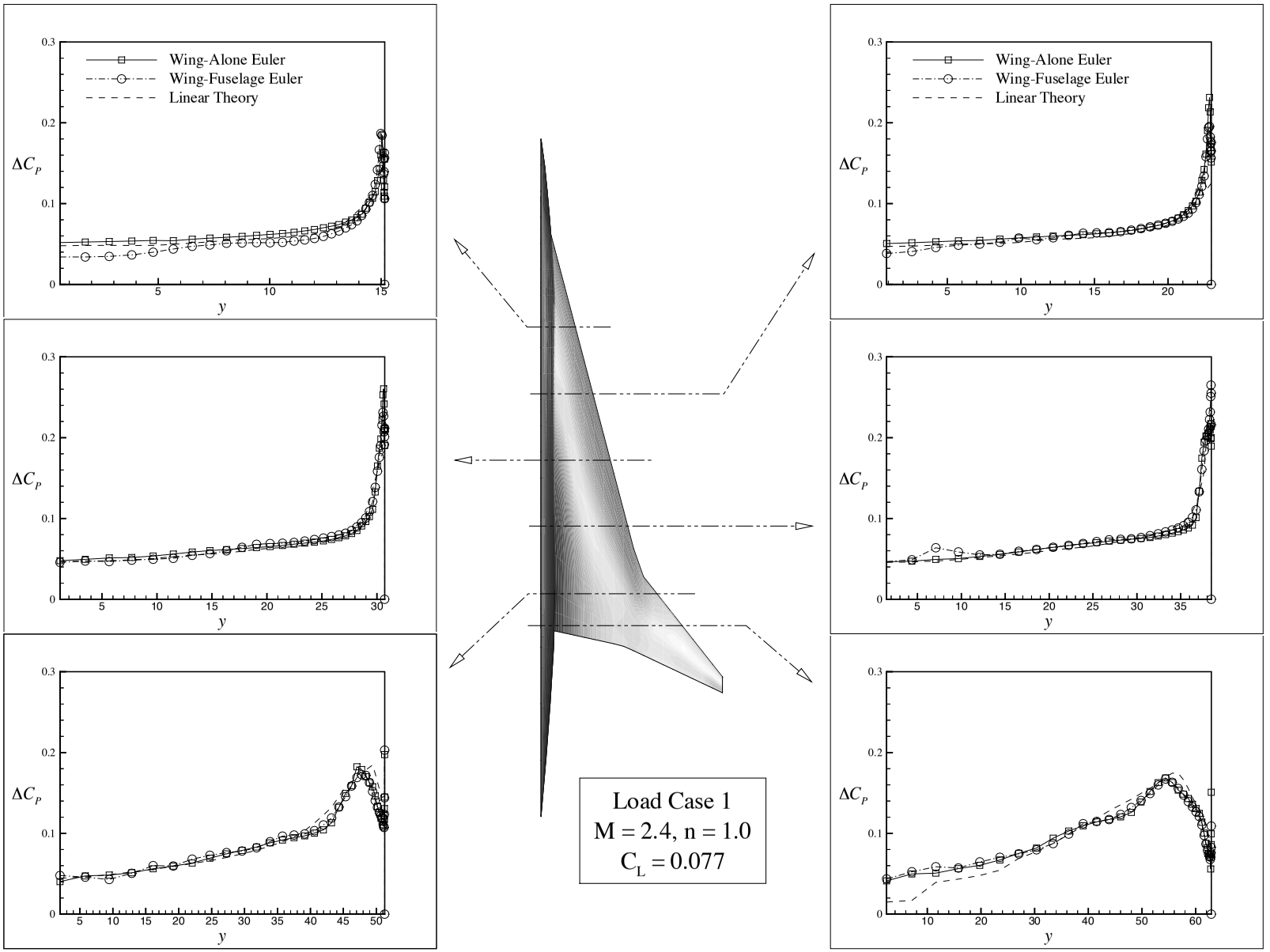

Figure 62: Aerodynamic Loads for Design Case 3 at Mach 2.4 Cruise

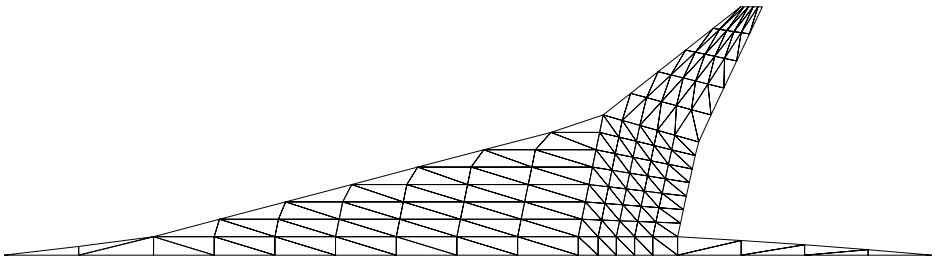

Figure 63: Structural Mesh for Design Case 3

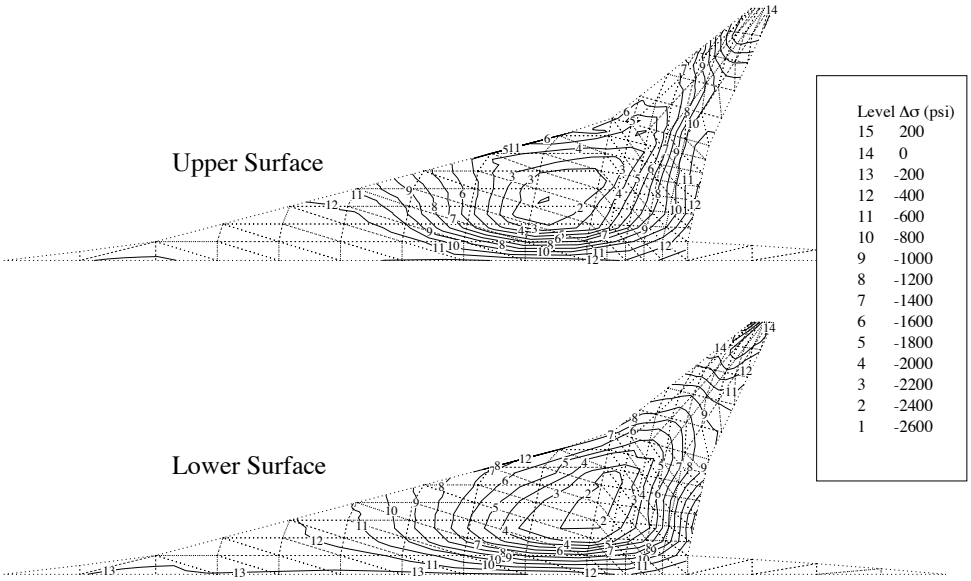

Figure 64: Stress Differences for Design Case 3 at Mach 2.4 Cruise

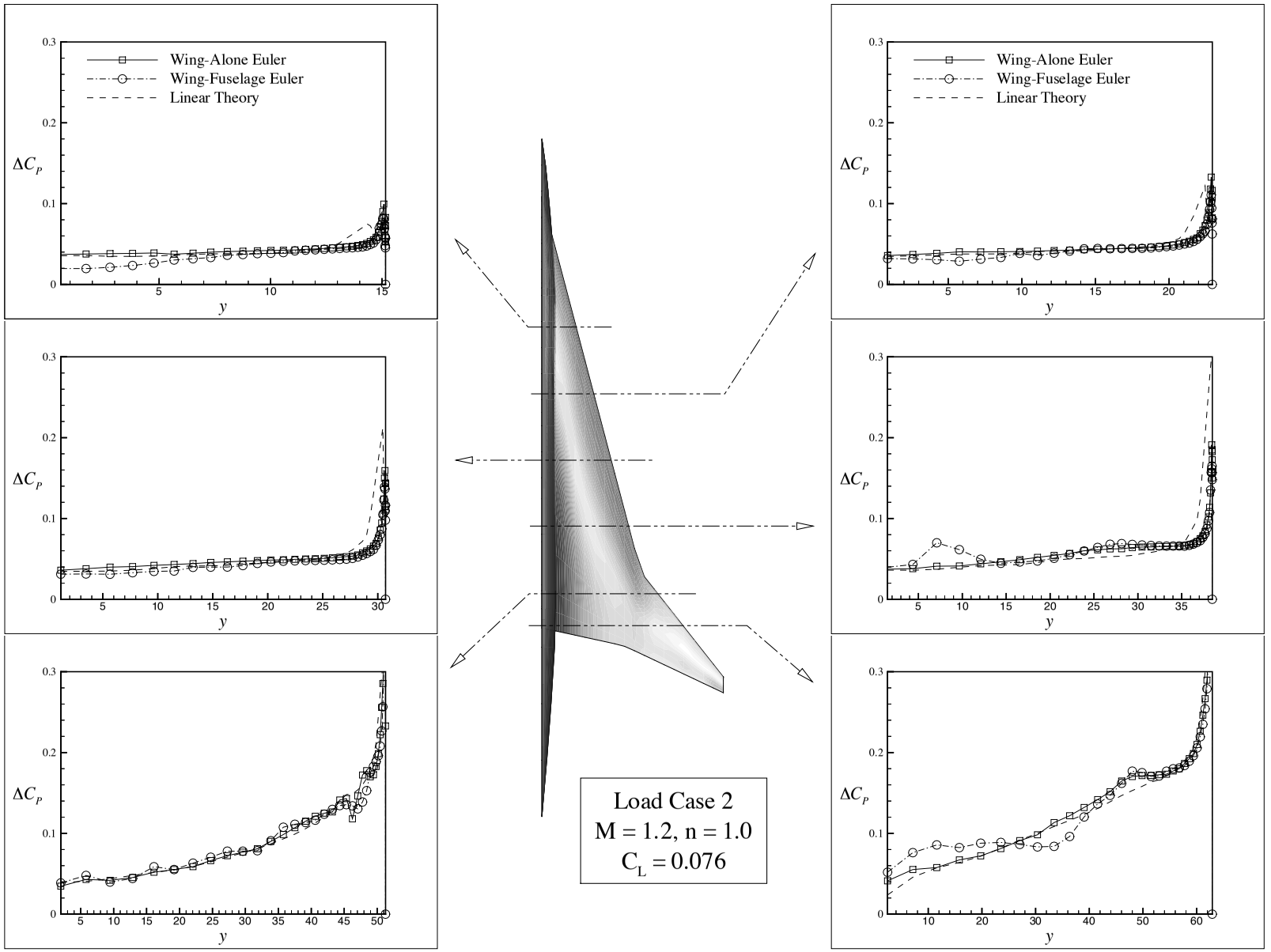

Figure 65: Aerodynamic Loads for Design Case 3 at Mach 1.2 Cruise

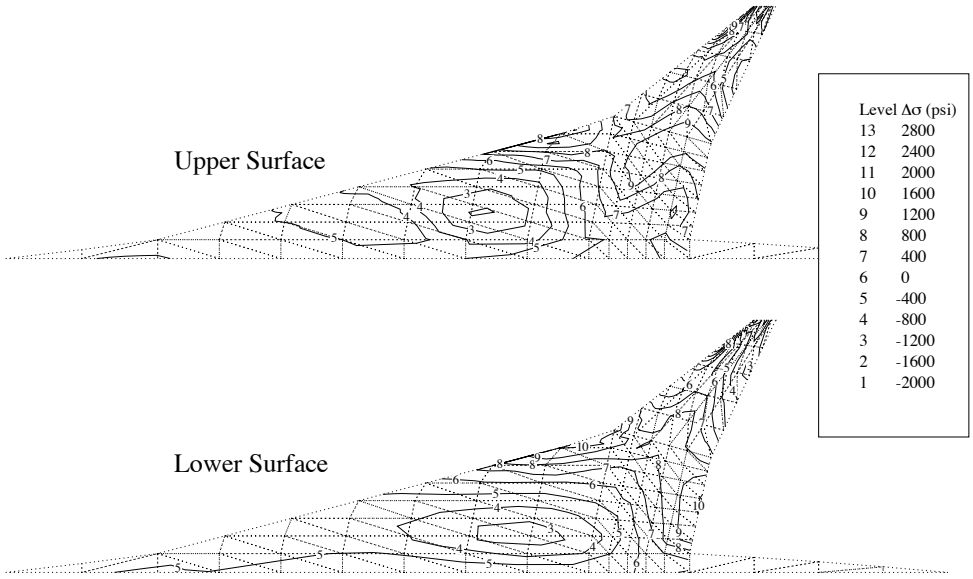

Figure 66: Stress Differences for Design Case 3 at Mach 1.2 Cruise

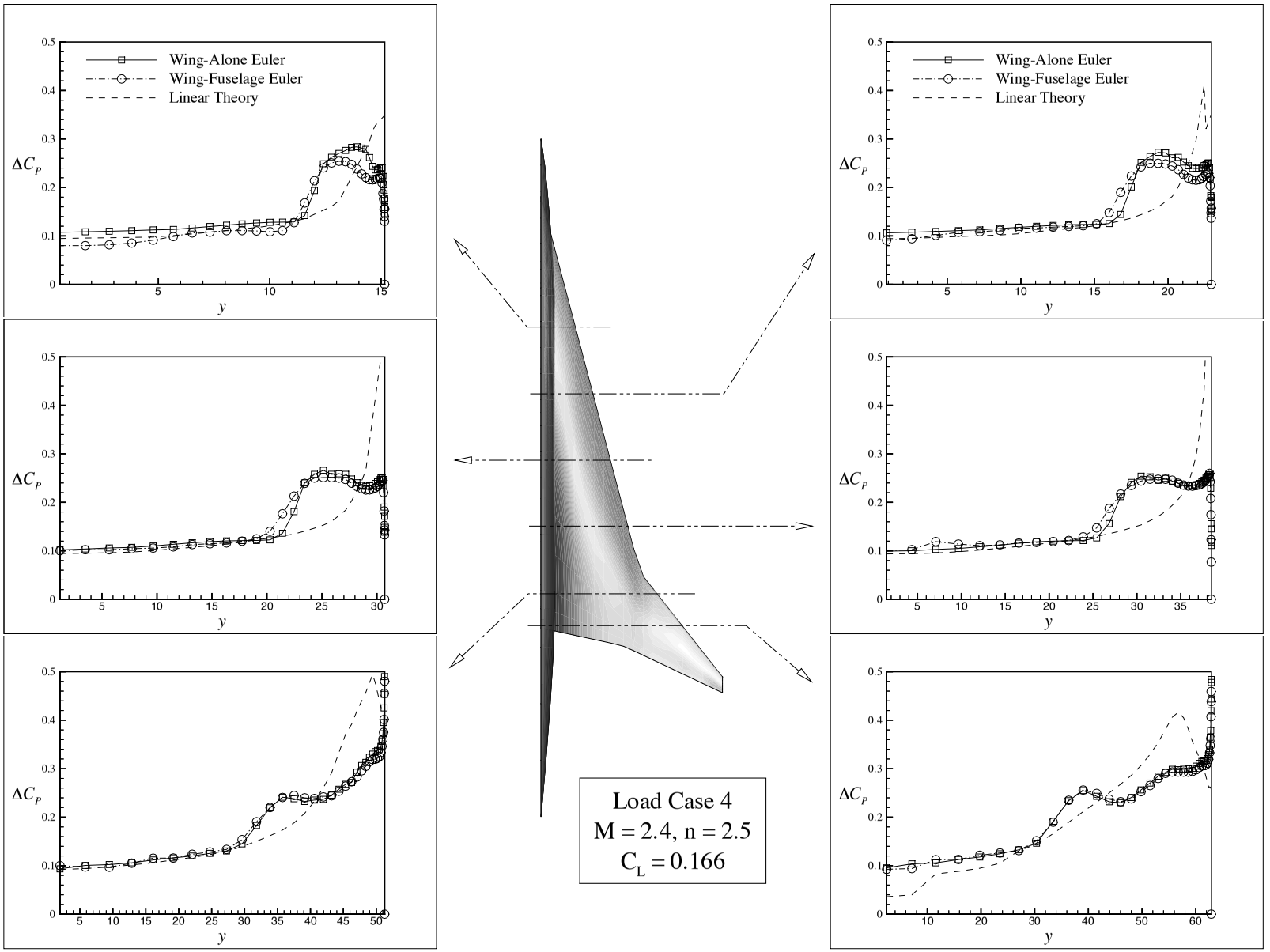

Figure 67: Aerodynamic Loads for Design Case 3 at Mach 2.4 2.5-g pull-up

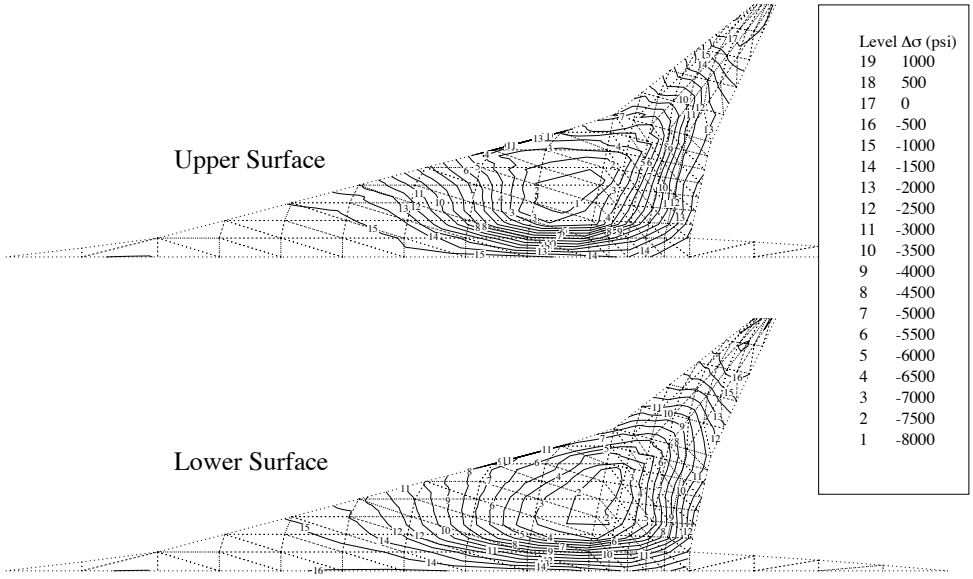

Figure 68: Stress Differences for Design Case 3 at Mach 2.4 2.5-g pull-up

3.4. Effects of Drag Differences on Design Optimization

As the previous sections have shown, small differences in the predicted drag coefficient result in large changes in the aircraft performance. We now discuss how changes in the drag effect the HSCT design optimization results. For the designs presented, we have seen errors in the linear supersonic theory cruise drag of up to 2.1 counts. In this study, up to 2 counts of drag are added to and subtracted from the viscous drag prediction, allowing the drag coefficient to be altered over the entire flight profile. The optimization procedure is then run with the altered drag values.

The plot of the change in the optimized take-off gross weight (TOGW) with the change in drag coefficient is given in Figure 69. The variation in certain components of the weight due to the changes in the drag are presented in Table 7. The TOGW of the optimal design increases by 56,118 *lbs* with the addition of the 2 counts of drag. Out of the total increase in weight, 37,218 *lbs* (66.3%) is from added fuel weight, 8625 *lbs* (15.4%) is from the propulsion system, 5967 *lbs* (10.6%) is from the wing weight, and the remaining 4308 *lbs* (7.7%) comes from the tails, fuselage, and other components. The main effect of increasing the drag is to cause the optimizer to increase the amount of fuel and size of the engines in order to meet the range constraint. Geometrically, adding 2 counts of drag causes the optimizer to increase the outboard wing sweep (Fig. 70) to improve the supersonic performance and offset the increased drag. Clearly, small errors in drag predictions also have a large influence on the optimized aircraft. Further details about the sensitivity of the design optimization to changes in the drag can be found in Ref. 38.

Table 7: Variation in Weight Due to Changes in the Drag

	Change in Drag Coefficient				
	-2 Counts	-1 Count	Baseline	+1 Count	+2 Counts
Gross Weight (*lbs*)	754,560	767,907	772,907	807,774	829,099
Fuel Weight (*lbs*)	391,817	401,316	403,346	426,628	440,564
Wing Weight (*lbs*)	107,071	107,364	113,086	115,077	119,053
Vertical Tail Weight (*lbs*)	1851	1877	1898	2014	2039
Horizontal Tail Weight (*lbs*)	8986	9208	8346	9617	10,946
Propulsion System Weight (*lbs*)	81,992	84,989	82,791	89,873	91,416

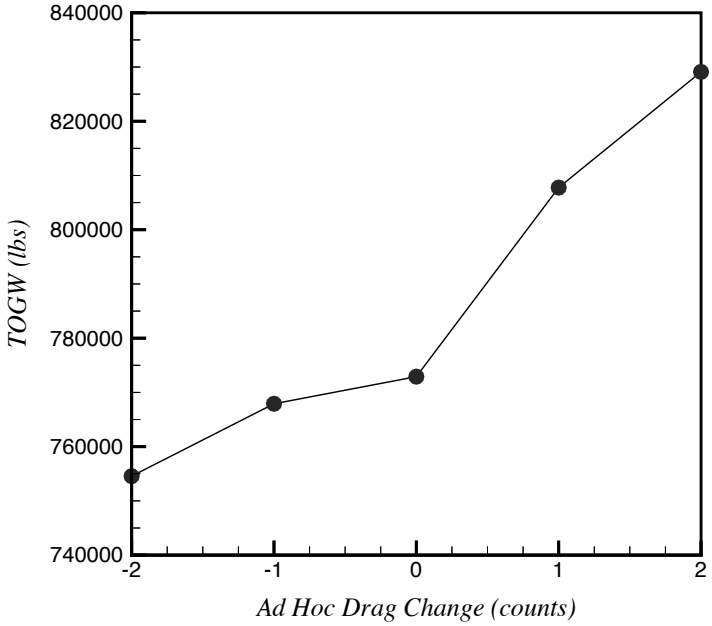

Figure 69: TOGW Variation with Drag Change

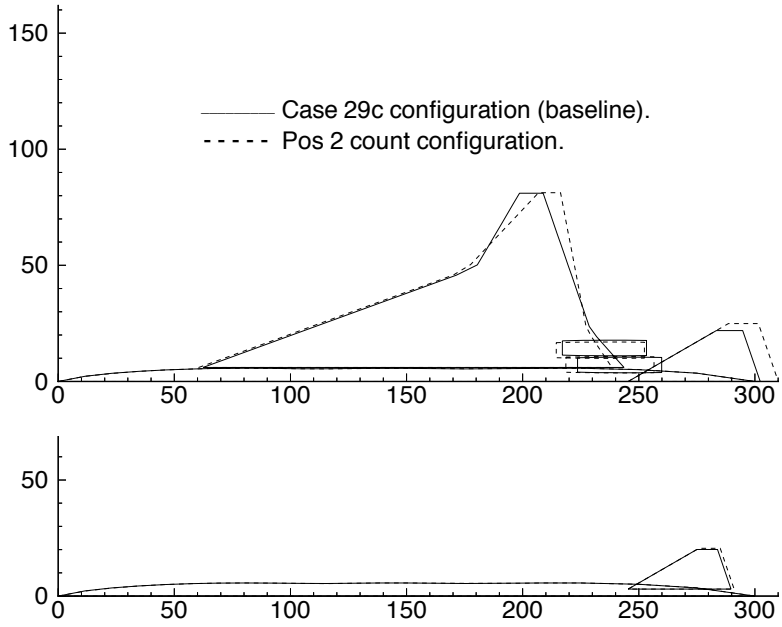

Figure 70: Changes in Optimal Design due to Increase in Drag

4. Summary of Results

Euler and PNS solutions for the supersonic performance and loads of HSCT wing and wing-fuselage designs are compared with those from linear theory. Grid convergence studies showed that, for wing-alone configurations, a 77×51×77 grid is sufficient to resolve the drag within 1/2 counts of the solution extrapolated to zero mesh size. The same resolution was obtained using a 77×91×77 grid for PNS calculations. Reducing the residual 2 orders of magnitude is required for converged solutions in the supersonic flow conditions considered. The computational costs of the wing-alone Euler and PNS calculations are 18 minutes and 2.5 hours, respectively, on an SGI Power Challenge R8000 machine.

The configurations examined show linear theory consistently overpredicting the lift. Linear theory pitching moments for the HSCT designs considered show a stronger nose-up tendency than those from CFD because the aerodynamic center is located farther forward. Studies of other configurations have indicated the opposite trend.[9, 10] Curvature in the pitching moment results occur due to forward movement of the aerodynamic center location with increasing lift. While this movement is small (0.5%–1.5% of the root chord, c_o), it is significant when the moment reference point is near the aerodynamic center. Analysis of the three designs shows that the nominal aerodynamic center location moves aft (Fig. 71) as the trailing edge of the wing becomes more aft-swept. This agrees with studies presented in Ref. 36.

For the uncambered wing-alone configurations, the difference in the Harris code and CFD predictions for the zero-lift wave drag range from -1.4 counts to +0.7 counts. (Negative values indicating that CFD results are lower.) The skin friction estimates are as much as 0.9 counts higher than the PNS values. Linear theory is found to underpredict the induced drag for these configurations. When the linear theory zero-lift drag is larger than that from CFD, these errors then to cancel each other at cruise. However, when the linear theory zero-lift drag is lower, the errors add. The largest discrepancy in the linear theory and PNS cruise drag for the uncambered wings is 1.4 counts.

Using WINGDES to find the optimal camber distribution results in a reduction of the cruise drag by up to 2.9 counts from the original uncambered wing using linear theory analysis. PNS predictions are not quite as optimistic. The best reduction in cruise drag through cambering is 2.4 counts when using PNS results. The algebraic skin friction estimates are again larger than the PNS viscous drag values, but they are within 1.0 count. The differences in cruise drag coefficient range from +0.3 to +2.1 counts. The 0.3 count difference occurs when the linear theory zero-lift drag and induced drag errors cancel, and the 2.1 count difference occurs when they add.

Wing-fuselage solutions require a larger number of spanwise and lengthwise points for drag results within 1/2 count of the extrapolated zero mesh value. A 91×91×91 grid is sufficient for PNS calculations and, following the pattern seen in the wing-alone grid sizes, a 91×51×91 grid is chosen for the wing-fuselage Euler computations. The computational cost for the Euler and PNS solutions on an SGI Power Challenge R8000 are 35 minutes and 3.3 hours respectively. The algebraic skin friction estimates are still within 1.0 count of those from PNS. Linear theory underpredicts the cruise drag for all three designs by 0.7 to 1.3 counts.

The aircraft range is sensitive to these relatively small differences in the cruise drag. For the Design Case 2 cambered wing, linear theory underestimates the cruise drag coefficient by 2.1 counts. The resulting range is 126 *n.mi.* larger than that predicted from PNS aerodynamics. The aircraft TOGW is also sensitive to drag variations of this magnitude. If we compensate for the linear theory cruise drag underestimate by adding 2.0 counts to it in the optimization procedure, the resulting aircraft is 56,118 *lbs* heavier than the original design. The majority of this added weight comes from the extra fuel required to meet the range requirement.

The PNS and Euler loads match closely at the flight conditions examined. At supersonic cruise, linear theory also compares well with CFD. The same is not true for high-lift conditions where crossflow shocks appear on the wings. In these cases, linear theory predicts the loads well inboard of the shock, underestimates the loads immediately outboard of the shock, and overestimates the loads at the subsonic leading edge. Despite the good agreement in loads at cruise, differences of 21%–49% are seen in the Von Mises stresses. The differences in maximum stress are lower, but still reach 23.6%. The magnitude of the differences in stresses is reflected in the differences in the spanwise center of pressure locations. Using Euler loads in the structural analysis results in a more inboard center of pressure and lower stresses over most of the wing. The Mach 1.2 cruise conditions show the largest regions on the wing where the stresses from Euler loads are bigger than those from linear theory loads. For Design Cases 1 and 2, the wing bending-material weights computed using Euler loads are lower than those from linear theory loads. However in Design Case 3, the larger stresses in the Mach 1.2 load case result in a heavier design using Euler loads. The bending material weights are not as sensitive as the wing stresses to the differences in loads. The difference in bending material weights is not greater than 5.6% for the three designs.

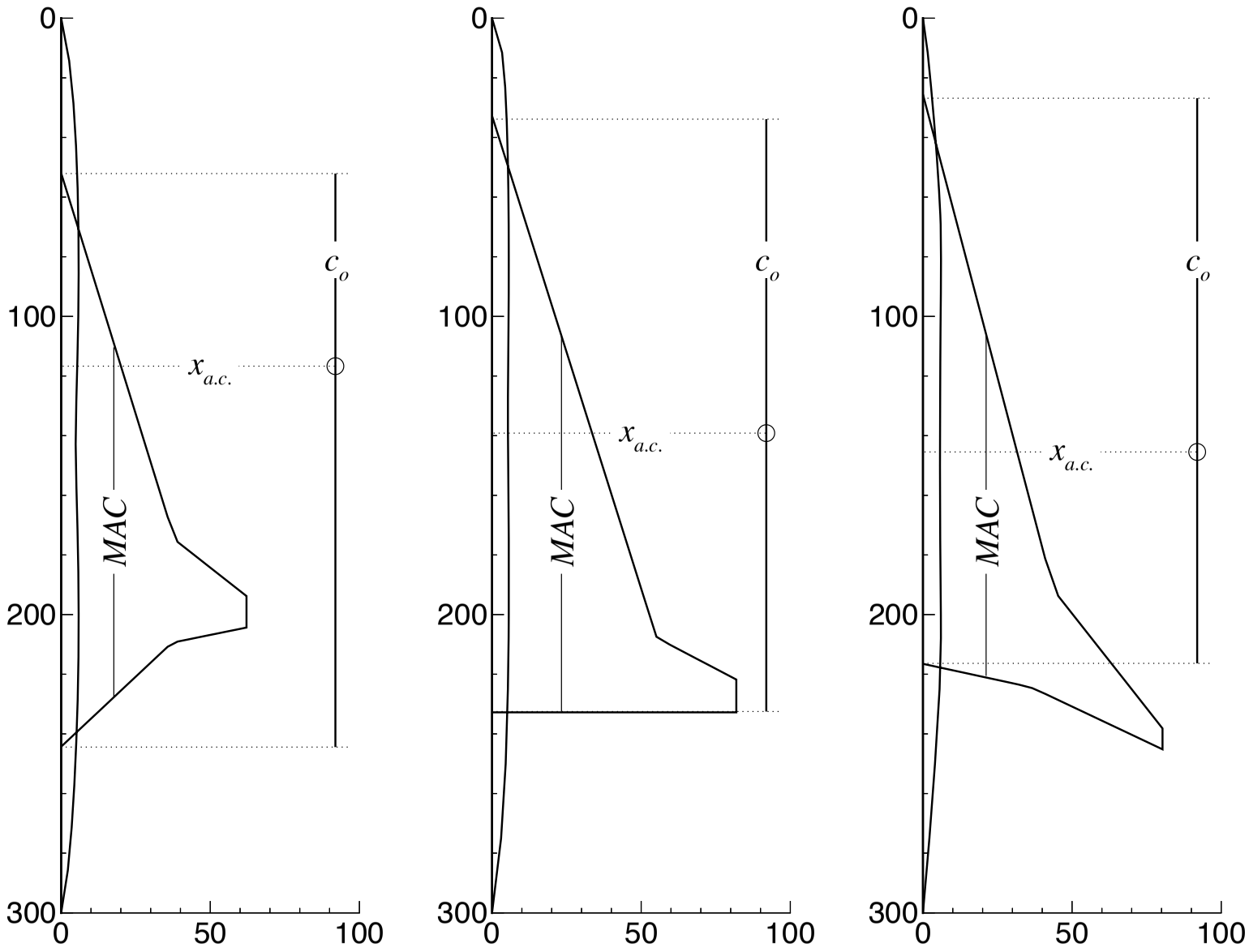

Figure 71: Aerodynamic Center Location Shift with Trailing-Edge Sweep

5. Concluding Remarks

The aerodynamic modeling requirements for multidisciplinary HSCT design optimization have been assessed through comparisons of CFD and linear supersonic theory estimates of the aerodynamic forces and moments and structural loads. Because the HSCT fuselage is slender and the wings are thin for improved supersonic aerodynamics, linear supersonic theory drag predictions at small values of the lift coefficient are fairly good. Differences in the cruise drag coefficient computed from PNS and linear theory of less than a 3% occur for the wing and wing-fuselage configurations presented. However, these small discrepancies in the predicted drag lead to large variations in the aircraft range. Linear supersonic theory tends to underestimate the cruise drag and therefore overestimate the aircraft range. Discrepancies of up to 126 *n.mi.* for an aircraft with a nominal range of 5500 *n.mi* indicate that linear theory predictions are not sufficient for HSCT range calculations. Small drag variations also have a dramatic effect on the optimization results. The large amounts of fuel the HSCT is required to carry to meet the range constraint makes the TOGW very sensitive to changes in the drag.

Using distributed loads from CFD in the HSCT structural optimization gives rise to differences of up to 24% in the maximum wing bending stress compared to those computed using linear theory loads. This is true even at the cruise conditions, where the loads appear to agree well. This sensitivity is a consequence of the large amount of fuel carried in the HSCT wings. The inertial relief from the fuel weight cancels much of the wing bending due to the aerodynamic loading. Therefore, the wing bending stresses become sensitive to small changes in the predicted center of pressure location. The wing bending material weights, however, appear to be less sensitive to the differences in the wing loading. For the three designs studied, the use of Euler loads as constraints in the structural optimization yields only three to six percent changes in the wing bending material weight compared to that found using linear theory loads.

The increase in the accuracy obtained using PNS and Euler calculations comes at a large increase in computational cost. For wing-fuselage configurations, PNS solutions take about 3.25 hours and Euler solutions take 35 minutes to converge on an SGI Power Challenge R8000 machine. In contrast, the linear supersonic theory predictions can be obtained in a matter of seconds. In order to maintain an efficient optimization we must be able to use a small number of CFD solutions to improve the accuracy of our less expensive methods. This becomes especially important when we apply CFD in the subsonic and transonic regimes, where our current computational costs will increase by an order of magnitude. Future work includes performing the aerodynamic and structural comparisons presented in this study for HSCT configurations in transonic flight conditions.

The integration of the CFD solution package into the optimization procedure is a source of difficulty. The simple aerodynamic models are relatively easy to code and integrate into a single VCM optimization program, but the size and complexity of production level grid generators and computational fluid dynamics codes prevent them from being integrated in this manner. The way in which we plan to overcome this problem is through the use of variable-complexity response surface modeling.[39–41] Using response surface approximations for the aerodynamic quantities allows the grid generation and CFD calculations to be performed separately from the optimization procedure by the people who are most proficient in using these codes. It also makes possible the incorporation of data from multiple sources and levels of accuracy. As part of our MAD Center activities, we are currently researching data representation methods which utilize thousands of calculations from linear methods, 10–100 detailed Euler/Navier-Stokes solutions, and perhaps some experimental data to create an accurate approximation to our HSCT response surfaces.

Acknowledgment

This work was supported by the NASA Langley Research Center under grants NAG1–1160 and NAG1–1562.

References

[1] M. G. Hutchison, E. R. Unger, W. H. Mason, B. Grossman, and R. T. Haftka. "Aerodynamic Optimization of an HSCT Configuration Using Variable-Complexity Modeling," AIAA Paper No. 93–0101, January 1993.

[2] M. G. Hutchison, E. R. Unger, W. H. Mason, B. Grossman, and R. T. Haftka. "Variable-Complexity Aerodynamic Optimization of a High-Speed Civil Transport Wing," *Journal of Aircraft*, 31, No. 1: 110–116, 1994.

[3] J. Dudley, X. Huang, R. T. Haftka, B. Grossman, and W. H. Mason. "Variable-Complexity Interlacing of Weight Equation and Structural Optimization of the High-Speed Civil Transport," AIAA Paper No. 94–4377, September 1994.

[4] J. Dudley, X. Huang, P. E. MacMillin, B. Grossman, R. T. Haftka, and W. H. Mason. "Multidisciplinary Optimization of the High-Speed Civil Transport," AIAA Paper No. 95–0124, January 1995.

[5] R. V. Harris, Jr. "An Analysis and Correlation of Aircraft Wave Drag," NASA TM X–947, 1964.

[6] H. W. Carlson and D. S. Miller. "Numerical Methods for the Design and Analysis of Wings at Supersonic Speeds," NASA TN D–7713, 1974.

[7] H. W. Carlson and R. J. Mack. "Estimation of Leading-Edge Thrust for Supersonic Wings of Arbitrary Planforms," NASA TP–1270, 1978.

[8] E. J. Hopkins and M. Inouye. "An Evaluation of Theories Predicting Turbulent Skin Friction and Heat Transfer on Flat Plates at Supersonic and Hypersonic Mach Numbers," *AIAA Journal*, 9, No. 6: 993–1003, June 1971.

[9] D. M. Hollenback and G. A. Blom. "Application of a Parabolized Navier-Stokes Code to an HSCT Configuration and Comparison to Wind Tunnel Test Data," AIAA Paper No. 93–3537, August 1993.

[10] J. L. Pittman, D. L. Bonhaus, M. J. Siclari, and S. M. Dollyhigh. "Euler Analysis of a High-Speed Civil Transport Concept at Mach 3," *Journal of Aircraft*, 28, No. 4: 239–245, April 1991.

[11] M. J. Mann and H. W. Carlson. "An Assessment of Current Methods for Drag-Due-To-Lift Minimization at Supersonic Speeds," AIAA Paper No. 91–3302, September 1991.

[12] P. Covell, G. Hernandez, J. Flamm, and O. Rose. "Supersonic Aerodynamic Characteristics of a Mach 3 High-Speed Civil Transport Configuration," AIAA Paper No. 90–3210, September 1990.

[13] W. D. McGrory, D. C. Slack, M. P. Applebaum, and R. W. Walters. *GASP Version 2.2 Users Manual*, Aerosoft, Inc., 1993.

[14] R. L. Barger, M. S. Adams, and R. R. Krishnan. "Automatic Computation of Euler-Marching and Subsonic Grids for Wing-Fuselage Configurations," NASA TM 4573, July 1994.

[15] C. B. Craidon. "Description of a Digital Computer Program for Airplane Configuration Plots," NASA TM X–2074, 1970.

[16] R. L. Barger and M. S. Adams. "Automatic Computation of Wing-Fuselage Intersection Lines and Fillet Inserts with Fixed-Area Constraint," NASA TM 4406, March 1993.

[17] Vanderplaats, Miura and Associates, Inc., 5960 Mandarin Avenue, Suite F, Goleta, CA 93117. *GENESIS User Manual, Version 1.3.*

[18] S. Burgee, A. A. Giunta, R. Narducci, L. T. Watson, B. Grossman, and R. T. Haftka. "A Coarse Grained Variable-Complexity Approach to MDO for HSCT Design," in D. H. Bailey, P. E. Bjørstad, J. R. Gilbert, M. V. Mascagni, R. S. Schreiber, H. D. Simon, V. J. Torczon, and L. T. Watson, eds., *Parallel Processing for Scientific Computing*, pp. 96–101, Philidelphia, PA, SIAM, 1995.

[19] X. Huang, R. T. Haftka, B. Grossman, and W. H. Mason. "Comparison of Statistical Weight Equations with Structural Optimization for Supersonic Transport Wings," AIAA Paper No. 94–4379, September 1994.

[20] P. J. Bobbitt. "The Pros and Cons of Code Validation," AIAA Paper No. 88–2535, June 1988.

[21] P. W. Sacher, R. G. Bradley, Jr., and W. Schmidt. "Technical Evaluation Report on the Fluid Dynamics Symposium on Validation of CFD [CP-437]," AGARD AR-257, May 1989.

[22] D. P. Aeschliman, W. L. Oberkampf, and F. G. Blottner. "A Proposed Methodology for Computational Fluid Dynamics Code Verification, Calibration, and Validation," 16^{th} *International Congress on Instrumentation in Aerospace Simulation Facilities (ICIASF)*, Wright-Patterson AFB, OH, July 18–21 1995.

[23] R. E. Melnik, M. J. Siclari, T. Barber, and A. Verhoff. "A Process for Industry Certification of Physical Simulation Codes," AIAA Paper No. 94–2235, June 1994.

[24] R. E. Melnik, M. J. Siclari, F. Marconi, T. Barber, and A. Verhoff. "An Overview of a Recent Industry Effort at CFD Code Certification," AIAA Paper No. 95–2229, June 1995.

[25] F. Marconi, M. Siclari, G. Carpenter, and R. Chow. "Comparison of TLNS3D Computations with Test Data for a Transport Wing/Simple Body Configuration," AIAA Paper No. 94–2237, June 1994.

[26] R. V. Harris, Jr. and E. J. Landrum. "Drag Characteristics of a series of a Series of Low-Drag Bodies of Revolution at Mach Numbers From 0.6 to 4.0," NASA TN-D 3163, December 1965.

[27] W. H. Mason and J. Lee. "Aerodynamically Blunt and Sharp Bodies," *Journal of Spacecraft and Rockets*, 31, No. 3: 406–413, May-June 1994.

[28] P. J. Roache. "Perspective: A Method for Uniform Reporting of Grid Refinement Studies," *Journal of Fluids Engineering*, 116: 405–413, September 1994.

[29] J. Weber and C. King. "Analysis of the Zero-Lift Wave Drag Measured on Delta Wings," *Aeronautical Research Counsel Reports and Memoranda No. 3818*, 1978.

[30] M. J. Siclari. "The NCOREL Computer Program for 3D Nonlinear Supersonic Potential Flow Computations," NASA CR–3694, 1983.

[31] W. H. Mason, M. J. Siclari, D. S. Miller, and J. L. Pittman. "A Supersonic Maneuver Wing Designed for Nonlinear Attached Flow," AIAA Paper No. 83–0425, January 1983.

[32] M. Siclari, M. Visich, A. Cenko, B. Rosen, and W. Mason. "An Evaluation of NCOREL, PAN AIR, and W12SC3 for Supersonic Wing Pressures," *Journal of Aircraft*, 21, No. 10: 816–822, October 1984.

[33] J. L. Pittman, D. S. Miller, and W. H. Mason. "Supersonic, Nonlinear, Attached-Flow Wing Design for High Lift With Experimental Validation," NASA TP–2336, August 1984.

[34] S. C. Somer and B. J. Short. "Free-Flight Measurements of Turbulent-Boundary-Layer Skin Friction in the Presence of Severe Aerodynamic Heating at Mach Numbers from 2.8 to 7.0," NASA TN 3391, 1955.

[35] E. Eminton. "On the Minimization and Numerical Evaluation of Wave Drag," *Royal Aircraft Establishment Report AERO.2564*, November 1955.

[36] R. T. Jones and D. Cohen. *High Speed Wing Theory*, Princeton University Press, 1960.

[37] H. W. Carlson and K. B. Walkley. "Numerical Methods and a Computer Program for Subsonic and Supersonic Aerodynamic Design and Analysis of Wings with Attainable Thrust Corrections," NASA CR–3808, 1984.

[38] P. E. MacMillin., O. Golividov, W. H. Mason, B. Grossman, and R. T. Haftka. "Trim, Control, and Performance Effects in Variable-Complexity High-Speed Civil Transport Design," *MAD Center Report 96–07–01*, Virginia Tech, Blacksburg, VA, July 1996.

[39] A. A. Giunta, R. Narducci, S. Burgee, B. Grossman, W. H. Mason, L. T. Watson, and R. T. Haftka. "Variable-Complexity Response Surface Aerodynamic Design of an HSCT Wing," AIAA Paper No. 95–1886, June 1995.

[40] M. Kaufman, V. Balabanov, S. L. Burgee, A. A. Giunta, B. Grossman, W. H. Mason, L. T. Watson, and R. T. Haftka. "Variable-Complexity Response Surface Approximations for Wing Structural Weight in HSCT Design," AIAA Paper No. 96–0089, January 1996.

[41] A. A. Giunta, O. Golividov, D. L. Knill, B. Grossman, W. H. Mason, L. T. Watson, and R. T. Haftka. "Multidisciplinary Design Optimization of Advanced Configurations," 15^{th} *International Conference on Numerical Methods in Fluid Dynamics*, Monterey, CA, June 1996.